Electrical characteristics of thin-film transistors (TFTs) based on the solution-processed Zinc Tin Oxide (ZTO) channel layer

by

Sunil Uprety

A dissertation submitted to the Graduate Faculty of
Auburn University
in partial fulfillment of the
requirements for the Degree of
Doctor of Philosophy

Auburn, Alabama
December 11, 2021

Keywords: Solution Process, Amorphous Oxide Semiconductors, Zinc Tin Oxide, Molar Concentration, Microwave-assisted annealing, Gamma and Proton Irradiation

Approved by

Minseo Park, Chair, Professor, Department of Physics
Michael Bozack, Emeritus Professor, Department of Physics
Sarit Dhar, Professor, Department of Physics
Ayayi C. Ahyi, Associate Research Professor, Department of Physics
Stuart Loch, Professor, Department of Physics
Dong-Joo Kim, Alumni Professor, Department of Materials Engineering

Abstract

Transparent amorphous metal oxide-based semiconductors have received significant attention since their inception by Hosono *et al*. Zinc tin oxide (ZTO), among others, has emerged as a promising candidate for indium-free semiconductors, enabling competitive device performance in comparison with its indium-based counterparts. High manufacturing costs pose an obstacle to the realization of modern large-area and mass-produced electronics. In contrast, the solution-processed deposition of semiconductor layers offers many advantages: simplicity, low-cost, and high throughput, still exhibiting performances more outstanding than conventional silicon in terms of their crucial performance parameters, such as charge-carrier mobility and current on−off ratio.

Solution-processed Zinc Tin Oxide (ZTO) thin-film transistors were fabricated. Thin Film transistors TFTs)fabricated with alternating concentrations were found to have enhanced electrical characteristics. It was attributed to the decreased surface roughness, increased oxygen vacancies (acting as donors), and decreased M-OH (acting as traps) ratios as obtained from X-ray Photoelectron Spectroscopy (XPS) analysis. It was also conjectured that low concentration (0.05M) film at the bottom of the alternating concentration film was used as a nucleation layer and helped reduce interface traps.

Secondly, ZTO films were subjected to Microwave (MW) assisted annealing for the microwave's different powers. Surface and electrical characterizations were performed. MW-assisted annealing showed reduced hydroxyl groups enhancing dihydroxylation and condensation of ZTO films and more oxygen vacancies produced via hydroxyl groups' decomposition during annealing the electrical characteristics of MW-assisted annealed films.

Effects of gamma irradiation on ZTO thin films and TFTs were studied for the different dosages of gamma irradiation. Shifts in the threshold voltage (V_{th}), changes in the field-effect mobilities (μ_{FE}), transconductance (g_m), saturation drain current (I_D), donor concentration (N_d) were studied for samples irradiated for four weeks with a dose rate of 23.59 rad/sec with a total dose of about 57 MRad. The electrical parameters' changes were attributed to the combined effect of radiation-induced positive oxide traps and negative interface trap charges.

Acknowledgments

I first and foremost would like to express my extreme gratitude to my supervisor, Dr. Minseo Park for his invaluable advice, continuous support, and patience during my Ph.D. study. I also would like to thank Dr. Bozack, Dr. Dhar. Dr. Ahyi, Dr. Kim, Dr. Loch for agreeing to serve as the committee members and evaluation my work. All your immense knowledge and plentiful experience have encouraged me in all the time of my academic research and daily life. I would also like to thank Tami and Max for their technical support on my research. I am indebted to Dr. Bozack, Dr. Comes, Dr. Dhar, Dr. Oh. Dr. Ahyi for their expertise and letting me use lab equipment used in my research.

My gratitude extends to the Department of Physics, Auburn University for understanding my situation and for the opportunity to undertake my research, and completion of my program. I would like to thank all the members in experimental solid state research group namely Dr. Burcu Ozden, Dr. Min Khanal, Dr. Vahid Mirkhani, Dr. Kosala Yapa Bandara, Dr. Shiqiang Wang, Dr. Asanka Jayawardena, Dr. Isanka Jayawardhena, Suman, Suresh, and Rajendra. It is your kind help and support that have made my study and life in the US a wonderful time.

Beyond everything, I would like to express my deepest gratitude to my parents, Dharma Bhakta and Narayani Uprety, for their unparalleled sacrifices to get me here from an underdeveloped village of Nepal to where I am today. I hope I made you proud! Thank you, my brothers Sushil, Suman, and sisters is laws Laxmi, and Tarjuma for being there as a continuous source of inspiration. It would be an injustice if I don't spend few words of acknowledgement toward my aunt (Sanima) and her family, uncles (Mama) and their family, Grandmother (my mother's side). Thank you for your support throughout my stay in Pokhara. No words of

acknowledgement would suffice to express my gratitude for the help, support and encouragement of my beloved wife Puja, during my study and our testing times. You inspire me every day. Thank you for being there.

Yanika, our sweet baby girl, your daddy misses you a lot. Thank you for teaching me the real meaning of love. I can't thank you enough for bestowing us with your presence in our lives. You have given me a reason to be a better person.

Last but not the least, I want to thank everyone who's been part of my life along the way in any shape or form. Without all your tremendous understanding and encouragement in the past few years, it would be impossible for me to complete my study.

Dedicated to our daughters,
Sulaxya, Mokshya and Yanika

Table of Contents

List of Tables

List of Figures

List of Abbreviations

WBG	Wide Band Gap
GaN	Gallium Nitride
SiC	Silicon Carbide
ZnO	Zinc Oxide
ZTO	Zinc Tin Oxide
IGZO	Indium Gallium Zinc Oxide
IZO	Indium Zinc Oxide
AOS	Amorphous Oxide Semiconductors
MOSFET	Metal Oxide Semiconductor Field Effect Transistor
FET	Field Effect Transistor
BJT	Bipolar Junction Transistor
JFET	Junction Field Effect Transistor
CMOS	Complementary Metal Oxide Semiconductor
AMOLED	Active-Matrix Organic Light Emitting Diode
FPD	Flat Panel Display
LCD	Liquid Crystal Display
AMLCD	Active-Matrix Liquid Crystal Display

TFTs	Thin Film Transistors
C-V	Capacitance-Voltage
DC	Direct Current
Ga-ZnO	Gallium doped Zinc Oxide
I-V	Current-Voltage
PL	Photoluminescence
rf	Radio Frequency
em	Electromagnetic
SiO_2	Silicon dioxide
$MoSi_2$	Molybdenum Silicide
XRD	X-Ray Diffraction
XPS	X-Ray Photoelectron Spectroscopy
AFM	Atomic Force Microscopy
EDS	Electron Dispersive Spectroscopy
SEM	Scanning Electron Microscopy
NBS	Negative Bias Stress
PBS	Positive Bias Stress
NBIS	Negative Bias Illumination Stress

RT	Room Temperature
UV	Ultraviolet
TMAH	Tetramethyl ammonium hydroxide
DC	Direct Current
PVD	Physical Vapor Deposition
Ar	Argon
RTA	Rapid thermal Annealing
TLM	Transmission Line Model
MW	Microwave
HP	Hot Plate
ESR	Electron Spin Resonance
EELS	Electron Energy Loss Spectroscopy
GCR	Galactic Cosmic Rays
SPE	Solar Particle Events
CME	Coronal Mass Ejections
TID	Total Ionizing Dose
SEU	Single Event Upsets
SEGR	Single Event Gate Rupture

SEL	Single Event Latch ups
NIEL	Non-Ionizing Energy Loss
ASTM	American Society of Testing Materials
He-CD	Helium Cadmium
UHV	Ultra High Vacuum

Chapter 1

Introduction and Literature review

1.1 Introduction

The advent of Silicon Integrated Circuits (ICs) nearly half a century ago has inexorably paved the path for modern computing and electronics. However, the recent developments and advances have pushed Si semiconductor technology to a limit since the power devices for many applications do not work appropriately with Si-based material or do not meet the requirements. The requirements to be mentioned are higher blocking voltages, switching frequencies, efficiencies, and reliability. Wide bandgap (WBG) semiconductors such as GaN, SiC, ZnO are preferred to subdue the limitations as mentioned earlier. These WBG semiconductors are highly likely to replace Si soon. WBG semiconductor materials have superior electrical characteristics shown in the table below [1]–[3].

Table 1.1: Physical Characteristics of Si and other WBG

Property	Si	GaAs	GaN	ZnO	6H-SiC	4H-SiC	Diamond
Band Gap, Eg (eV)	1.12	1.43	3.45	3.6	3.03	3.26	5.45
Dielectric constant, ε_r[a]	11.9	13.1	9	9	9.66	10.1	5.5
Electric breakdown Field, Ec (kV/cm)	300	400	2000	200	2500	2200	10000
Hole mobility μ_p (cm^2/V.sec)	600	400	850	180	101	115	850
Electron mobility μ_n (cm^2/V.sec)	1500	8500	1250	200	500	100	2200
Thermal Conductivity, λ	1.5	0.46	1.3	1.3	4.9	4.9	22

[a] $\varepsilon = \varepsilon_r.\varepsilon_o = 8.85 \times 10^{-14}$ F/cm

Some of the advantages of WBG semiconductors over Si can be summarized as follows:

- WBG semiconductor-based power devices have higher breakdown voltages because of their high electrical breakdown field.
- WBG semiconductor-based unipolar devices are thinner and have lower on-resistances.
- WBG semiconductor-based power devices can operate at high temperatures.
- WBG devices have a higher thermal conductivity (4.9 W/cm.K for SiC and 22 W/cm.K for a diamond) instead of 1.5 W/cm.K for Si).
- Forward and reverse characteristics of WBG semiconductor-based power devices vary only slightly with temperature and time, and thus they are more reliable.
- Because of low switching losses, WBG semiconductor-based devices can operate at higher frequencies (>20 kHz) are not possible with Si-based devices.

Even before it was widely known as a semiconductor or even a unique element, Zinc Oxide was widely used by Romans in the early first century A.D. It was not until the 14^{th} century that the Indians recognized zinc in Zewar, India. ZnO was produced by the smelting process [4] as a byproduct, and the powder was used as a remedy for sore eyes. Before the electrical and optical properties of it were realized, ZnO's white powder was used in painting. ZnO's first use for the electronic application was made in the 1920s in radio sets [5] as a Schottky barrier. ZnO is also reported to be used as a bacteriostatic in human medicine [6]. It has also been mentioned to be used in stopping diarrhea in weaned pigs.

1.2 General ZnO Properties:

Zinc Oxide (ZnO) is an II-VI group compound semiconductor with a wide bandgap of around 3.37eV. It has applications in different sectors such as in optical waveguides [7], transparent conductive oxides [8], UV-light emitters [9], piezoelectric transducers [10], spin functional devices [11], solar cells [12], surface acoustic wave devices [13], varistors [14]. The transparency of the material's visible light and softness makes ZnO an appropriate candidate for transparent electronics and flexible electronics. It belongs to the $C_{6\vartheta}^{4}$ ($P6_3$ mc) space group [4]–[6][15]. It has a very high exciton binding energy of about 60meV, much higher than other WBG semiconductors such as Gallium Nitride (GaN) (25meV). ZnO's growth on native substrates yields a reduced concentration of extended defects compared to GaN, which is one of the main reasons for enhanced electrical and optical device performances [16]. ZnO also has been researched as a substitute as a photocatalyst for water decontamination because of its lower cost, relative energy bandgap, and higher visible light photoactivity [17]. Ferromagnetic quantum dots could also be used in high-density storage devices [18]. ZnO is also supposed to be a radiation hard semiconductor, making it a stronger contender for space electronics[19].

Moreover, in RF application, ZnO with a wider bandgap also tends to ease impedance matching related to higher voltage operation [20]. ZnO's large exciton binding energy paves the way for intense near band edge emission at the room, and high temperatures since this value are approximately four times higher than that of the room temperature thermal energy. ZnO is one of the multipurpose functional materials with a vast range of growth morphologies. For example, nanocombs, nanohelixes/nanosprings, nanorings, nanobelts, and nanocages, to name a few. Because of its wide bandgap and properties like high energy radiation stability and its excellent responsivity to wet chemical etching, ZnO makes it preferable among other WBG materials.

However, ZnO's use as a replacement to GaN has been bounded with difficulty in obtaining stable p-type conductivity in ZnO[21]. Several reports have been put forward to claim p-type doping in Zinc Oxide (ZnO) with appropriate hole mobility and concentrations [22].

1.2.1 Crystal and surface Structure of ZnO:

ZnO crystals can take different structures such as wurtzite structure (hexagonal symmetry), zinc blende (cubic symmetry), and rock salt (cubic symmetry). However, unless high-pressure is applied to ZnO crystals, they prefer to stabilize in the wurtzite structure and are thus the most common. Wurtzite ZnO has a hexagonal structure with lattice parameters a= 0.3296 and c= 0.526065. Also, the ratio c/a ratio is around 1.602, which complies with the 1.633 ratios of the hexagonal closed packed structure [23], [24].

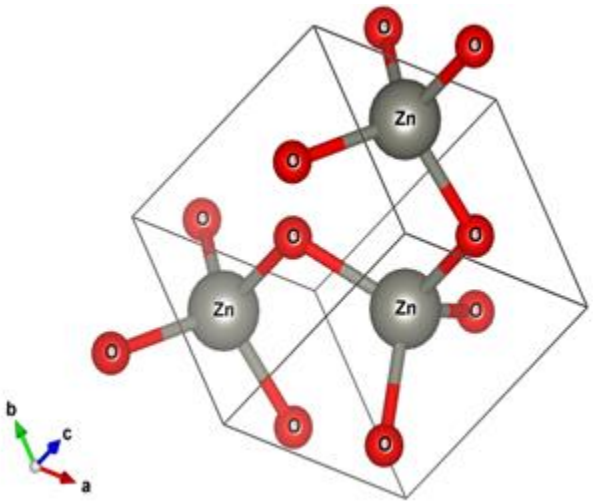

Figure 1.1:Hexagonal Ball and socket structure of ZnO

Zinc blend structure can be obtained by growing on a cubic substrate [25]. It has also been suggested that another phase cubic of cesium chloride could even exist but only in very high temperatures. However, this phase was not yet experimentally observed [26]. Bonding in ZnO crystal lattice involves sp^3 hybridization of the electron states, which lead to four equivalent

orbitals directed in a tetrahedral geometry. In ZnO semiconducting crystal, the sp^3 bonding states constitute the valence bands while the conduction band originates from its antibonding counterpart. The structure of ZnO can be described as a plethora of alternating planes composed of tetrahedrally coordinated O^{2-} and Zn^{2+} ions, stacked alternately along the c-axis. Properties such as piezoelectricity and pyroelectricity in ZnO arise due to this tetrahedral coordination since it creates a non-central symmetric structure.

1.3 Amorphous Oxide Semiconductors (AOSs):

The history of AOSs started in 1954 when a glass group of Sheffield University in the UK reported electronically conductive glasses containing a large amount of V_2O_5 in Nature [27]. Electronic conductivity in these types of oxides was caused by the hopping of electrons from donor to donor. The mobility of electrons in these types of oxide semiconductors was reported to be of the order of 10^{-4} $cm^2/V.s$ at RT. Low mobility and intense coloring due to d-d absorption of transition metal ions made it an unfavorable transparent semiconducting oxide. The main advantage of amorphous materials over crystalline counterparts is the capability of large-area deposition of uniform thin films at low temperatures.

Research on these AOSs started back in the 1950s to find materials that have these types of advantages. Oxide semiconductors such as ZnO, Indium Oxide (In_2O_3), Tin Oxide (SnO_2, SnO), Aluminum Indium Oxide (AIO), Zinc Tin Oxide (ZTO), Indium Gallium Zinc Oxide (IGZO) are a class of materials for transparent electronics applications, mainly flat panels display application since they exhibit good transparency in the visible spectrum due to its wider bandgap of these materials. Research on ZnO [28] demonstrated that a polycrystalline semiconductor film with grain boundaries defects could wane stability, performance, and uniformity of thin-film transistors (TFTs). ZnO also rarely forms a stable amorphous phase at room temperature and generally

exhibits a polycrystalline phase. Hence, the electron mobility cannot be enhanced because of the diffusion at the interfaces of polycrystalline grains. ZnO, moreover, tends to contain oxygen defects and a huge number of carrier electrons, and thus, it is arduous to decrease the electrical conductivity and hence increase the on/off ratio of the transistors [29]. Therefore, the amorphous oxide semiconductors were preferred. AOSs are most likely to have enhanced field-effect mobility compared to hydrogenated amorphous silicon (a-Si:H) and organic semiconductors. Amorphous Si still holds its position for being the dominant semiconductor for AMLCD applications since it is a proven technology, and massive investment still belongs to it. Amorphous hydrogenated silicon (a-Si:H) because of its adversities such as low mobility, poor threshold voltage stability, and relatively high processing temperature, a different breed of semiconductors was needed. AOS came into existence, which exhibited better field-effect mobility and air stability. The amorphous oxide semiconductors tend to have higher mobility because structural randomness concentrates on an energetically fragile part in an amorphous state.

The structural randomness in AOSs widely occur in the bond angle distribution and is more prominent. For covalent semiconductors, the extent of the overlap between the vacant orbitals of the neighboring atoms is extremely sensitive to the bond angle distortion, which results in the creation of deep localized states at reasonably high concentrations, and the drift mobility is highly reduced [30]. However, in an amorphous state in ionic semiconductors, the magnitude of the overlap depends mainly on the choice of metal cations. In these materials, the spatial spread of the s-orbitals, which are isotropic in shape, exceeds the inter cation distance. This is the reason why the magnitude of the bond angle distribution is of low consequence. As a result, we can expect these to have large mobility as compared to their crystalline form. Hence, these ionic semiconductors with heavy post transition metal cations make an excellent choice for amorphous

materials, which could mainly be used for TFT application. Figure 1.2(a) represents the electron transfer mechanism for silicon. In single-crystal structure silicon, transfer path along with hopping mechanism due to long-range order in the crystal structure using sp3 hybridization orbitals, possess large electron field mobility. Silicon, a covalent semiconductor, the conduction band minimum, and valence band maximum are formed by anti-bonding and bonding states of Si sp3 hybridized orbitals [31].

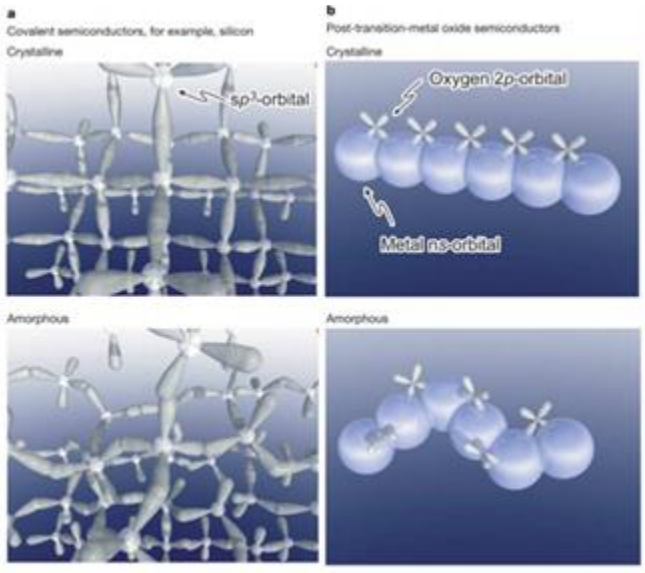

Figure 1.2: Schematic orbital drawings for the carrier transport paths (i.e., conduction bottom bottoms) in crystalline and amorphous semiconductors. (a) Covalent semiconductors with sp3 orbitals, (b) metal oxide semiconductors with an s-orbital overlap

But when the amorphous silicon structure is considered, they lack long-range order, and thus the electron carriers cannot move swiftly because of the barrier with random structure. In a metal oxide semiconductor, a large s-orbital of metal ion possesses an overlapping between adjacent atoms and provides a current electron carrier path. Despite their amorphous nature in the metal oxide layer, the s-orbital is easy to overlap with another s orbital, as shown in figure 1.2.

The first demonstration of flexible amorphous IGZO TFTs was performed by Nomura *et al.* in 2004 [33]. Since its inception, tremendous efforts have been made to AOS TFT device research, mainly in next-generation flat panel display applications. Ito *et al.* [34] demonstrated the use of amorphous oxide TFTs to electrophoretic display in 2008. They fabricated a 4-inch bottom gated amorphous Indium Gallium Zinc Oxide (a-IGZO) TFT arrays and combined it with an electrophoretic front-plane. Jeong *et al.* (2009) demonstrated a full-color 12.1-in. WXGA active-matrix organic-light-emitting-diode (AMOLED) display for the first time using IGZO TFTs as an active matrix backplane [35]. With the proper implementation of IGZO TFT arrays, Samsung Electronics victoriously developed a 70 inch 240 HZ 3D Ultra Definition (UD) Television (TV) prototype, which they presented at a conference, Flat Panel Display (FPD) International 2010, November [36].

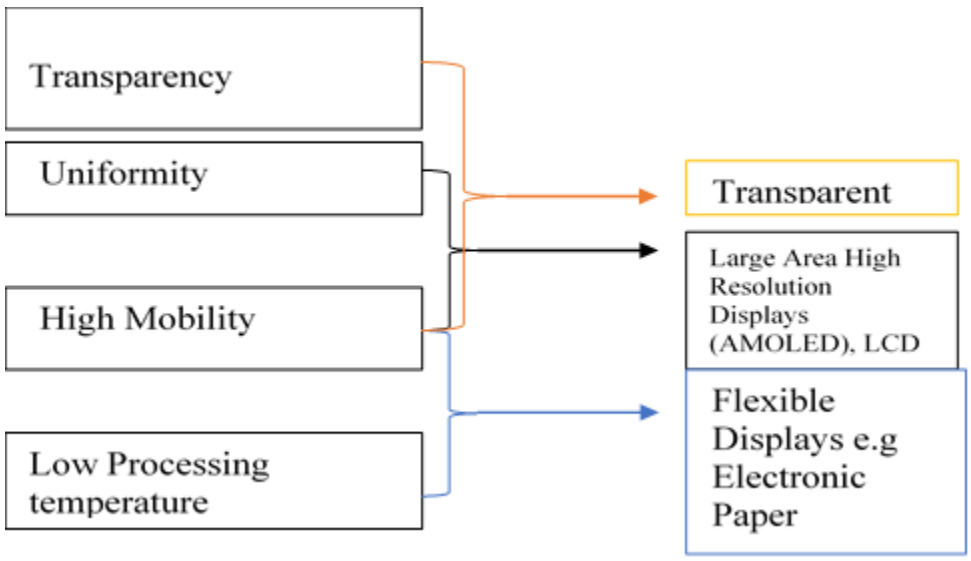

Figure 1.3: Wager *et al.*, "Transparent electronics" (2008) [43]

Amorphous Oxide Semiconductors TFTs, in conjunction with AMLCDs, could also be used as alternatives to low-temperature polysilicon (LTPS) TFTs used as driving elements in AMOLED displays. LTPs with the non-uniform spatial distribution of poly-Si grain structure

results in various device properties over large areas. Therefore, current AMOLED displays are bound to relatively small size applications, e.g., cell phone applications. With the advancement of technology, the application of oxide-based TFTs is not restricted to displays. They have been employed in ICs, amplifiers, logic gates, ring oscillators, radio frequency identification systems, and so on [37]–[42]. Figure 1.3 summarizes the potential applications and merits of using AOS TFTs.

Table 1.2: The characteristics that differentiate the two classes of AOS.

	Conventional AOS (e.g. a:Si-H)	Amorphous oxide Semiconductors
Chemical bonding	Covalent	Ionic
Conduction Mechanism	Hopping	Band Conduction
Mobility	1-2 $cm^2/V.\ s$	10-55 $cm^2/V.\ s$
Degenerate doping	Not Possible	Possible

Some of the most common oxide semiconductors are described below:

1.3.1 Indium Gallium Zinc Oxide (IGZO)

IGZO is a fascinating material that can be used in various technologies. Applications could include transparent electronics, high-end displays, flexible electronics, memories, and it is also a potential candidate for three-dimensional integrated circuits. It is a wide bandgap (~3.5eV), an n-type semiconductor. Stoichiometrically, it is generally written as $In_{2x}Ga_{2-2x}(ZnO)_k$ where $0<x<1$ and k is an integer greater than 0 [44]–[48], which suggests that it is a ternary metal oxide material that comprises of In_2O_3, Ga_2O_3, and ZnO. The inception of IGZO technology was made by incorporating gallium into IZO by Nomura *et al.* in 2004 [49].

As mentioned earlier, such a composition generally impedes the compound material's crystallization at high temperatures. The density of states (DOS) of amorphous IGZO near the conduction band is lower than that of amorphous hydrogenated silicon (a-Si:H) [50]. The incorporation of gallium into IZO plays the role of a suppressing agent to minimize the formation of oxygen vacancies. These oxygen vacancies are present throughout the material, which act as intrinsic donors, and their effective concentration controls the conductivity of the material [31], [51], [52]. These vacancies are formed because of the imperfections in the amorphous structure of IGZO. Gallium creates a strong bond with oxygen because of its large oxygen vacancy formation energy [51]. Also, Gallium oxide (Ga_2O_3) has the highest average electron affinity (-3.1 eV) compared to indium oxide, zinc oxide, or tin oxide between -4.4 and -4.6 eV is the reason it possesses the strongest metal-oxygen bonds in the IGZO mixture. However, the incorporation of Gallium into IGZO has to be in a controlled manner as its carrier suppressing ability would also act as a reason for increasing TFT threshold voltage [53]. Jeong *et al.* studied the role of Gallium doping in solution-processed IZO in dramatically lowering amorphous oxide processing temperatures [54]. The effect of annealing temperature on mobility and AOS composition were analyzed, and the chemical role of Ga addition was clarified.

G. H. Kim *et al.* investigated the role of Ga concentration in the InZnO compound system [55]. The incorporation of Ga into the InZnO system resulted in a decrease in the carrier concentration of the films off current of thin-film transistors (TFTs). It was attributed to the Ga ions forming a stronger chemical bond with oxygen as compared to the Zn and In ions, behaving as a carrier suppressor. G. H. Kim also studied the effect of Indium (In) content on characteristics of nanocrystalline IGZO films grown by a solution process method along with the TFTs fabricated with it [56]. Indium corporation into IGZO helped to enhance the field-effect mobilities of the

TFTs because of the increase in conducting pathways and the decrease in grain size. Also, the surface roughness of the film was found to be reduced due to more InO_2^- ions induce cubic stacking faults with IGZO. Jianke Yao *et al.* studied electrical and Photosensitive characteristics of a-IGZO TFTs related to Oxygen vacancy [57]. Degradation of TFTs was observed for the TFTs with lower oxygen vacancies ($\ddot{Vo}$)in the IGZO film. Electron density of the channel was decreased along with the saturation mobility. Threshold voltage and subthreshold slope (SS) was found to be increased with a lower ON current and higher interface defect density. The photosensitive behavior of a-IGZO TFTs was found to be dependent on the absorption of a-IGZO, i.e., for higher absorption, the thin film transistors had large photocurrent and a larger shift in the threshold voltage after the illumination of light.

H. K. Noh *et al.* studied the structure of oxygen vacancies Vo defect in a-IGZO performing first-principle density functional calculations to investigate the atomic and electronic properties of different kinds of O-vacancy (Vo) defects. They discovered that the formation energies of Vo tended to increase with an increased number of near Ga atoms. In addition to it, the formation of energies was much reduced in the ambiance of In atoms which made it easy for the generation of O- deficient defects [58]. Ide *et al.* discussed the effects of excess oxygen on operation characteristics of a-IGZO TFTs. TFTs annealed in O_3 ambient at~150°C improved the subthreshold swing, mobility, and threshold voltage. However, when annealed at the same ambient at around 300ºC, caused significant deterioration, exhibiting a bistable transition between a large V_{th} state and S state [59].

1.3.2 Zinc Tin Oxide (ZTO):

The ternary oxide ZTO presents its candidacy as an eligible TCO because of good transparency (95% in visible portion), low resistivity, tunable work function, and chemical

selectivity, among all other things [60]– [62]. ZTO could be used mainly as a channel layer for display devices and solar cells, like using other transparent semiconducting oxides. An amorphous phase of ZTO is usually beneficial to avoid grain boundary effects. Several crystalline phases have been reported to form depending upon the methods and conditions while synthesizing ZTO. There are mainly two crystalline phases for ZTO; Zn_2SnO_4 and Zn_2SnO_3 represent the compositions.

Chiang *et al.* [63] reported the novel TFTs based on amorphous zinc tin oxide (ZTO) channel material. The semiconducting material was deposited from a ceramic target using radio frequency (rf) magnetron sputtering in an argon and oxygen atmosphere. The substrate was coated with a 200nm sputtered indium tin oxide (ITO) layer underneath a 220nm atomic layer deposited superlattice of AlO_x and TiO_x (ATO). The ZTO channel layer was formed with two different stoichiometries, $(ZnO)_x(SnO_2)_{1-x}$ (x=1/2 and x=2/3), which corresponds to the compositions of the ilmenite ($ZnSnO_3$) and spinel (Zn_2SnO_4) structures, respectively. Device performance, precisely in terms of channel mobility, exhibited minimal variation between these two stoichiometries, which indicated the possibility of an extraordinary insensitivity to stoichiometry (ratio of Zn:Sn). The trend of increasing mobility with increasing annealing temperature was attributed to the modification of the semiconductor-insulator interface with annealing or improved atomic rearrangement because of higher temperature rather than enhancing long-range crystallinity.

Hong *et al*. [64] reported ZTO thin-film transistors' fabrication *via* reactive magnetron sputtering using a metallic zinc/tin alloy target. The oxygen partial pressure and total sputtering pressure were clearly examined. Sputtering was performed in an oxygen/argon environment with a total pressure of 30mTorr, while oxygen partial pressure was varied from 0.5 to 1.2mTorr. The devices were completed with aluminum top contacts with shadow masks. Transistors fabricated had incremental mobilities of $11cm^2/V.s$ and average mobility of $32cm^2/V.s$ for two different

annealing temperatures of 300 and 500°C. With this study, an optimal value of oxygen partial pressure is at 0.8mTorr, which corresponds to the incremental mobility peak for both annealing conditions.

Lee *et al*. in 2010 demonstrated ZTO showed a band transport in the saturation regime, which is due to the localized states and is more pronounced at a higher value of the charge carrier concentration [65]. Inkjet-printed Zinc Tin Oxide TFTs were first reported by Kim *et al*. in 2009 [66]. They used a similar process and the same precursors and transistor layout as reported by Jeong *et al.* [67], but this time instead of the spin coating process, they used the inkjet printing process. The maximum saturation mobility reported to be 0.6 cm^2/V.s. Braquinho *et al*. reported on a new environmentally friendly route of solution combustion synthesis, using ethanol as a solvent to prepare indium/gallium free ZTO TFTs using AlO_x as a dielectric layer. The decomposition of ZTO and AlO_x precursor solutions, electrical characterizations, and stability of solution processed ZTO/AlO_x TFTs under positive bias stress, in air and vacuum, were investigated. It was concluded that ethanol-based ZTO/AlO_x could demonstrate low operation voltages, low subthreshold (S), and saturation mobility of about 0.8 cm^2/V.s [68].

Hong and Wager [69] explored the methodology for the passivation of bottom gated ZTO TFTs with SiO_2 as a passivation layer. Staggered inverted TFTs were passivated using thermally evaporating SiO_2 over the exposed channel, deposited by rf magnetron sputtering from a ceramic target. ZTO thickness of 80nm was deposited onto a silicon substrate with a layer of thermally grown SiO_2. ITO was used as a source and drain contacts. The non-passivated TFTs were then annealed at 600°C. It was found that passivated ZTO TFTs possessed electrical characteristics equivalent to those of non-passivated, air-exposed devices. In contrast, TFT electrical performance was found to be affectedly degraded if ZTO TFTs were covered with a dielectric layer and does

not subject to both types of annealing. In addition to silicon dioxide, successful passivation of ZTO TFTs was performed using thermally evaporated calcium fluoride, strontium fluoride, germanium oxide, or antimony oxide as passivating dielectrics.

Yuan *et al*. studied the effect of annealing temperature on the growth of Zn-Sn-O nanocomposites thin films. XRD analysis performed on the films showed that the composition largely depended upon the annealing temperature. Spinel zinc stannate (Zn_2SnO_4) was obtained at around 400-700°C. The perovskite-type zinc stannate $ZnSnO_3$ appeared at 800°C, and the Zn_2SiO_4 was produced only above 1000°C. Also, the lattice parameter, grain size, and micro strain were investigated to understand the influence of annealing temperature on the film property. The average transmittance of the ZTO films was found around 80% - 96%, and the film's optical band gap increased from 3.55 to 4.09 eV with temperature increases from 300 to 1000°C [70].

Liu *et al*. [71] studied the bias illumination stress stability of solution-processed ultra-thin (~3 nm) ZTO TFTs.. It was found that the change in threshold voltage (ΔV_{th}) was significantly positive when ZTO TFTs were under positive bias stress (PBS, ΔV_{th} =9.98 V) and positive bias illumination stress, but ΔV_{th} was slightly negative under only light illumination stress or negative bias stress (ΔV_{th} =2.27 V). The result was attributed to the photoionization and subsequent transition of electronic states of oxygen vacancies (*i.e.*, Vo, Vo^{+}, and Vo^{++}) in ZTO. Yoon Jang

Kim *et al*.[72] also studied the photo bias instability of high-performing solution-processed a-ZTO TFTs. The effects of dark negative bias stress (NBS) and negative bias illumination stress (NBIS) on the degradation of transfer characteristics of ZTO TFTs were examined. During the study, it was found that increasing annealing temperature was able to suppress the instability caused by NBS and NBIS slightly. The dynamics of the shift of threshold voltage (V_{th}) with NBS and NBIS time for the TFTs were analyzed based on the stretched exponential relaxation model

better to comprehend the mechanism of stress time-dependent charge trapping. The Tau values (relaxation time constant) were increased with the increased annealing temperature, which was attributed to the photo-created hole trapping model and Vo transition model. It was also revealed that the densification and purification of solution processed ZTO films played a vital role in high-performance ZTO TFTs with improved photo bias stability.

Bong Seob Yang *et al*. [73] studied the effect of ozone treatment improvement of photo-bias stability of ZTO FETs. Highly improved NBIS stability was achieved in ZTO FETs after ozone treatment. The threshold voltage shifts for the ozone-treated FETs were found to be almost unchanged. Improvement in the NBIS was attributed to the decreased oxygen vacancy concentration and decrement of adsorbed oxygen under photon irradiation by Ozone treatment. It was attributed to oxygen radicals diffusing toward the bulk region of the ZTO film during the O3 treatment, which resulted in the O_3 treated device having diminished pre-existing oxygen vacancies.

Jeong *et al.* also studied bias stress stability of solution-processed ZTO TFTs [74]. The effects of bias stress on spin-coated ZTO TFTs were investigated. Positive bias stress resulted in the transfer curves' displacement in the positive direction without changing the field-effect mobility and the subthreshold behavior. However, for a negative stress , no effect was observed on the threshold voltage. The device instability was attributed to the charging and discharging the temporary trap states at the interface and in the ZTO channel region. M.S. Rajachidambaram *et al.* studied the chemistry of backchannel passivation and its effect on voltage shifts due to positive bias stress. Positive bias stress turn-on voltage (Von) shifts were highly reduced by passivation of the backchannel compared to non-passivated TFTs. It was indicated that the adsorption of molecular species on the exposed backchannel of ZTO TFTs strongly influenced observed shifts

instead of the charge injection into the dielectric or trapping due to oxygen vacancies [75]. Kim *et al.* studied the effect of the Zinc/Tin composition ratio on solution-processed ZTO TFTs' operational stability. Variation of Zinc/Tin ratio atomic composition was highly influencing the microstructure and the device performance, and the operational stability of fabricated ZTO TFTs. The significant variation of ΔV_{th} under gate bias stress appeared to be closely related to the excessive or deficient Sn content and the oxidation potentials of the metallic contents along with the ambient effects. It was found that the ZTO channel with an optimum Zn: Sn ratio resulted in improved device characteristics and performance [76].

Zhao *et al.* studied the impact of Sn precursors on solution-processed a-ZTO film and TFTs by using zinc acetate dehydrate and four other different kinds of Sn precursors, tin (II) 2-ethyl hexanoate, tin (IV) acetate, tin (II) chloride, and tin (IV) isopropoxide. With the systematic analysis of produced films and devices, it was demonstrated that Sn precursors, with various molecular geometrical configurations and organic ligands, greatly affected the thickness, density, morphology, and composition of the ZTO thin films and, hence, the performance of their Field-effect Transistors (FETs) [77].

Chen proposed improving the overall electrical performance of solution-processed TFTs by channel layer multi stacking- Sha Li *et al*. proposed TFTs. Moreover, Deuk Jong Kim *et al.* used a similar method for ZnO and IGZO, respectively [78]–[80]. In these experiments, smaller and higher concentrations of precursor solutions were spin-coated on top of each other to form a semiconducting film to fabricate TFTs. It was found that an increased number of depositions can enhance the mobility of TFTs. High mobility could be obtained by using precursors solutions of low concentrations and multiple depositions, though only one deposition only resulted in low

mobility. A new method for enhancing TFTs' electrical characteristics using solution-processed has been discussed in chapter 4 as a published journal article in Electronics Letters.

1.4 References:

[1] Ozpineci, B., & Tolbert, L. M. (2004). *Comparison of wide-bandgap semiconductors for power electronics applications*. United States. Department of Energy.

[2] Shenai, K., Scott, R. S., & Baliga, B. J. (1989). Optimum semiconductors for high-power electronics. *IEEE transactions on Electron Devices*, *36*(9), 1811-1823.

[3] Baliga, B. J. (2006). *Silicon carbide power devices*. World scientific.

[4] Pande, V. (1996). A note on ancient zinc smelting in India and China. *Indian journal of history of science*, *31*(3), 275-278.

[5] Jagadish, C., & Pearton, S. J. (Eds.). (2011). *Zinc oxide bulk, thin films and nanostructures: processing, properties, and applications*. Elsevier.

[6] Dutta, R. K., Nenavathu, B. P., Gangishetty, M. K., & Reddy, A. V. R. (2012). Studies on antibacterial activity of ZnO nanoparticles by ROS induced lipid peroxidation B Biointerfaces.

[7] Chen, B., Meng, C., Yang, Z., Li, W., Lin, S., Gu, T., ... & Tong, L. (2014). Graphene coated ZnO nanowire optical waveguides. *Optics express*, *22*(20), 24276-24285.

[8] Stadler, A. (2012). Transparent conducting oxides—an up-to-date overview. *Materials*, *5*(4), 661-683.

[9] Absor, M. A. U., Kotaka, H., Ishii, F., & Saito, M. (2014). Tunable Rashba effect on strained ZnO: First-principles density-functional study. *Applied Physics Express*, *7*(5), 053002.

[10] Hsu, Y. H., Lin, J., & Tang, W. C. (2008). RF sputtered piezoelectric zinc oxide thin film for transducer applications. *Journal of Materials Science: Materials in Electronics*, *19*(7), 653-661.

[11] Absor, M. A. U., Kotaka, H., Ishii, F., & Saito, M. (2014). Tunable Rashba effect on strained ZnO: First-principles density-functional study. *Applied Physics Express*, *7*(5), 053002.

[12] Katoh, R., Furube, A., Hara, K., Murata, S., Sugihara, H., Arakawa, H., & Tachiya, M. (2002). Efficiencies of electron injection from excited sensitizer dyes to nanocrystalline ZnO films as studied by near-IR optical absorption of injected electrons. *The Journal of Physical Chemistry B*, *106*(50), 12957-12964.

[13] Sharma, P., Kumar, S., & Sreenivas, K. (2003). Interaction of surface acoustic waves and ultraviolet light in ZnO films. *Journal of materials research*, *18*(3), 545-548.

[14] Ohashi, N., Kataoka, K., Ohgaki, T., Miyagi, T., Haneda, H., & Morinaga, K. (2003). Synthesis of zinc oxide varistors with a breakdown voltage of three volts using an intergranular glass phase in the bismuth–boron–oxide system. *Applied physics letters*, *83*(23), 4857-4859.

[15] Wang, D., Seo, H. W., Tin, C. C., Bozack, M. J., Williams, J. R., Park, M., ... & Tzeng, Y. H. (2006). Effects of postgrowth annealing treatment on the photoluminescence of zinc oxide nanorods. *Journal of Applied Physics*, *99*(11), 113509.

[16] Wei, S. H., & Zunger, A. (1988). Role of metal d states in II-VI semiconductors. *Physical Review B*, *37*(15), 8958.

[17] Udom, I. (2014). Investigation of Enhanced Titanium and Zinc Oxide Semiconductors for the Photodegradation of Aqueous Organic Compounds.

[18] Pearton, S. J., Abernathy, C. R., Overberg, M. E., Thaler, G. T., Norton, D. P., Theodoropoulou, N., ... & Boatner, L. A. (2003). Wide band gap ferromagnetic semiconductors and oxides. *Journal of Applied Physics*, *93*(1), 1-13.

[19] Look, D. C., Reynolds, D. C., Hemsky, J. W., Jones, R. L., & Sizelove, J. R. (1999). Production and annealing of electron irradiation damage in ZnO. *Applied Physics Letters*, *75*(6), 811-813.

[20] Boomer, K., Lauenstein, J. M., & Hammoud, A. (2016). Body of knowledge for silicon carbide power electronics.

[21] Özgür, Ü., Alivov, Y. I., Liu, C., Teke, A., Reshchikov, M., Doğan, S., ... & Morkoç, A. H. (2005). A comprehensive review of ZnO materials and devices. *Journal of applied physics*, *98*(4), 11.

[22] Look, D. C., Reynolds, D. C., Litton, C. W., Jones, R. L., Eason, D. B., & Cantwell, G. (2002). Characterization of homoepitaxial p-type ZnO grown by molecular beam epitaxy. *Applied physics letters*, *81*(10), 1830-1832.

[23] *Pearson, W. B. (2013). A handbook of lattice spacings and structures of metals and alloys: International series of monographs on metal physics and physical metallurgy, Vol. 4 (Vol. 4). Elsevie*r.

[24] Creagh, D. C., & McAuley, W. J. (1992). International tables for crystallography. *Vol C,(AJC Wilson, ed.), Kluwer Academic Publishers, Boston, Table*, *4*(4.3), 200-206.

[25] Li, W. J., Shi, E. W., Zhong, W. Z., & Yin, Z. W. (1999). Growth mechanism and growth habit of oxide crystals. *Journal of crystal growth*, *203*(1-2), 186-196.

[26] Jaffe, J. E., Snyder, J. A., Lin, Z., & Hess, A. C. (2000). LDA and GGA calculations for high-pressure phase transitions in ZnO and MgO. *Physical Review B*, *62*(3), 1660.

[27] Culea, E., & Nicula, A. (1986). Electrical properties of V2O5□ B2O3 glasses. *Solid state communications*, *58*(8), 545-549.

[28] Hossain, F. M., Nishii, J., Takagi, S., Ohtomo, A., Fukumura, T., Fujioka, H., ... & Kawasaki, M. (2003). Modeling and simulation of polycrystalline ZnO thin-film transistors. *Journal of Applied Physics*, *94*(12), 7768-7777.

[29] Hosono, H., Hirano, M., Ota, H., Kamiya, T., & Nomura, K. (2007). *U.S. Patent Application No. 10/592,431*.

[30] Hosono, H. (2006). Ionic amorphous oxide semiconductors: Material design, carrier transport, and device application. *Journal of non-crystalline solids*, *352*(9-20), 851-858.

[31] Kamiya, T., Nomura, K., & Hosono, H. (2010). Present status of amorphous In–Ga–Zn–O thin-film transistors. *Science and Technology of Advanced Materials*.

[32] Sung, S. Y., Kim, S. Y., Jo, K. M., Lee, J. H., Kim, J. J., Kim, S. G., ... & Heo, Y. W. (2010). Fabrication of p-channel thin-film transistors using CuO active layers deposited at low temperature. *Applied Physics Letters*, *97*(22), 222109.

[33] Yabuta, H., Sano, M., Abe, K., Aiba, T., Den, T., Kumomi, H., ... & Hosono, H. (2006). High-mobility thin-film transistor with amorphous In Ga Zn O 4 channel fabricated by room temperature rf-magnetron sputtering. *Applied physics letters*, *89*(11), 112123.

[34] Ito, M., Miyazaki, C., Ishizaki, M., Kon, M., Ikeda, N., Okubo, T., ... & Sekine, N. (2008). Application of amorphous oxide TFT to electrophoretic display. *Journal of Non-Crystalline Solids*, *354*(19-25), 2777-2782.

[35] Jeong, J. K., Jeong, J. H., Yang, H. W., Ahn, T. K., Kim, M., Kim, K. S., ... & Chung, H. K. (2009). 12.1-in. WXGA AMOLED display driven by InGaZnO thin-film transistors. *Journal of the Society for Information Display*, *17*(2), 95-100.

[36] K. (2010, November 8). *Samsung develops 70-inch LCD panel using Oxide Semiconductor tech*. Sammy Hub. https://sammyhub.com/2010/11/08/samsung-develops-70-inch-lcd-panel-using-oxide-semiconductor-tech/

[37] Münzenrieder, N., Petti, L., Zysset, C., Salvatore, G. A., Kinkeldei, T., Perumal, C., ... & Tröster, G. (2012, December). Flexible a-IGZO TFT amplifier fabricated on a free-standing polyimide foil operating at 1.2 MHz while bent to a radius of 5 mm. In *2012 International Electron Devices Meeting* (pp. 5-2). IEEE.

[38] Heremans, P., Papadopoulos, N., De Meux, A. D. J., Nag, M., Steudel, S., Rockele, M., ... & Myny, K. (2016, December). Flexible metal-oxide thin film transistor circuits for RFID and health patches. In *2016 IEEE International Electron Devices Meeting (IEDM)* (pp. 6-3). IEEE.

[39] Guang, Y., Chen-Fei, W., Hai, L., Fang-Fang, R., Rong, Z., You-Dou, Z., & Xiao-Ming, H. (2015). Frequency performance of ring oscillators based on a-IGZO thin-film transistors. *Chinese Physics Letters*, *32*(4), 047302.

[40] Liu, N., Zhu, L. Q., Feng, P., Wan, C. J., Liu, Y. H., Shi, Y., & Wan, Q. (2015). Flexible sensory platform based on oxide-based neuromorphic transistors. *Scientific reports*, *5*(1), 1-9.

[41] Bahubalindruni, P. G., Martins, J., Santa, A., Tavares, V., Martins, R., Fortunato, E., & Barquinha, P. (2018). High-gain transimpedance amplifier for flexible radiation dosimetry using InGaZnO TFTs. *IEEE Journal of the Electron Devices Society*, *6*, 760-765.

[42] Hung, M. H., Chen, C. H., Lai, Y. C., Tung, K. W., Lin, W. T., Wang, H. H., ... & Lin, Y. C. (2017, May). Ultra-low voltage 1-V RFID tag implement in a-IGZO TFT technology on plastic. In *2017 IEEE International Conference on RFID (RFID)* (pp. 193-197). IEEE.

[43] Wager, J. F., Keszler, D. A., & Presley, R. E. (2008). Devices. In *Transparent Electronics* (pp. 83-151). Springer, Boston, MA.

[44] Orita, M., Ohta, H., Hirano, M., Narushima, S., & Hosono, H. (2001). Amorphous transparent conductive oxide InGaO3 (ZnO) m (m≤ 4): a Zn4s conductor. *Philosophical magazine B*, *81*(5), 501-515.

[45] Orita, M., Tanji, H., Mizuno, M., Adachi, H., & Tanaka, I. (2000). Mechanism of electrical conductivity of transparent InGaZnO 4. *Physical Review B*, *61*(3), 1811.

[46] Orita, M., Ohta, H., Hirano, M., Hosono, H., Morita, K., Tanji, H., & Kawazoe, H. (2000). Properties of a Novel Amorphous Transparent Conductive Oxide, InGaO 3 (ZnO) m. *MRS Online Proceedings Library Archive*, *623*.

[47] Nomura, K., Kamiya, T., Ohta, H., Uruga, T., Hirano, M., & Hosono, H. (2007). Local coordination structure and electronic structure of the large electron mobility amorphous oxide semiconductor In-Ga-Zn-O: Experiment and ab initio calculations. *Physical review B*, *75*(3), 035212.

[48] Moriga, T., Kammler, D. R., Mason, T. O., Palmer, G. B., & Poeppelmeier, K. R. (1999). Electrical and optical properties of transparent conducting homologous compounds in the Indium–Gallium–Zinc Oxide system. *Journal of the American Ceramic Society*, *82*(10), 2705-2710.

[49] Nomura, K., Ohta, H., Takagi, A., Kamiya, T., Hirano, M., & Hosono, H. (2004). Room-temperature fabrication of transparent flexible thin-film transistors using amorphous oxide semiconductors. *nature*, *432*(7016), 488-492.

[50] Kamiya, T., Nomura, K., & Hosono, H. (2009). Electronic structures above mobility edges in crystalline and amorphous In-Ga-Zn-O: Percolation conduction examined by analytical model. *Journal of display technology*, *5*(12), 462-467.

[51] Kim, S. J., Yoon, S., & Kim, H. J. (2014). Review of solution-processed oxide thin-film transistors. *Japanese Journal of Applied Physics*, *53*(2S), 02BA02.

[52] Hosono, H. (2006). Ionic amorphous oxide semiconductors: Material design, carrier transport, and device application. *Journal of non-crystalline solids*, *352*(9-20), 851-858.

[53] Fortunato, E., Barquinha, P., & Martins, R. (2012). Oxide semiconductor thin-film transistors: a review of recent advances. *Advanced materials*, *24*(22), 2945-2986.

[54] Jeong, S., Ha, Y. G., Moon, J., Facchetti, A., & Marks, T. J. (2010). Role of gallium doping in dramatically lowering amorphous-oxide processing temperatures for solution-derived indium zinc oxide thin-film transistors. *Advanced Materials*, *22*(12), 1346-1350.

[55] Kim, G. H., Jeong, W. H., & Kim, H. J. (2010). Electrical characteristics of solution-processed InGaZnO thin film transistors depending on Ga concentration. *physica status solidi (a)*, *207*(7), 1677-1679.

[56] Fang, L., Liu, J., Ju, S., Zheng, F., Dong, W., & Shen, M. (2010). Experimental and theoretical evidence of enhanced ferromagnetism in sonochemical synthesized BiFeO 3 nanoparticles. *Applied Physics Letters*, *97*(24), 242501.

[57] Yao, J., Xu, N., Deng, S., Chen, J., She, J., Shieh, H. P. D., ... & Huang, Y. P. (2011). Electrical and photosensitive characteristics of a-IGZO TFTs related to oxygen vacancy. *IEEE transactions on electron devices*, *58*(4), 1121-1126.

[58] Noh, H. K., Chang, K. J., Ryu, B., & Lee, W. J. (2011). Electronic structure of oxygen-vacancy defects in amorphous In-Ga-Zn-O semiconductors. *Physical Review B*, *84*(11), 115205.

[59] Kamiya, T., Nomura, K., & Hosono, H. (2010). Present status of amorphous In–Ga–Zn–O thin-film transistors. *Science and Technology of Advanced Materials*.

[60] Gorrn, P., Sander, M., Meyer, J., Kroger, M., & Becker, E. (2006). H.-. H. Johannes, W. Kowalsky, and T. Riedl. *Adv. Mater*, *18*, 738.

[61] Jackson, W. B., Hoffman, R. L., & Herman, G. S. (2005). High-performance flexible zinc tin oxide field-effect transistors. *Applied physics letters*, *87*(19), 193503.

[62] Chang, Y. J., Lee, D. H., Herman, G. S., & Chang, C. H. (2007). High-performance, spin-coated zinc tin oxide thin-film transistors. *Electrochemical and Solid-State Letters*, *10*(5), H135.

[63] Chiang, H. Q., Wager, J. F., Hoffman, R. L., Jeong, J., & Keszler, D. A. (2005). High mobility transparent thin-film transistors with amorphous zinc tin oxide channel layer. *Applied Physics Letters*, *86*(1), 013503.

[64] Hong, D., Chiang, H. Q., & Wager, J. F. (2006). Zinc tin oxide thin-film transistors via reactive sputtering using a metal target. *Journal of Vacuum Science & Technology B: Microelectronics and Nanometer Structures Processing, Measurement, and Phenomena*, *24*(5), L23-L25.

[65] Lee, C. G., Dutta, S., & Dodabalapur, A. (2010). Solution-processed ZTO TFTs with recessed gate and low operating voltage. *IEEE electron device letters*, *31*(12), 1410-1412.

[66] Kim, D., Jeong, Y., Song, K., Park, S. K., Cao, G., & Moon, J. (2009). Inkjet-printed zinc tin oxide thin-film transistor. *Langmuir*, *25*(18), 11149-11154.

[67] Park, J., Song, I., Kim, S., Kim, S., Kim, C., Lee, J., ... & Yin, H. (2008). K.. Kim, K.. Kwon, and Y. Park,"Self-aligned top-gate amorphous gallium indium zinc oxide thin film transistors,". *Applied Physics Letters*, *93*(5).

[68] Branquinho, R., Salgueiro, D., Santa, A., Kiazadeh, A., Barquinha, P., Pereira, L., ... & Fortunato, E. (2015). Towards environmental friendly solution-based ZTO/AlOx TFTs. *Semiconductor Science and Technology*, *30*(2), 024007.

[69] Hong, D., & Wager, J. F. (2005). Passivation of zinc–tin–oxide thin-film transistors. *Journal of Vacuum Science & Technology B: Microelectronics and Nanometer Structures Processing, Measurement, and Phenomena*, *23*(6), L25-L27.

[70] Yuan, H. L., & Li, J. C. (2017). Effect of annealing temperature on the growth of Zn-Sn-O nanocomposite thin films. *Journal of Alloys and Compounds*, *714*, 114-119.

[71] Liu, L. C., Chen, J. S., & Jeng, J. S. (2014). Role of oxygen vacancies on the bias illumination stress stability of solution-processed zinc tin oxide thin film transistors. *Applied Physics Letters*, *105*(2), 023509.

[72] Kim, Y. J., Yang, B. S., Oh, S., Han, S. J., Lee, H. W., Heo, J., ... & Kim, H. J. (2013). Photobias instability of high performance solution processed amorphous zinc tin oxide transistors. *ACS applied materials & interfaces*, *5*(8), 3255-3261.

[73] Yang, B. S., Park, S., Oh, S., Kim, Y. J., Jeong, J. K., Hwang, C. S., & Kim, H. J. (2012). Improvement of the photo-bias stability of the Zn–Sn–O field effect transistors by an ozone treatment. *Journal of Materials Chemistry*, *22*(22), 10994-10998.

[74] Jeong, Y., Song, K., Kim, D., Koo, C. Y., & Moon, J. (2009). Bias stress stability of solution-processed zinc tin oxide thin-film transistors. *Journal of The Electrochemical Society*, *156*(11), H808.

[75] Rajachidambaram, M. S., Pandey, A., Vilayurganapathy, S., Nachimuthu, P., Thevuthasan, S., & Herman, G. S. (2013). Improved stability of amorphous zinc tin oxide thin film transistors using molecular passivation. *Applied Physics Letters*, *103*(17), 171602.

[76] Kim, Y. H., Han, J. I., & Park, S. K. (2011). Effect of zinc/tin composition ratio on the operational stability of solution-processed zinc–tin–oxide thin-film transistors. *IEEE electron device letters*, *33*(1), 50-52.

[77] Zhao, Y., Dong, G., Duan, L., Qiao, J., Zhang, D., Wang, L., & Qiu, Y. (2012). Impacts of Sn precursors on solution-processed amorphous zinc–tin oxide films and their transistors. *RSC advances*, *2*(12), 5307-5313.

[78] Li, C. S., Li, Y. N., Wu, Y. L., Ong, B. S., & Loutfy, R. O. (2009). Fabrication conditions for solution-processed high-mobility ZnO thin-film transistors. *Journal of Materials Chemistry*, *19*(11), 1626-1634.

[79] Hong, S., Park, J. W., Kim, H. J., Kim, Y. G., & Kim, H. J. (2016). A review of multi-stacked active-layer structures for solution-processed oxide semiconductor thin-film transistors. *Journal of Information Display*, *17*(3), 93-101.

[80] Kim, D. J., Kim, D. L., Rim, Y. S., Kim, C. H., Jeong, W. H., Lim, H. S., & Kim, H. J. (2012). Improved electrical performance of an oxide thin-film transistor having multistacked active layers using a solution process. *ACS applied materials & interfaces*, *4*(8), 4001-4005.

Chapter 2

Overview of Metal Oxide Field Effect transistors (MOSFET) and Thin-Film Transistors (TFTs):

2.1 Introduction:

The necessity of reducing size and power consumption in transistors limited the use of Bipolar junction Transistors (BJTs). Field-Effect Transistors (FETs), mainly Metal Oxide Semiconductor Field Effect Transistors (MOSFETs) and Junction Field Effect Transistors (JFETs), alleviated the introduction of insulating dielectrics reduced the BJT's limitations such as low power operation restriction into the substrate. This resulted in the advent of JFETs and MOSFETs into modern electronics. Both MOSFETs and JFETs are a type of semiconductor unipolar devices which are widely used for switching and amplifying electrical signals in electronic devices. Both are voltage-controlled FETs. They use an electric field to control the electrical conductivity of a channel.

JFET is the simplest type of FET in which the current can either pass from source to drain or vice versa. Unlike BJTs, it uses the voltage applied to the gate terminal to control the current flowing *via* the channel between the drain and source terminals resulting in an output current being proportional to the input voltage. It is a three-terminal device that can only operate in depletion mode. MOSFETs are the core of integrated circuits (ICs), and they can be fabricated in a single chip due to their tiny sizes. The MOSFET is a four-terminal device with source (S), Drain (D), Gate (G), and body (B) terminals. Usually, the MOSFET body is connected to the source terminal, making it a three-terminal device resembling a Field Effect Transistor (FET).

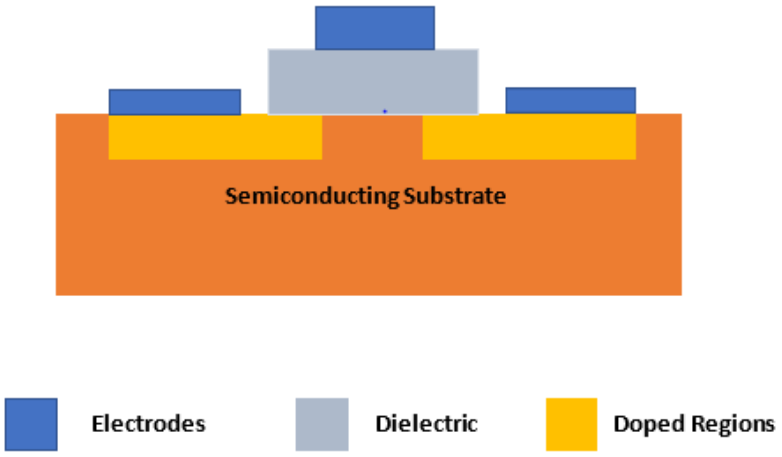

Figure 2.1: MOSFET schematic diagram

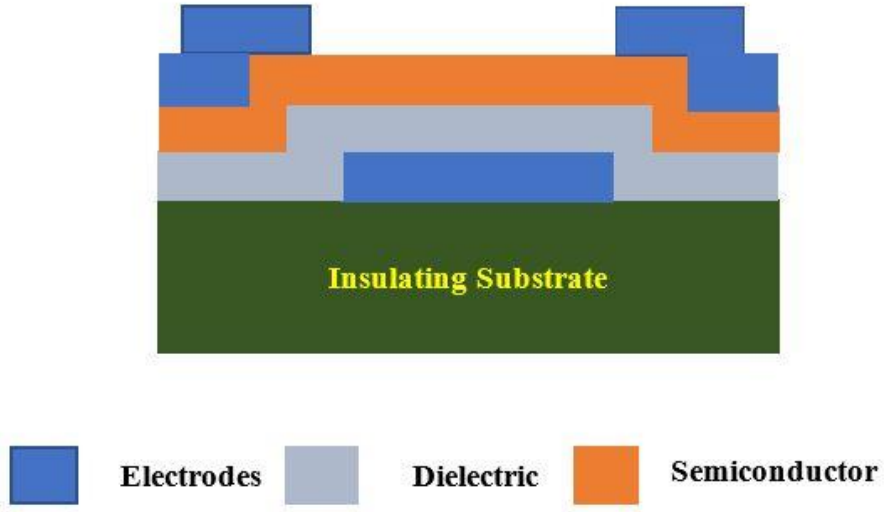

Figure 2.2: Thin Film Transistor schematic diagram

Insulated Gate Field Effect Transistor (IGFET) or Metal Oxide field-effect Transistor (MOSFET) is a voltage-controlled FET. It differs from a Junction field-effect transistor (JFET) because it possesses a "Metal Oxide" Gate electrode, electrically insulated from the semiconductor n or p channel material by a very thin layer of insulator usually Silicon dioxide. It can operate in both modes, depletion, and enhancement. As the name suggests, the majority charge carriers' movement in a MOSFET is controlled by the voltage applied on the gate electrode. The field

produced by the gate voltage modulates the channel's conductivity between the primary current carrying terminals, namely called Drain (D) and Source (S). MOSFETs can be of two types: depletion and enhancement. Both can either be n-channel or p channel types depending upon the nature of the semiconductor.

Depletion Type: The depletion type MOSFET is equivalent to a “NORMALLY ON” switch. The depletion type of transistors requires the gate-source voltage to switch off the device. For a channel depletion MOSFET, a negative bias will deplete (thus its name) the conductive channel of its free electrons switching the transistors off. Likewise, for a p channel MOSFET, a positive bias will deplete the channel of its free holes, turning it off. The symbols for depletion-mode MOSFETs in both N-channel and P-channel types are shown in Figures 2 a & b. In the figure, the fourth terminal is connected to the ground, but in separate MOSFETs, it is connected to the source terminal. The continuous thick line connected between the drain and the source terminal represents the depletion type. The arrow symbol indicates the channel type. The depletion type MOSFETs are usually ON at zero bias voltage. Compared to the enhancement MOSFETS, the channel conductivity in depletion MOSFET is lower.

Enhancement Type: The enhancement type MOSFETs are equivalent to the “NORMALLY OFF” switch, and these types of transistors require voltage to switch ON the device. The conducting channel is lightly doped or even undoped, making it nonconductive, which results in the device being normally off when the gate bias is zero. A drain current can only flow when a gate voltage is applied to the gate terminal higher than the threshold voltage for an n channel MOS enhancement transistor. The application of positive bias as the gate to an n-type transistor attracts more electrons towards the oxide layer near the gate, henceforth increasing the

channel's thickness allowing more current to flow. Hence the name enhancement type as the application of a gate voltage enhances the channel.

The transistors fabricated and used in this research mostly belong to this category of transistors. The symbols of both N and P channel enhancement mode MOSFET are shown in Figures 2 c & d. The broken line connected between the S and D represents the enhancement type. The channel is established between the source and drain in the opposite type of the substrate, i.e., N- channel is made with a P-type substrate and *vice versa*. The conductivity of the channel due to holes and electrons depends upon the P-type and N-type channels, respectively. Enhancement mode MOSFETs make excellent electronics owing to their low "ON" resistance and extremely high "OFF" resistance in addition to their infinitely high input resistance due to their isolated gate. Enhancement mode MOSFETs are used in ICs to fabricate Complementary Metal Oxide Semiconductor (CMOS) type logic gates and power switching circuits in the form of PMOS and NMOS gates.

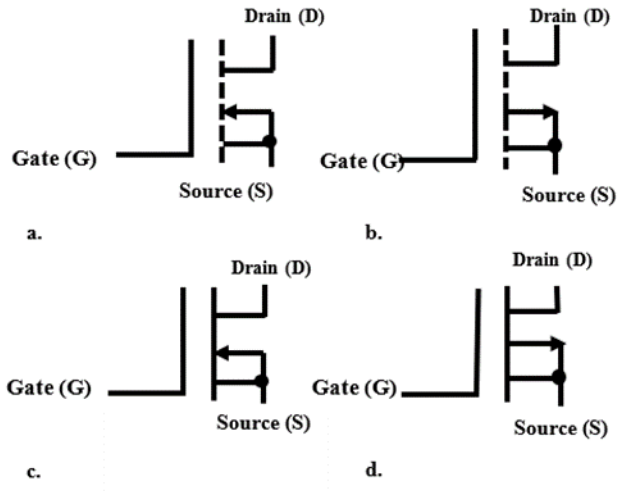

Figure 2.3: . a) N-channel enhancement type MOSFET b) P-channel enhancement type MOSFET c) N-channel depletion type MOSFET d) P- channel depletion type MOSFET

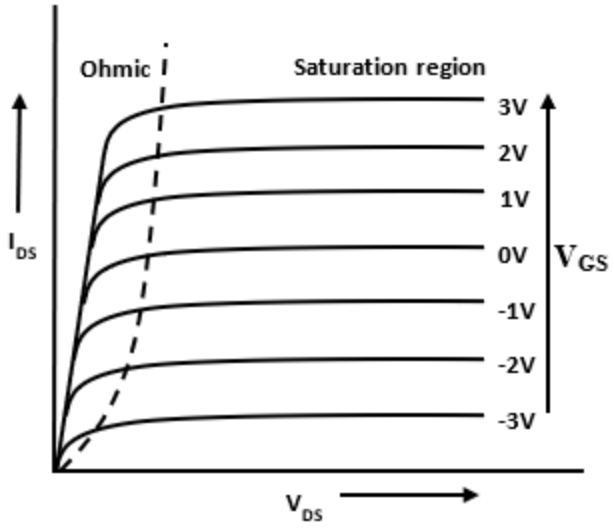

Figure 2.4: Output characteristics of depletion type MOSFET

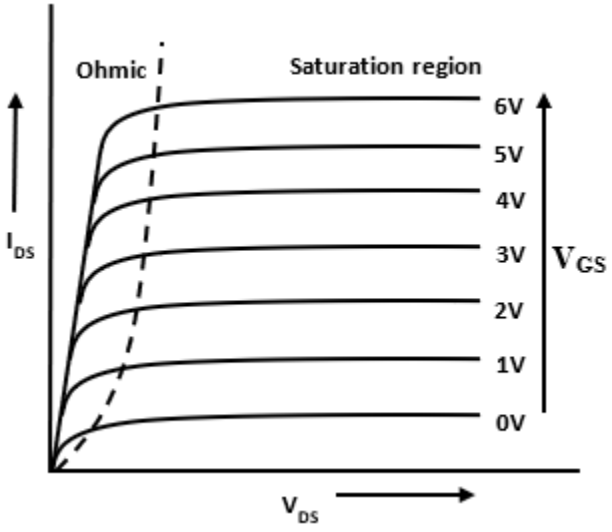

Figure 2.5: Output characteristics of depletion type MOSFET

The different operating regions in which the MOSFET are discussed below:

Cut Off region: If the gate-source voltage is less than the threshold voltage, then the transistor is meant to be operating in the cut-off region also "fully off." In a thin region drain current is zero, and the transistor acts as an open switch.

Ohmic Region: If the gate-source voltage is greater than the threshold voltage and the drain-source voltage lies between the threshold voltage and (V_{GS}- V_{th}), then the transistor is said to be working in the linear region or the Ohmic region. The transistor acts as a variable resistor at this state.

Saturation Region: If the gate voltage is much greater than the threshold voltage and the drain current is at its maximum, and the transistor is fully ON, then the transistor is said to be in the saturation region. In this state, it acts as a closed switch.

Table 2.1: The behavior of MOSFET in enhancement and depletion modes depending upon the gate voltage is summarized

MOSFET TYPE	**V_{GS}= +ve**	**V_{GS} = 0**	**V_{GS} = -ve**
N- channel depletion	ON	ON	OFF
N-channel enhancement	ON	OFF	OFF
P- channel depletion	OFF	ON	OFF
P- channel enhancement	OFF	OFF	ON

The TFTs are a special kind of field-effect transistors (FETs) and are different in some respects as compared to conventional MOS transistors, where the substrate is usually a semiconductor. A thin film of a semiconductor layer is generally deposited on a foreign substrate in TFTs to fabricate TFTs. The inception of Field Effect Transistors was first introduced after the patent was filed by Lilienfeld in the 1930s [1].

The most technical name for these kinds of devices is “Thin-film insulated-gate field-effect transistors.” Weimer used the more straightforward term “thin-film transistor in a top gate structure with a channel film of ploy Cadmium Sulfide (CdS) to elucidate the first successful vacuum-deposited field-effect device fabricated in 1961 [2]. Since Weimer’s initial work, TFTs structure, fabrication, integration, and materials systems used and employed have gone through extensive change, development, and refinement. TFTs have been fabricated using CdS, CdSe, amorphous hydrogenated silicon (a-Si: H), and polycrystalline Silicon as the channel material. The most extensively used application of TFTs is as switching transistors for active-matrix liquid crystal displays (AMLCD), and the channel material of choice is a-Si: H and poly-Si. The general characteristics of these technologies have mobilities in the range of 0.5 – 1.0 cm^2/V. s and 10 – 80 cm^2/V. s For a-Si:H and poly-Si, respectively with maximum processing temperatures, are 300 °C and 500 – 600 °C, respectively [3].

Owing to the limitations of a-Si:H and poly-Si with lower mobility and difficulty for large-sized fabrication for the high-temperature process, respectively, it necessitated using novel semiconductor layers instead of a-Si:H and poly-Si. Metal Oxide semiconductors, because of their properties such as high field-effect mobility, transparency, good uniformity, and easy fabrication at room temperature (RT), have been much researched as a possible alternative to the before-mentioned semiconductors. In addition to Si-based TFTs [4]–[6], other TFTs, MOS-based [7]–[10], organic materials based, polymers based TFTs have been studied recently by researchers. Table 2.2 shows the comparison of TFTs characteristics fabricated by different kinds of semiconducting layers. In this dissertation, we mainly focus on the TFTs using the ZTO semiconducting layer.

Table 2.2: Comparison of available TFT technologies

	Poly-Si TFTs	a-Si:H TFTs	Polymer Organic TFTs	Organic TFTs	AOS TFTs
Circuit type	CMOS	NMOS	NMOS	PMOS	NMOS
Mobility	Good	Poor	Good	Poor	Good
Transparency (%)	<20	<20	>80	>80	>80
Uniformity	Fair	Good	Medium	Good	Good
Reliability	Medium/High	Low	Low	Medium	High
Processing temperature	High	Low	Low	Low	Low
Cost	High	Low	Low	Low	Low
Leakage Current	Medium	Low	Medium	Medium	Low

2.2 Thin Film Transistor Device Structures:

TFTs structures are mainly categorized as staggered or co-planar. They can either be bottom gated or top gated devices. In this dissertation, we use bottom gated TFTs. Figure 2.6 shows different possible device structures. Their common difference lies in the position of the gate,

source/drain, the semiconductor, and the insulator. A staggered TFT structure has the gate and S/D contacts on the opposite sides of the semiconductor, and thus there is no direct connection with the induced channel in the semiconductor. While this sort of arrangement provides a large area for contact for the source and drain for charge injection, the coplanar structure has the gate, source, and drain contacts on the same side of the semiconductor. This arrangement leads to the source and drain contacts to be in direct contact with the induced channel.

In bottom gated or inverted TFT structure, the gate electrode and the gate insulator lie beneath the semiconductor, which in turn leads to the top surface of the semiconductor to be exposed to the ambient. In a top-gated structure, the gate electrode and the insulator are present on top of the semiconductor. In this arrangement, the semiconductor is covered by the insulator, and thus the surface is innately passivated.

Process flow and process integration can also determine the right kind of TFT structure for the application. In top-gate structures, the insulator is deposited after the semiconductor layer, which implies that during the deposition of the insulator, extra care must be taken to avoid the damage of the semiconductor near the interface. In the coplanar structures, the semiconductor is deposited first, and hence the maximum processing temperature is constrained only by the semiconductor and the substrate. A bottom gate structure would come in handy to resolve such issues where the insulator is prepared before the semiconductor deposition. Amorphous hydrogenated Silicon Technology is hard to be realized with the co-planar structure. Generally, the staggered configuration is employed in the fabrication of amorphous silicon TFTs, while the co-planar design is used to realize polycrystalline silicon TFTs. The staggered bottom gate TFTs are extensively used in the manufacturing of AMLCDs backplanes [11].

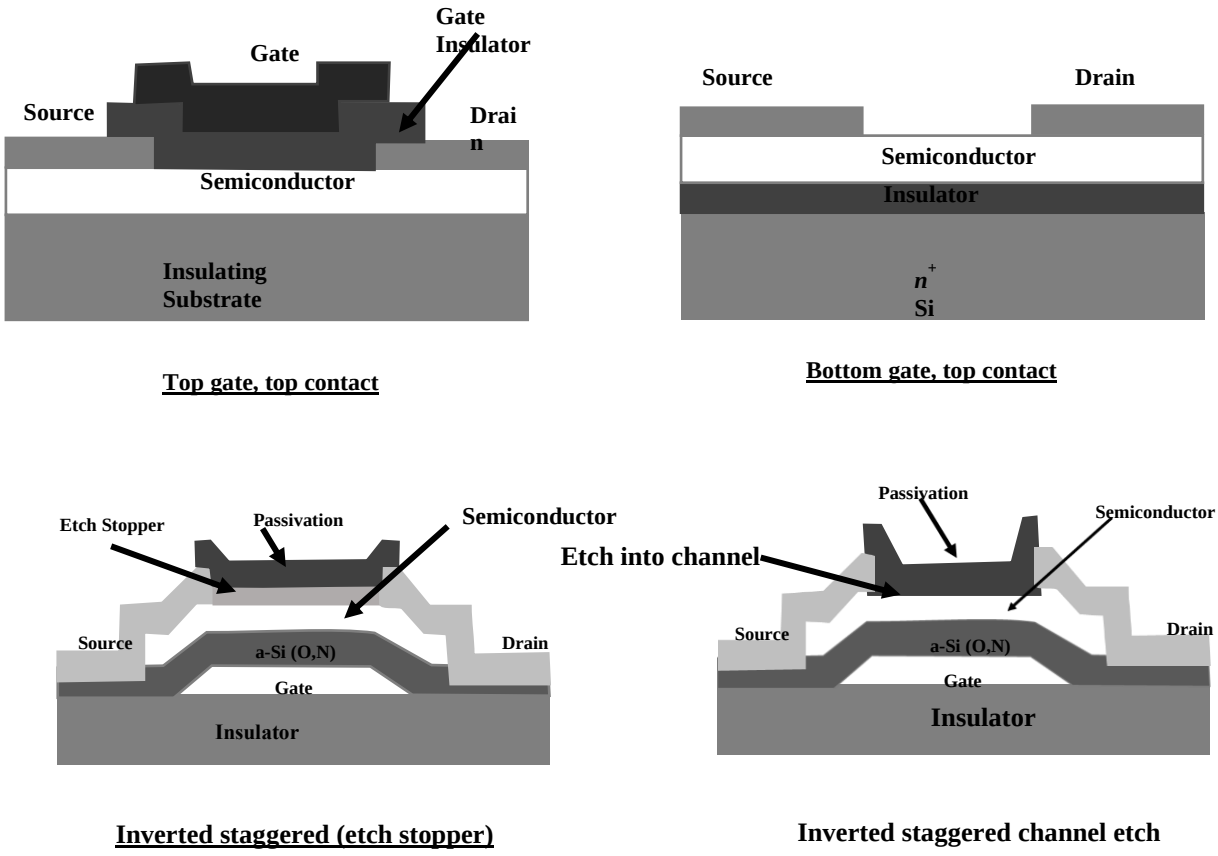

Figure 2.6: Device Structure for Thin Film Transistors

2.3 Basic Device Operation:

In this dissertation, an n-channel enhancement mode TFT is assumed. Figure 2.7 shows the basic structure of n-type semiconductor TFT and energy band diagrams with the gate bias [12]. Figure 5 (a) shows the device in an equilibrium state with 0V gate bias. Figure 5 (b) shows an energy band diagram with a negative bias on the gate. The applied negative voltage bias repels the mobile electrons from the channel region at the interface between the dielectric and channel layer. The absence of mobile electrons in the channel creates a depletion region in the semiconductor layer, decreasing the conductance of the semiconducting layer and restrain the flow of current from

source to drain. Figure 5 (c)shows the TFT energy band diagram when a positive gate bias is applied.

In this case, the mobile electrons are attracted to the channel region, and the device is said to be working on “accumulation mode.” The channel layer accumulates mobile electrons, and the resistivity of the channel is highly reduced, making the channel layer conductive. When applied with positive gate bias, devices result in a high current between the source to drain electrodes.

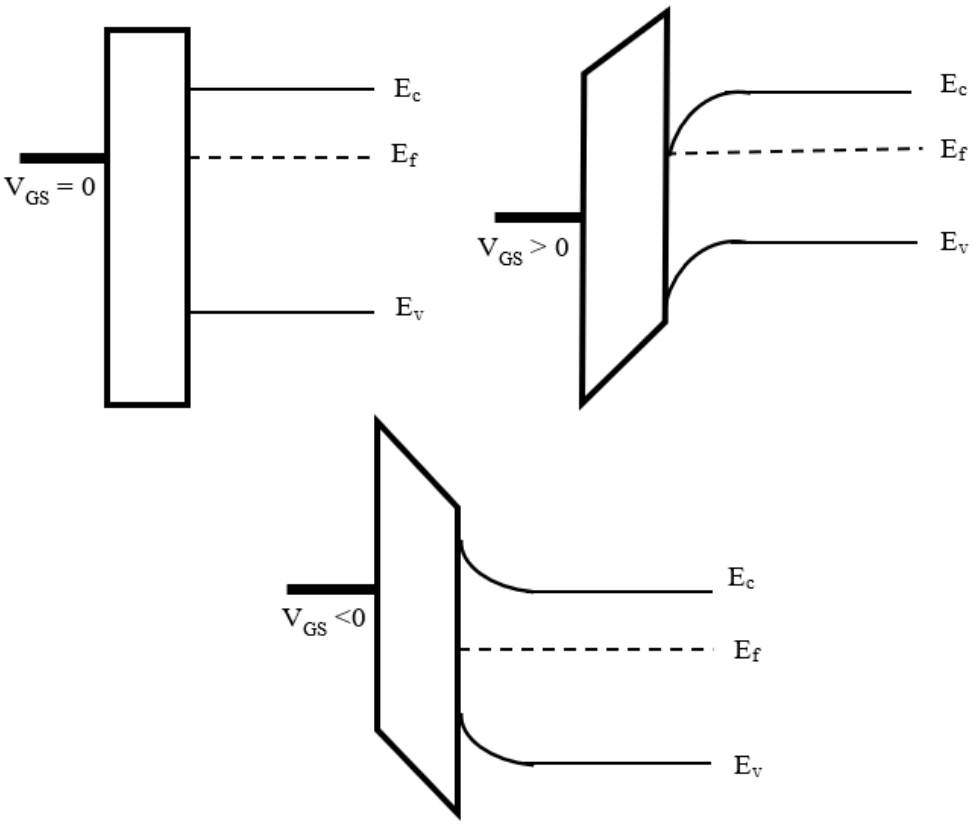

Figure 2.7: Energy band diagram of n-type semiconductor under gate bias

The section 2.3.1 discusses the critical TFT figures-of-merit, field-effect mobility (μ_{FE}), the threshold voltage (V_{th}), subthreshold swing (SS), and slope (SS) and current on-off ratio (I_{ON}/I_{OFF}).

2.4 Electrical Characteristics of Thin Film Transistors (TFTs):

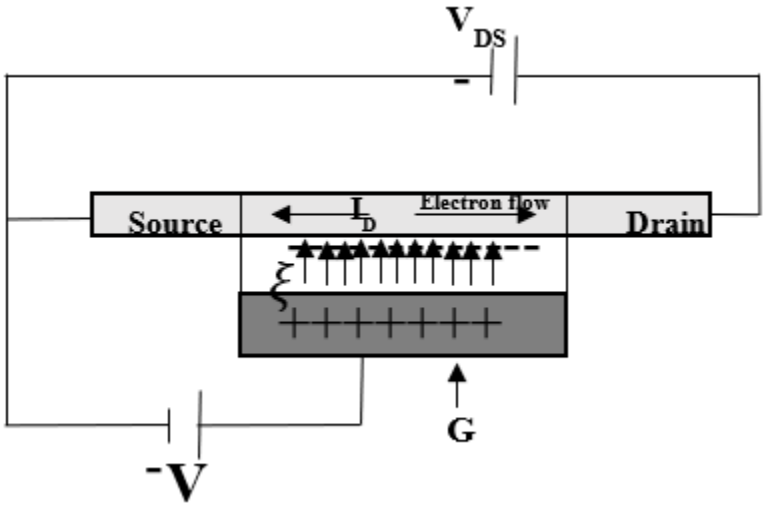

Figure 2.8: Schematic Illustration of the central elements of TFT operation

2.4.1 Threshold Voltage:

TFT operation is generally quantified in the form of the drain current (I_D) as a function of the gate to source voltage (V_{GS}) and drain to source voltage (V_{DS}). Owing to the appropriate selection of simplified assumptions, the well-recognized ideal MISFET equation is obtained as follows

$$I_D = \begin{cases} 0 & \ldots\ldots \quad V_{GS} \leq V_{th} \\ \mu C_{ins} \dfrac{w}{L} \left\{ (V_{GS} - V_{th}) V_{DS} \dfrac{-V_{DS}^2}{2} \right\} & \ldots\ldots \quad V_{DS} \leq V_{GS} - V_{th} \\ \dfrac{1}{2} \mu C_{ins} \dfrac{w}{L} \{ (V_{GS} - V_{\mathrm{th}})^2 \} & \ldots\ldots \quad V_{DS} > V_{GS} - V_{th} \end{cases} \qquad 2.1$$

The threshold voltage (V_{th}) is a widely used TFT parameter to quantify turn-on voltage, as per the ideal TFT model. However, in the case of ZTO or any other ZnO-based TFTs, it is not precisely possible to define and quantify the measured electrical characteristic defined by equation 2.1.

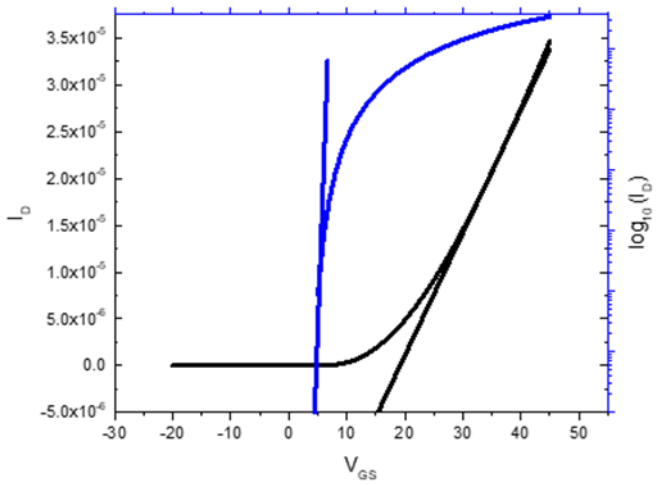

Figure 2.9: Linear extrapolation of the ID Vs. VGS curve for the extraction of threshold voltage V_{th} and V_{on}

The dependence of channel mobility on the gate is one of the sources of deviation, which calls into question the validity of threshold voltage extraction based on direct manipulation of equation 2.1 [13]. Some other non-idealities might also be present and need to be suitably accounted for to model the TFT behavior precisely. These non-idealities comprise, but are not

restricted to, traps at the semiconductor/insulator interface, subthreshold conduction, interface roughness, conductive channel, channel length modulation, gate leakage, etc.

Moreover, V_{th} can be estimated graphically by plotting the TFT output conductance, transconductance (g_m) a function of V_{GS}. The drain current is given by equation 2.1where W is the width of the TFT, L is the length between the source and drain, μ is the mobility in the channel, $C_{ins}$is the capacitance of the insulator, V_{DS} and V_{GS} being the drain to source voltage and gate to source voltage respectively. The output or transconductance are obtained by differentiating equation 2.1 with respect to V_{GS} as

$$g_m = \frac{\partial(I_D)}{\partial V_{Gs}} = \mu C_{inS} \frac{W}{L} V_{DS} \qquad 2.2$$

2.4.2 Mobility:

In combination with the threshold voltage and turn-on voltage, mobility adds to the minimal set of the parameters generally used to quantify basic TFTs' electrical performance. Mobility supplies a measure of the efficiency with which the charge carriers (electrons for ZTO) move from source to drain through the semiconducting channel. To be precise, mobility is defined as the constant of proportionality between the average electron drift velocity (v_d) and the strength of the applied electric field (ξ), *i.e.* $v_d = \mu\ \xi$ [14]. Mobility involves a useful TFT performance metric, both current driving capability and maximum operating frequency. These are the two of basic TFT performance criteria and are directly proportional to mobility [13]. Thus, a precise assessment of mobility is crucial to providing an explicit characterization of TFT performance.

2.4.2.1 Mobility extraction methodology:

The usual approach for the evaluation of TFT mobility lies on fitting of the measured Current-Voltage data to one of the several expressions obtained through manipulation of the ideal transistor equation 2.1, hence yielding three typically reported FET mobility types, namely, field-effect (μ_{FE}), saturation mobility (μ_S) and effective mobility (μ_{eff}). A brief description of conventional all three TFT mobilities extraction methods is listed below.

Field-effect mobility (μ_{FE}) is procured from measured I_D-V_{GS} data with small fixed V_{DS} such the device operates in the linear region, satisfying equation 2.2. Following either transconductance (g_m) or drain conductance (g_{ds}). In the case of transconductance, differentiating equation (2.2) with respect to VGS and re-arranging the resulting expression which yields

$$\mu_{FE}(V_{GS}) = \frac{g_m[v_{GS}]}{C_{ins}\frac{W}{L}v_{DS}} \qquad 2.3$$

Where μ (V_{GS}) and g_m (V_{GS}) indicate the functional dependence of μ and gm on V_{GS}. Alternatively, Equation 2.1may be differentiated with respect to $V_{DS,}$ which yields the drain conductance (g_d) which further differentiating with respect to V_{GS} assuming μ to be independent of V_{GS}) and rearranging yields

$$\mu_{FE}(V_{GS}) = \frac{g'_d(V_{GS})}{C_{ins}\frac{W}{L}} \qquad 2.4$$

where g'_dindicates the derivative of $g_d$with respect to V_{GS}. Thus μ_{FE} can be obtained by calculating either g_m or $g'_d$from a measured I_D-V_{GS} data set with a small V_{DS} satisfying the assumptions of equation 2.1.

However, while calculating saturation mobility (μ_{sat}), a large V_{DS} is required for the device to operate in the saturation region (i.e., $V_{DS} > V_{GS} - V_{th}$). In this case, the ideal model equation suggests that the square root of the drain current in saturation ($I_{D,sat}$) becomes,

$$\sqrt{I_{D,Sat}} = \sqrt{\frac{1}{2}\mu C_{ins}\frac{w}{L}}(V_{GS} - V_{th}) \qquad 2.5$$

Taking the derivative of Equation 2.5 with respect to $V_{GS,}$ assuming μ to be independent of V_{GS}, and rearranging yields the saturation mobility.

$$\mu_{sat}(V_{Gs}) = \frac{(\frac{d\sqrt{ID,sat}}{dVGs})^2}{\frac{1}{2}\mu\, Cins\frac{W}{L}} \qquad 2.6$$

Substitution of measured $I_{D,sa}$t-V_{GS} data into Equation 2.6 then, gives μ_{sat} as a function of V_{GS}.

2.4.3 Drain Current On/OFF ratio:

Another additional performance metric often included in TFT characterization is the on/ off ratio, the ratio of maximum to minimum drain current (ID) for a fixed, typically, and relatively large drain to source voltage.

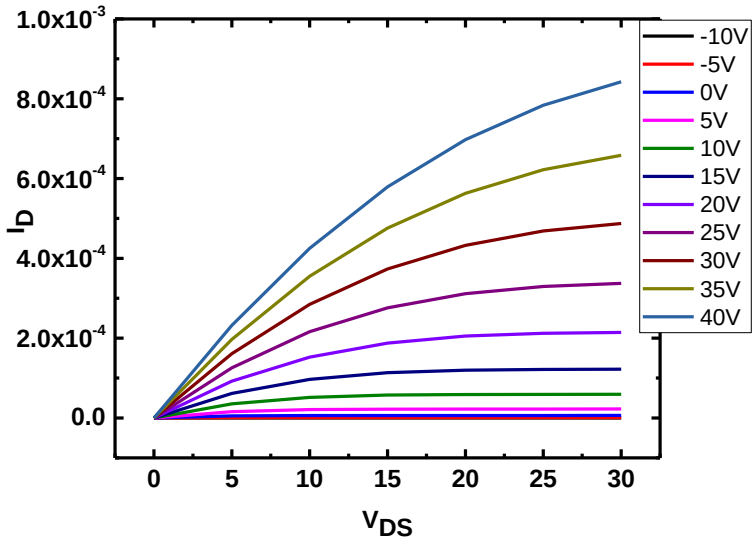

Figure 2.10: Drain current vs. drain-to-source voltage (I_D-V_{DS}) curves for the ZTO TFT with I_D-V_{DS}. V_{GS} =-10 V to 40V in 5V increments, I_D increases with increasing VGS. On/Off ratio as obtained from the data is 10^7

2.4.4 Subthreshold Slope/Swing:

An additional performance metric often included in the TFT characterization is the Subthreshold slope/swing. The subthreshold slope is the direct derivative of the log of current with respect to the gate voltage. SS swing is the inverse of the SS slope.

The subthreshold slope S of a transistor was obtained using the following definition.

$$SS = \frac{\partial \log_{10}(I_{DS})}{\partial V_{GS}} \qquad 2.7$$

SS is given by the maximum slope in the transfer curve.

In addition to the parameters as mentioned earlier, another important parameter, Interface trap density, can be calculated using the following equation:

$$D_{it} = \left[\frac{SS \log e}{kT/q} - 1\right] \frac{Cox}{q} \qquad 2.8$$

where k is Boltzmann constant, q is the elementary electron charge and T is the absolution temperature.

2.5 References:

[1] Chih-Tang, S. (1988). Evolution of the MOS transistor-from conception to VLSI. *Proceedings of the IEEE*, *76*(10), 1280-1326.

[2] Tickle, A. C. (1969). Thin-film transistors: a new approach to microelectronics.

[3] Kagan, C. R., & Andry, P. (Eds.). (2003). *Thin-film transistors*. CRC Press.

[4]S. Y. Yoon *et al*., "Mater. & Eng. Mater. & Eng. A179/A180, 426, 1994."

[5] Lee, S. W., & Joo, S. K. (1996). Low temperature poly-Si thin-film transistor fabrication by metal-induced lateral crystallization. *IEEE Electron Device Letters*, *17*(4), 160-162.

[6] Shimizu, K., Sugiura, O., & Matsumura, M. (1993). High-mobility poly-Si thin-film transistors fabricated by a novel excimer laser crystallization method. *IEEE Transactions on Electron Devices*, *40*(1), 112-117.

[7] Nomura, K., Ohta, H., Takagi, A., Kamiya, T., Hirano, M., & Hosono, H. (2004). Room-temperature fabrication of transparent flexible thin-film transistors using amorphous oxide semiconductors. *nature*, *432*(7016), 488-492.

[8] Han, S. Y., Herman, G. S., & Chang, C. H. (2011). Low-temperature, high-performance, solution-processed indium oxide thin-film transistors. *Journal of the American Chemical Society*, *133*(14), 5166-5169.

[9] Nomura, K., Ohta, H., Ueda, K., Kamiya, T., Hirano, M., & Hosono, H. (2003). Thin-film transistor fabricated in single-crystalline transparent oxide semiconductor. *Science*, *300*(5623), 1269-1272.

[10] Chang, Y. J., Lee, D. H., Herman, G. S., & Chang, C. H. (2007). High-performance, spin-coated zinc tin oxide thin-film transistors. *Electrochemical and Solid State Letters*, *10*(5), H135.

[11] Amundson, K., Ewing, J., Kazlas, P., McCarthy, R., Albert, J. D., Zehner, R., ... & Baldwin, K. (2001, June). 12.3: Flexible, Active-Matrix Display Constructed Using a Microencapsulated Electrophoretic Material and an Organic-Semiconductor-Based Backplane. In *SID Symposium Digest of Technical Papers* (Vol. 32, No. 1, pp. 160-163). Oxford, UK: Blackwell Publishing Ltd.

[12] Bao, Z., Dodabalapur, A., & Lovinger, A. J. (1996). Soluble and processable regioregular poly (3-hexylthiophene) for thin film field-effect transistor applications with high mobility. *Applied Physics Letters*, *69*(26), 4108-4110.

[13] Jagadish, C., & Pearton, S. J. (Eds.). (2011). *Zinc oxide bulk, thin films and nanostructures: processing, properties, and applications*. Elsevier.

[14]Sze, S. M., Li, Y., & Ng, K. K. (2021). *Physics of semiconductor devices*. John wiley & sons.

Chapter 3

Device Processing and Material Characterization

In this chapter, a summary of the process involved in the fabrication of ZTO TFTs is presented. The general theoretical background of the device processing and the detailed description of the primary experimental procedures are briefly described.

3.1 Growth of ZTO films:

Table 3.1: Summary of device characteristics of ZTO TFTs fabricated by different film deposition techniques

Technique	Annealing temperature (ºC)	Mobility (cm^2 /V. s)	V_{TH} (V)	On/OFF ratio
Sol-gel	500	14	1.71	10^8
PLD	N/A	10	N/A	10^6
Ink Jet	500	0.58	10	10^7
RF sputtered	600	16-26	N/A	10^7

ZTO thin films can be grown by a plethora of methods such as sol-gel process [1]–[5], spray pyrolysis [6], Pulsed Laser Deposition (PLD) [7], Inkjet-printed [8], and radio frequency (RF) magnetron sputtering [9]. Every method used to grow thin films of ZTO has its pros and cons. For example, growth methods like PLD, CVD, MBE are known to produce high-quality thin films. However, these instruments require expensive instrumentation and severely controlled ambient. Spray pyrolysis, sol-gel, and inkjet printing are the deposition techniques that use a solution-based approach.

The advantages of the solution process approach lie in its low-cost instrumentation and the capability to deposit on very large substrates. In this dissertation work, a sol-gel approach to the deposition of ZTO thin films on a p-doped Si substrate will be discussed. Table 3.1 shows the summary of device characteristics of ZTO TFTs fabricated with various deposition methods.

3.2 Sol-gel Process:

3.2.1 ZTO Sol-gel Preparation:

Zinc acetate dihydrate ($Zn(CH_3COO)_2.2H_2O$), Tin Chloride dihydrate ($SnCl_2.2H_2O$), 2-methoxyethanol ($C_3H_8O_2$), and monoethanolamine ($(HO(CH_2)2NH_2$) are used in the sol-gel preparation. Zinc acetate dihydrate and tin chloride dihydrate are the metal precursors, while 2-methoxyethanol a solvent, and monoethanolamine (MEA) is a stabilizer.

In this dissertation work, the Zinc to Tin ratio for the solution is maintained at 7:3. For the first project, two different molar concentration of the solution is used for the same volume of the solvent. First, we take 20ml of 2-methoxyethanol and add 0.6146 grams of Zinc Acetate dihydrate and 0.27grams of Tin chloride dihydrate to make a sol-gel solution for 0.2M concentration of the solution. We also take 20 ml of 2- methoxy ethanol and add 0.153grams of Zinc acetate dihydrate and 0.06grams of tin chloride dihydrate to make a 0.05M solution. We then add MEA to stabilize the solution. Also, MEA, since being an amine increases the pH value of the solution to enhance the ZTO formation.

The amount of Zinc acetate and tin chloride to be added in the solution is calculated as follows.

Of Zn acetate = (MW of Zn acetate dihydrate (219.5) ×20ml of 2-methoxyethanol ×0.2 ×0.7)/1000

Of Sn chloride acetate = (MW of Tin chloride dihydrate (225.65) ×20ml of 2-methoxyethanol ×0.2M ×0.3)/1000

Amount of MEA to be added into the solution is calculated as:

$C_1V_1 = C_2V_2$ » 16.29 ×V_1 = 0.2 ×20 » V_1 = 0.24ml for 0.2M concentration solution

$C_1V_1 = C_2V_2$

V_1 = 0.06ml of MEA for 0.05M concentration of solution

Then, the solutions were stirred at 60ºC for two hours until a clear homogeneous solution is obtained.

3.3 Thermogravimetric analysis:

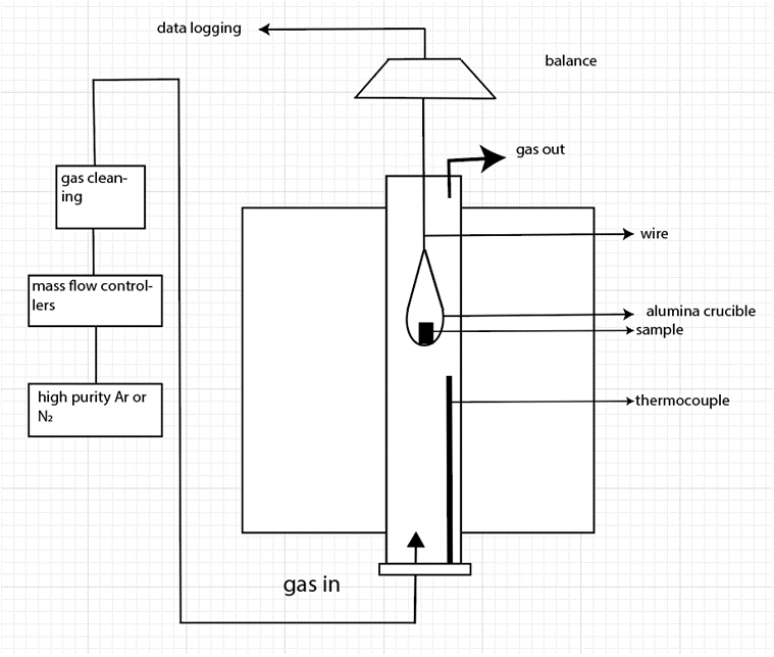

Figure 3.1: Schematics of Thermogravimetric Analysis

Thermogravimetric analysis (TGA) is a thermal analysis method in which a sample's mass is measured over time for a range of temperatures. TGA measurement gives a perspective about

the physical phenomena, such as transition, adsorption, desorption, and absorption. It can elucidate the chemical phenomena, including chemisorption and thermal decomposition. The measured weight reduction curve gives information on:

a) Alterations in sample composition

b) Thermal stability

c) Kinetic parameters for chemical reactions in the sample

A derivative of the weight loss curve can be used to show the point at which the loss is most apparent. TGA of the ZTO solution was performed to elucidate the thermal decomposition of metal precursors used in making the sol-gel. Thermogravimetric analysis (TGA) was performed using Shimadzu-50H with a 20 µL alumina crucible. Approximately 10 mg of sample was heated from room temperature to 800^{o}C at a heating rate of 20^{o}C/min under 20 mL/min of nitrogen. Figure 3.1 shows the schematic diagram of the TGA process involved in this dissertation.

3.4 Spin Coating Process:

Spin coating is a procedure employed to deposit uniform thin films that use the centrifugal force generated by the rotating substrate at a certain speed along with the surface tension of the solution across the surface of the substrate. Rotation is continued for 30 seconds with the fluid being spun off the edges of the substrate till the desired film thickness is achieved. The solvent used in the process is usually volatile, providing for its simultaneous evaporation. The spin coating process's simplicity lies in its instrumentation, which makes it easy to integrate into the process.

Also, one of many advantages of the spin coating process is its capability to deposit thin films onto substrates of different sizes and orders ranging from a few mm to larger flat panel

displays. The spin coating process is highly likely to achieve a uniform and consistent film with high spin speeds in another main advantage. However, low throughput because of single deposition compared to batch deposition and chemical waste with only 10% of the chemical used. In contrast, others are just flung off because of the disadvantages of the spin coating process. The spin coating involves three steps mechanisms, as shown in figure

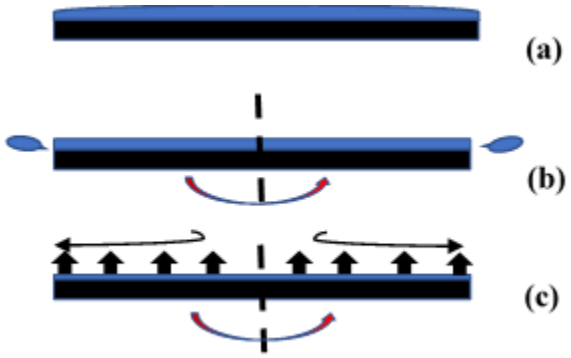

Figure 3.2: Schematic diagram of the vital steps of thin film deposition using a spin coating process. (a) sol-gel solution poured onto the substrate, (b) substrate spinning at high-speed flinging off the excess solution to the sides, (c) airflow drying

The deposited film's thickness depends on the spinner's speed (spin coater), the viscosity of the solution, vapor pressure, temperature, and local humidity. The film thickness of the spin-coated thin film can be obtained as follows [10];

$$t = k\frac{p^2}{\sqrt{\omega}} \sim \frac{\vartheta^{0.4}}{\omega^{0.2}} \qquad 3.1$$

where k is spinner constant, ω is the spin speed in rpm, and ϑ is the viscosity of the solution, p is the percentage of solids in the solution. It is a general practice to determine the required conditions empirically to achieve the desired thickness for a film.

3.4.1 Sol-gel Thermal Evolution:

The development of the gel layer into the oxide film is a multiple-step procedure that involves the formation of metastable intermediates, pyrolysis, and the decomposition of the organic parts, followed by the initiation of development of a network of metal oxide crystallites by nucleation and growth mechanisms. It also involves releasing residual outwards. Initially, this process occurs during the drying and intermediate heat treatment performed between each layer deposition. The whole process occurs during the final heat treatment within all the layers in a collective manner. The extent to which the transformation occurs during the initial heating process plays a vital role in the crystallization behavior and the microstructure of the final film.

3.5 ZTO thin film deposition:

Oxidized Si wafers with 100nm dry oxidized SiO_2 and highly p (Boron) doped Silicon substrate with <100> orientation and 0.001-0.005 Ω. cm resistivity purchased from University wafers, Inc. First, Si wafer is cleaned ultrasonically using Acetone, Methanol, and DI water to remove any impurities in the wafer itself. It was then attached to the spin coater onto its spinning head with double tape. It was made sure that the Si wafer is well centered and leveled. ZTO solution was dropped onto the oxidized wafer after filtering it through a 0.22μm syringe membrane to spin coat a thin film of ZTO. It was then spun 30 secs at a speed of 3000 rpm four times and calcined at 285ºC after each spin coat. The final heat treatment was done in the box furnace in the air at 500ºC for 1 hour to obtain the film's desired thickness as measured using a profilometer.

3.6 Cleaning:

Wafers surfaces are vulnerable to contamination during the storage and device fabrication process because of chemicals, gases, humidity, water vapor, and human errors. The contaminants

get absorbed onto the wafer surface and might occupy space in the electrically responsive area, leading to devices' failure. The micro contaminants may cause 50% of yield loss in IC fabrication. Hence, a clean substrate surface has been recognized as the vital component in semiconductor microelectronic devices' fabrication process. Thus, it is crucial to remove the native oxides, organic contaminants, metallic impurities, adsorbed molecules, and the residual species before proceeding to the final steps [11], [12].

Metal contacts, electrical and optical properties might be affected by native oxides that can grow easily on the exposed surfaces. Molecular compounds such as organic contaminants from photoresist, solvent residues, metal oxides or hydroxides, atomic species introduced by equipment and ionic materials such as Sodium (Na^+) ions, Fluorine (Fl^+), Chlorine (Cl^+) ions that are absorbed during the processing, are the three main species of contaminants can alter the device characteristics of a semiconductor [13]. Wet and dry etching is usually used for surface cleaning. Compared between the two, wet etching is favored more because of its superiority over dry etching, as dry etching might sometimes damage the surface and create electrically inept devices [14]. The following paragraph describes the cleaning procedure involve in cleaning the ZTO surface.

The ZTO deposited Si wafer was diced into 1×1 cm pieces. It was first cleaned ultrasonically with acetone for 5 minutes to completely de-grease the organic contaminants. It was then put on a methanol bath to dissolve residues from acetone and to further clean the sample. Finally, the samples were rinsed with de-ionized (DI) water to remove any remaining residues from acetone and methanol, followed by drying of the samples blowing house nitrogen.

3.7 Device Fabrication

Semiconductor device fabrication to fabricate IC requires several physical and chemical processes, including ion implantation, diffusion, oxidation, photolithography, thin film deposition, etching. Photolithography is one of the major and most fundamental steps in any semiconductor device processing. The paragraph or section below describes the process and technology involved in photolithography.

3.7.1 Photolithography

Photolithography derives its meaning from the Greek word *lithos*, meaning stones and *graphia*, meaning to write, literally mean writing on stones. Photolithography, also referred to as optical or UV lithography, uses light to transfer a pattern onto the substrate. In other words, optical lithography is a photographic process by which a light-sensitive polymer, called a photoresist (PR), is exposed and developed to form 3-D relief images on the substrate [15].

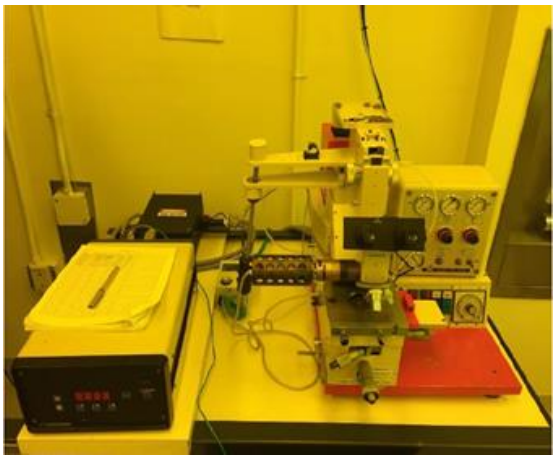

Figure 3.3: Karl Suss MJB3 photo-mask aligner

However, this process has its limitation since the minimum feature sizes to be in the realm of a few microns, and hence in the modern device fabrication process, e-beam photolithography is used to obtain the smaller feature sizes in the nanometer scale. Since the maximum spectral sensitivity

of the PR employed in this process lies in the near UV or blue portion of the spectrum (320-460nm), a yellow light ambient is used as ambient lighting to block photons with wavelengths smaller than 500nm as shown in figure 3.3.

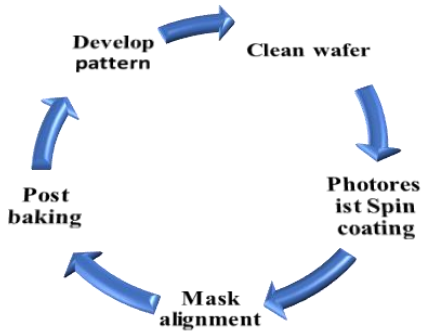

Figure 3.4: The typical order of the Photolithography process

For research presented in this dissertation, the sensitivity of the Photolithography was enough with the required minimum dimensions. The typical photolithography process involves multiple steps, as shown in the chart in Figure 3.3, to produce a device pattern on a clean substrate.

The optical lithography's fundamental limit is determined by the optical system alone and by the overall contribution from the optics, resist, developing, and etching process. The photoresist performance factor mainly depends upon:

- Resolution
- Adhesion
- Process latitude
- Exposure rate, sensitivity, and exposure source
- Pinholes

- Particle and contamination levels
- Step coverage
- Thermal flow

Also, the minimum feature size depends upon the radiation wavelength. The shorter the wavelength, higher the resolution. The numerical aperture (NA) of the lens used is a key aspect in determining the feature size in photolithography given by

$$NA = n\sin\theta \tag{3.2}$$

where θ is the largest angle incident on the wafer. The relationship between the numerical aperture, light source wavelength and the feature size for optical lithography systems is given by

$$R\ (resolution) = \frac{k\lambda}{NA} \tag{3.3}$$

where, R is the resolution or the feature size, k is the proportionality constant and is determined by several factors including the resist's intrinsic parameters, existence of antireflective coatings above or below the PR, and the coherence of the illumination. λ is the light source wavelength. From equation 3.2, it is seen as NA increases, the resolution (R) decreases, decreasing the feature size.

The following photolithographic steps were used.

First, a diced sample after cleaning was attached to a three-inch Si wafer, and they were placed in a vacuum chuck of a spin coater. Then, the sample wafer assembly is coated with image reversal Photo Resist (AZ-5214eIR) capable of both positive and negative tone modes. The photoresist is coated by spin coating at 4000 rpm for 30 secs and baked. The post-application bake was carried out at 110ºC for one minute, which helps driving off the excess solvent in the resist

layer. Additional processes will make PR less viscous and hence becomes less vulnerable to particle contamination. The rough thickness of the spin-coated PR was about 1.4µm as measured with a profilometer. The thickness of the coating depends upon the speed of the spinner, the viscosity of the PR, humidity, and the topography of the substrate, as given by equation 3.1.

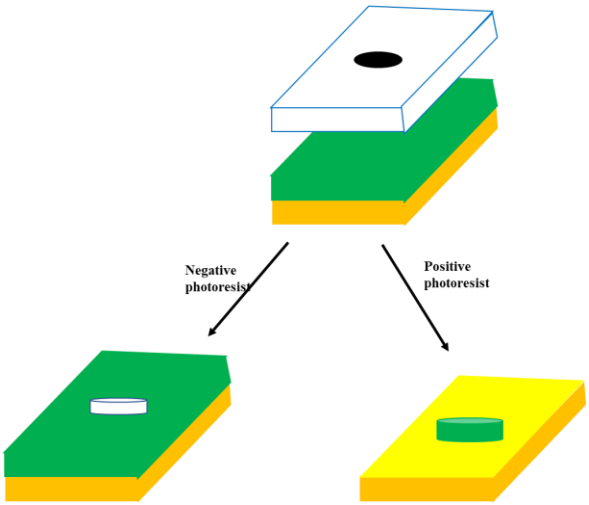

Figure 3.5: Illustration of the pattern transfer mechanism for negative and positive PR

Two types of PR are available. Positive PR (for example-5214e-IR) and negative PR (for example, AZ-nLOF 2070) are the two types of PR that are used in this research. The positive PR becomes more soluble when exposed to UV light, and negative PR would harden with UV exposure because of the cross-linking between the polymers. The selection of the type of PR depends upon what kind of photomask is used to transfer the pattern. Figure 3.4 depicts the pattern transfer mechanisms for both positive and negative PR.

After the post-application bake, the PR coated sample was mounted on the sample holder of the Karl Suss MJB3 photo-mask aligner equipped with a 160W mercury lamp, as shown in figure 3.2. A self-patterned plastic photomask was mounted above the sample. The sample and the patterns of the photomask were aligned using the optical microscope attached to the mask aligner. Then it was exposed to the radiation of the Hg lamp at a power of 160W for 30 secs. A

clear field mask with the soft contact illumination mode was used in all the device fabrication processes. A clear field photomask has an opaque pattern on a transparent background, while a dark field photomask has a transparent pattern on an opaque background. AZ-5214e photoresist has the capability of image reversal (IR).

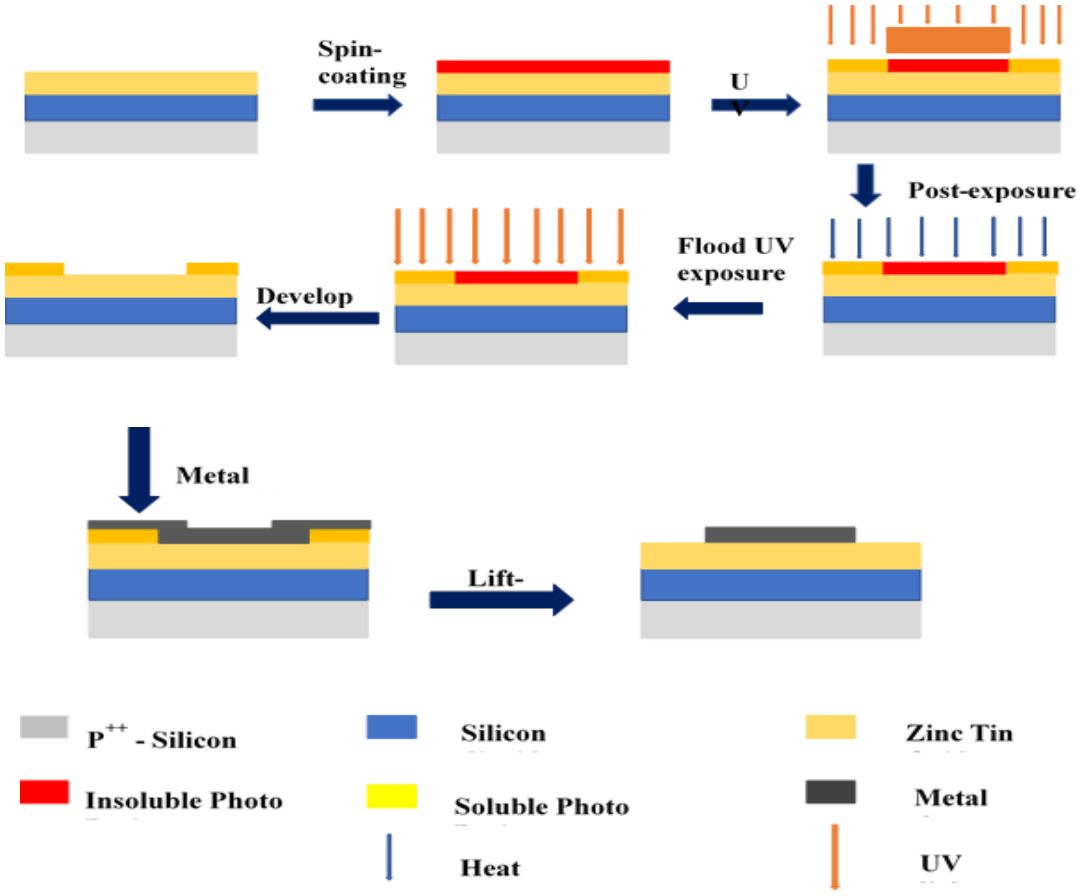

Figure 3.6: Flow diagram of the reverse Photolithography process

After UV exposure, the samples were hard baked at 110ºC for 60 secs, after which the exposed area of the PR crosslinks and becomes insoluble in developer. However, the unexposed area remains photoactive. Then, a direct re-exposure of UV with no mask, also known as flood exposure, for 60secs to the post-baked samples was performed, which made the areas harden where a higher dose of UV absorbed results in image reversal [16].

The samples were then developed in AZ 726MIF to dissolve the soluble area of the photoresist film, which resulted in a negative image of the mask pattern on the substrate. The chemicals used as developers for common PRs are, in general, aqueous-based such as KOH or tetramethylammonium hydroxide (TMAH) for metal ion free developers. The shape of the PR profile and the linewidth control is determined by the developer's reaction and the resist. Out of all other methods, in this research, the puddle development method in which the substrate is spun to spread the developer efficiently was used to develop the pattern. When the developing time elapsed, the additional developer was rinsed with DI water. It is essential to employ the rinsing immediately after development to avoid over-developed patterns.

3.7.2 Metal Contact Deposition: Direct Current (DC) Magnetron Sputtering

Sputtering is a physical vapor deposition (PVD) technique that is used to deposit films of the target source onto the substrate. It involves the removal of material from the target (usually called a cathode) by bombarding energetic ions from the plasma, and the ejected material transports to the surface of the sample to be deposited [17].

In a DC sputtering system, plasma is created by the application of DC voltage between the two electrodes, the cathode, and the anode. An inert gas such as Argon (Ar) is used as the regular feed gas to generate plasma. Positively charged ions (Ar^+) of the inert gas (Ar) are attracted and are accelerated towards the target that is in a negative potential with respect to the plasma. Sputtering is usually conducted either in a vacuum or at a very low pressure to prevent a gas-phase collision in the space between the target and surface. Magnetron configuration with a magnet placed beneath the target with the magnetic field being parallel to the target surface increases the intensity of the plasma by enhancing energetic electron density near the target, which enables a

DC magnetron sputtering system a higher yield or sputtering rate process compared to ordinary parallel electrode DC sputtering.

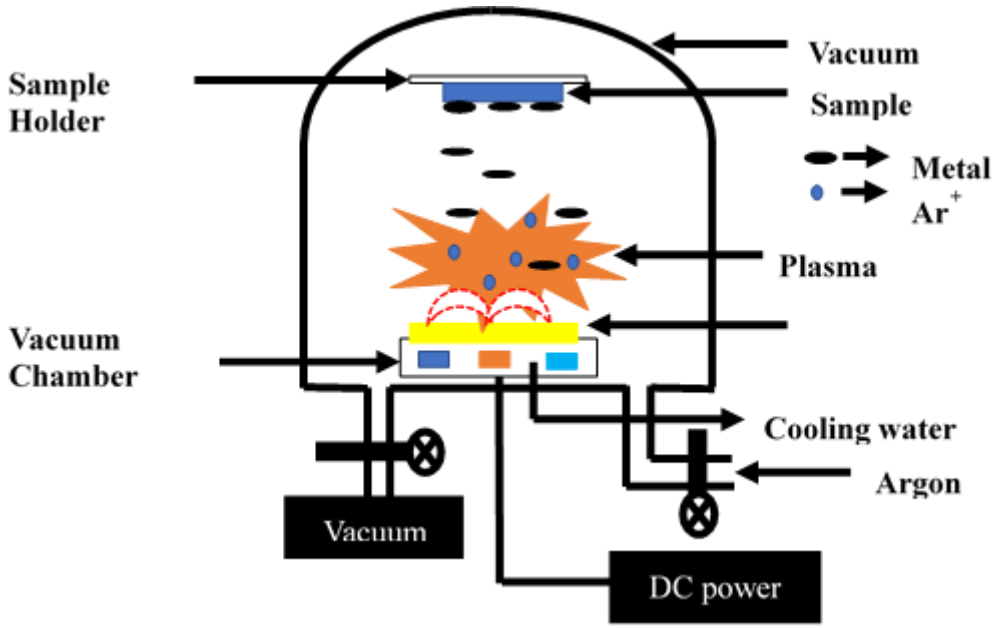

Figure 3.7: Schematic diagram of the DC magnetron sputtering system.

Depending upon the nature of supplied power source, two types of magnetrons sputtering systems are available. a) DC sputtering and b) RF sputtering. DC power is usually preferred for electrically conductive target materials, and it is effective and economical. The deposition rate is high as compared to RF sputtering. In RF sputtering, the source of power is AC. The power supply is a high voltage RF source often fixed at 13.56MHz. RF sputtering has a wide range of applications and is suitable for all the materials (conductive and non-conductive materials) but is generally used for depositing dielectric sputtering target materials. The schematics of the DC magnetron sputtering system used in this research are shown in figure 3.5.

Figure 3.8: The dc magnetron sputtering system used for the metal deposition

For the device fabrication purpose in this research, metal contact deposition was carried out by DC magnetron sputtering with a maximum attainable power of 1000W. The system consists of a vacuum chamber that could attain a high vacuum of 3×10^{-7} Torr was coupled with a roughing pump and turbopump. The chamber is comprised of four 2" diameter magnetron sputtering guns. Chimneys are placed on each gun to facilitate the deposition on the targeted substrate which in turn would prevent the ejected material from the wide-spreading and cross-contamination.

The sample holder plate is located right above the sputter target in approximately 15cm which can be mechanically rotated once the vacuum chamber is closed to facilitate the deposition of four different metals on the same or several other samples simultaneously without venting the vacuum. The photolithographically patterned samples were mounted on the sample holder plate. The vacuum chamber was vented with the pumping assembly until it reaches about 10^{-7} Torr. Argon gas was introduced into the chamber at the rate of 95sccm (standard cubic centimeter per

minute), and the pressure of the chamber was maintained at 18 mTorr. The required DC voltage was applied between the target and the ground at a fixed current to initiate the plasma.

Table 3.2: A summary of the parameters to be fixed for each metal deposition

Metal	Voltage (V)	Current (A)	Pre-sputter time (s)	Sputter time (s)	Film thickness (nm)
Pd	380	0.25	40	120	140
Ti	290	0.25	180	360	100
Ir	490	0.25	60	20	15
Ni93% V7%	340	0.25	120	240	40

Pre-sputtering was performed for few minutes to remove any impurities on the surface of the target before depositing the metal on the samples. Finally, the desired metals were deposited on the samples. Chilled water lines were maintained under the targets to maintain the temperature during the deposition process. The picture of the DC magnetron sputtering system located at the Leach Science Center of Auburn University is shown in figure 3.8.

3.7.3 Lift off

Lift-off is a step in the semiconductor device processing which allows to wipe off the excess metal deposited on the substrate. In this process, the metal deposited is washed away by stripping the photoresist underneath. By dissolving the resist to the suitable solvent. For the research work presented in this dissertation work, wet chemical lift-off was performed with

acetone followed by ringing in methanol and DI water to dissolve photoresist and lift off the excess metal to pattern metal contacts on the substrate.

Generally, the lift-off duration depends upon the quality of the deposited film, type of photoresist, prebake/post-bake time, film deposition temperature, UV exposure dose, and developer solvent. Image reversal photolithography used in this research made the lift-off process easier by creating an undercut profile with a negative slope. Fig 3.6 shows the schematics of the process flow of the ZTO device fabrication.

3.8 Ohmic Contacts:

Ohmic contact is defined as a contact between the metal and semiconductor surface when there is a negligible barrier between the Fermi level and the conduction band of the semiconductor so that is no restriction of two-way flow of charge carriers across the junction. Ideal ohmic contact shows a linear relationship between the output current and the applied voltage (Ohm's law) with a low contact resistance R_c. The contact resistance (R_c) of a metal-semiconductor junction for a highly doped semiconductor is given by [18];

$$R_C = \exp\left[\frac{2\sqrt{\varepsilon_S m^*}}{h}\left(\frac{\varphi_b}{\sqrt{N_D}}\right)\right] \quad 3.4$$

where ε_S is the permittivity of the semiconductor, $m*$ is the effective mass of an electron, h is the Planck's constant, φb is the barrier height and N_D is the doping concentration. A low contact resistance compared to the bulk resistance is required to obtain a low voltage drop across the metal-semiconductor to reduce power dissipation during the current conduction.

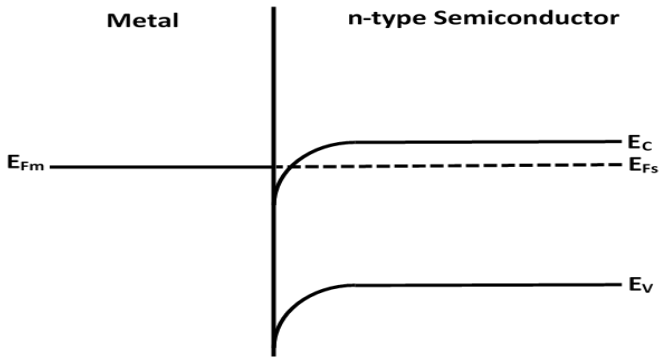

Figure 3.9: Energy band diagram of ohmic contact on an n-type semiconductor

A semiconductor with a higher doping concentration and a metal-semiconductor contact with lower barrier potential can enhance a low contact resistance. Good control in surface parameters that affect the Schottky barrier height dictates the Schottky or Ohmic nature of the contact. If the work function of the metal (φ_m) is lower than the work function of the semiconductor (φ_s), an ohmic contact can be realized for n-type semiconductors, as shown in figure 3.3.1. The combination of the proximity of the Fermi level to the conduction band and the band bending at the interface allows the low contact resistance, Linear *I-V* characteristic proportional to the contact area, which is a result of low work function of the metal than the semiconductor and the fermi level pinning caused by electronic states at the MS interface and the doping level in the semiconductor. Some of these parameters usually affect the Schottky barrier height. A thinner depletion region helps the carriers be tunneled through the barrier, contributing to the ohmic contact's improvement. Barrier height can also be lowered by choosing a metal that has a work function lower than that of ZTO and with contact metal annealing. Contact metal annealing in this research has been performed by RTA in N_2 at 500ºC for 2 mins.

3.9 Experimental Procedure:

In this section, different material characterization techniques used for the characterization of Zinc Tin Oxide thin film and their principles are discussed. Before device fabrication, the film was characterized using Atomic Force Microscopy (AFM), Scanning Electron Microscopy (SEM), X-Ray Diffraction (XRD), X-Ray Photoelectron Spectroscopy (XPS), and Photoluminescence (PL) spectroscopy.

3.9.1 Atomic Force Microscopy (AFM)

AFM is possibly the most versatile and powerful microscopy techniques to study the samples at the nanoscale. It is a technique that allows high-resolution imaging of surfaces with atomic layer depth resolution to obtain topographical information. AFM, along with surface roughness, also gives information on friction, thickness, dislocations, capacitance, and homogeneity of the scanned surface. AFM principle mainly can be categorized into three different parts. They are:

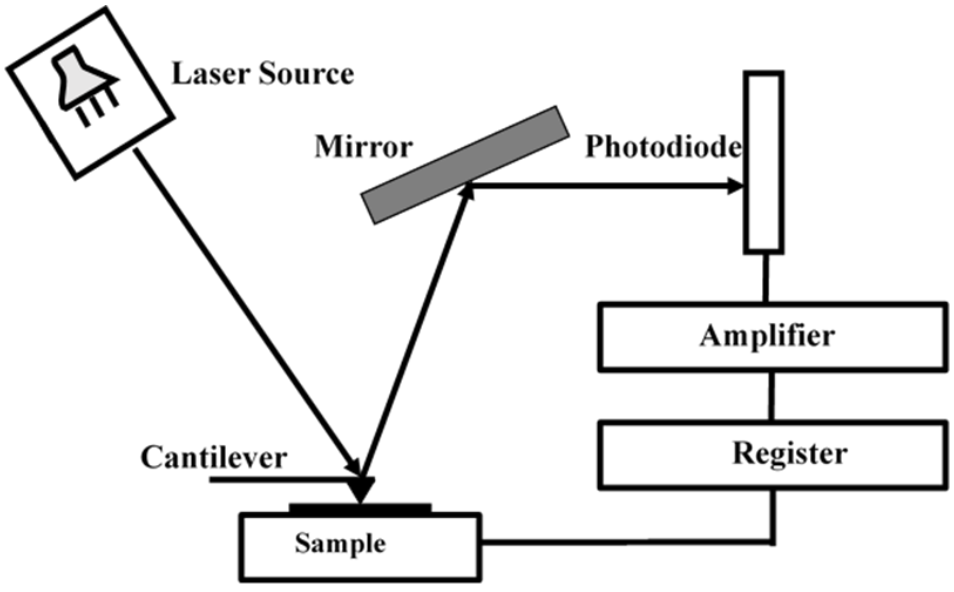

Figure 3.10: Schematics of Atomic Force Microscopy

Surface sensing: AFM utilizes a cantilever with a very sharp tip that is used to scan a sample region. The attractive close-range force between the surface and the tip causes the cantilever to travel toward or deflect away from the surface as the tip reaches the surface. But as it is brought nearer to the surface, there is an increased amount of repulsive force, causing the cantilever to deflect from the surface.

a) Detection method: A laser beam is used to identify cantilever deflections towards or away from the area of interest. Upon the reflection of an incident laser beam off the cantilever, deviations may vary in the direction of the reflected beam. A position-sensitive photodiode (PSPD) is used to record these changes. Hence, if an AFM scans over a raised surface, the resulting cantilever deflection and the consequent change in the direction of the reflected beam are recorded by the PSPD[20].

b) Imaging: AFM produces the images of the scanned samples by scanning the cantilever over an area of interest. The raised and lowered features on the sample surface triggers the deflection of the cantilever monitored by PSPD. With the use of a feedback loop used to control the height of the tip above the surface, constant laser position is maintained, and AFM generates an exact topographic map of the surface features. Based on the interaction of the tip and the sample surface, AFM is mainly categorized as non-contact mode (attractive), contact mode (repulsive), and tapping or intermittent mode [21]. In this research work, Park System's non-contact AFM has been used.

3.9.2 X-Ray Photoelectron Spectroscopy:

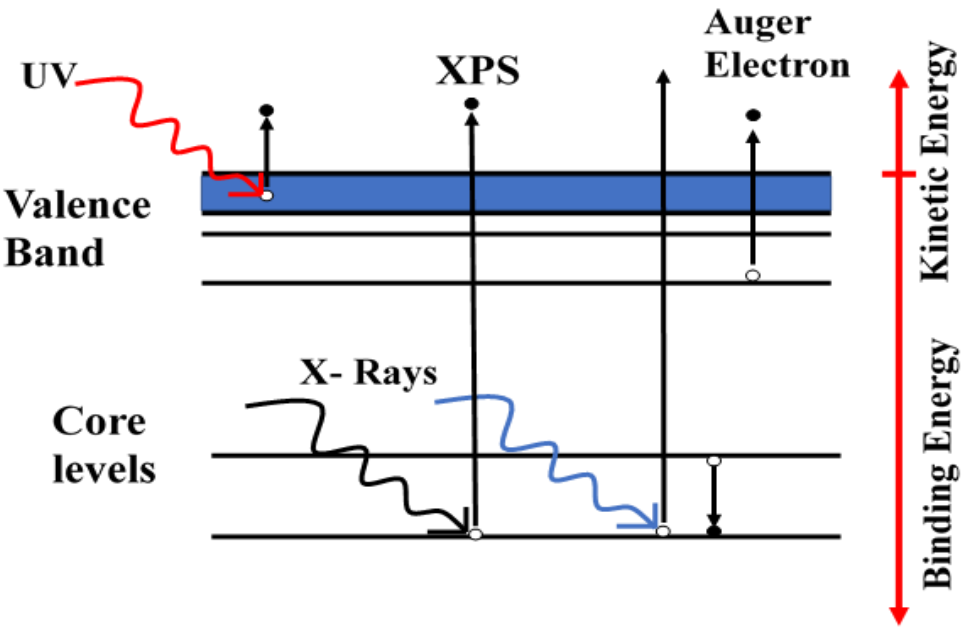

Figure 3.11: Photoelectron emission due to incident photon interaction with the sample

X-ray Photoelectron (XPS), also known as Electron Spectroscopy for Chemical Analysis (ESCA), is a surface analysis technique that is based on Einstein's theory of photoelectric effect. According to the photoelectric effect, when light is incident on a sample, an electron can absorb a photon and escape from the material with maximum kinetic energy given by:

$$K.E. = h\nu - E_B - e\phi \qquad 3.4$$

where v is the frequency of the incident photon, h is the Planck's constant, E_B is the binding energy of the electron, and ϕ is the metal's work function. A threshold frequency below which light, regardless of intensity, fails to eject electrons from a metallic surface.

$$h\nu > eF_m \qquad 3.5$$

In XPS, the Kinetic Energy (K.E.) distribution of the emitted photoelectrons can be measured using an appropriate electron energy analyzer, and a photoelectron spectrum can hence

be recorded. With the use of photoionization and energy dispersive analysis of the emitted photoelectrons, the composition, and the electronic state of the surface of a sample can be investigated. Traditionally, photoelectron spectroscopy can be categorized into three main divisions according to the source of exciting radiation:

- X-ray Photoelectron Spectroscopy (XPS or ESCA) - using soft x-ray (200 - 1500 eV) radiation to examine core-levels.

- Ultraviolet Photoelectron Spectroscopy (UPS) - using vacuum UV (10 - 45 eV) radiation to examine valence levels.

- Auger Electron Spectroscopy (AES or SAM) – using energetic electron (1000 – 10,000 eV) to examine core-levels.

Besides identifying elements in the sample or specimen, the intensity of the peaks can be used to quantify how much of each element is in the sample. Each peak area is proportional to the number of atoms present in each element. The specimen chemical composition is obtained by calculating the respective contribution of each peak area. The average probing depth for an XPS system is approximately 10nm [22]. Illustration of the mechanism of knocking off the electrons when short-wavelength X-rays are incident on a surface is shown in figure 3.13.

For this research, a load-locked Kratos XSAM, 800 surface analysis system, equipped with a hemispherical energy analyzer. A water-cooled, non-monochromatic dual anode x-ray gun equipped with an Al window was used to excite the photoelectrons. MgKα of energy 1253.6 eV was used as radiation. Dr. Bozack and Dr. Comes' graduate students Suresh and Rajendra performed XPS for the research presented in this dissertation. The results and analysis of XPS spectra obtained are presented in chapters 1, 6, and 7.

3.9.3 X-Ray Diffraction (XRD):

For electromagnetic radiation (em) to be diffracted, the spacing in the diffraction grating should be of the same order as the wavelength. Generally, in crystals, the interatomic spacing is around 2.3A^{o}. Hence, the suitable radiation for the study of the crystal structure is X- rays.

Figure 3.12: Picture of Bruker D2 Picture of Bruker D2 Phaser XRD system in Geosciences, Auburn University.

Crystallographic information of a specimen, such as thickness, alloy composition, strain state of different layers, and dislocation density, can be obtained with the help of X-ray Diffraction (XRD). The diffraction of an X-ray beam on a crystal can be simplified to the diffraction of an X-ray beam at the lattice planes of a crystal. A beam of X- rays directed at a crystal interacts with the electrons of the atoms in the crystal and oscillate under the influence of the incoming X-rays and becomes a secondary source of em radiation. In this process, a monochromatic beam of X-ray hits an ordered lattice with the distance d between the lattice planes with an angle θ as shown in Figure 3.14. When Bragg's law is satisfied the atomic planes of a crystal scatters the incident beam of x-rays to constructively interfere as they leave the crystal at an angle θ, which is referred to as x-ray diffraction. Constructive interference can only be detected if the wavelength λ of the x-ray multiplied by an integer n equals interplanar spacing d times sinθ where n is the order of diffraction.

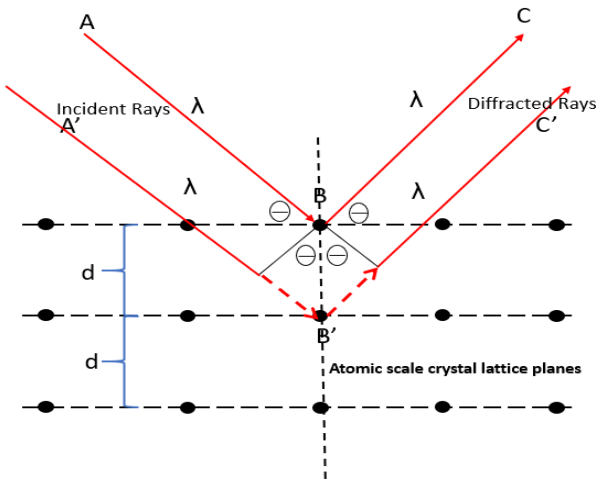

Figure 3.13: Bragg's law of reflection. The diffracted X-rays shows constructive interference when the distance between paths ABC and A'B'C' differs by an integer of wavelength λ

X- rays are produced whenever high-speed electrons are ejected from a heated filament and accelerated towards a target by applying a voltage and bombarding the target material with these electrons. When the electrons have enough energy to dislodge the inner shell electrons of the target material, characteristic X-ray spectra are produced, consisting of many components, the most common being K_α and K_β. K alpha consists, in part, of $K_{\alpha 1}$ and $K_{\alpha 2}$.

This is caused by the fact that the L-shell has four subshells from which the electrons fall in the K-shell. $K\alpha_1$ has a slightly shorter wavelength but twice the intensity of $K\alpha_2$. A filter is used to get the monochromatic convergent K alpha X-ray beam. Copper (Cu), Aluminum (Al), Molybdenum (Mo), and Magnesium (Mg) are the commonly used metal targets [23]. Table 3.3 shows the list of characteristics values for different targets of X-ray tubes [24].

Table 3.3: List of characteristics values for different targets of X-ray tubes

Anode material	Atomic number	Wavelength K-alpha $_{1,2}$ nm	Energy K-alpha$_{1,2}$	Critical excitation keV voltage	Optimum KV setting
Cu	29	0.1542	8.04	8.98	30-45
Co	27	0.1791	6.92	6.871	25-40
Fe	26	0.1937	6.40	7.11	20-35
Cr	24	0.2291	5.4	5.99	20-30
Mo	42	0.0561	17.77	20.00	60

The interplanar spacing d for all the layers within the penetration depth can be calculated after sweeping the incident x-ray and detection angles and identifying intensity peaks representing the constructive interference with the use of fitting software as

$$d = \frac{a}{\sqrt{h^2+k^2+l^2}} \tag{3.6}$$

where a is the lattice constant for the cubic structure. h, k and l are the miller indices. For hexagonal structures,

$$\frac{1}{d^2} = \frac{4}{3}\left(\frac{h^2+hk+k^2}{a^2}\right) + \frac{l^2}{c^2} \tag{3.7}$$

where a and c are the lattice constant of the hexagonal unit cell.

For the research purpose presented in this dissertation, we used Proto- AXRD Θ-Θ diffractometer with an X-Ray Kα line with a Cu target with 40kV at 30mA to probe the ZTO films.

3.9.4 Photoluminescence (PL) Spectroscopy:

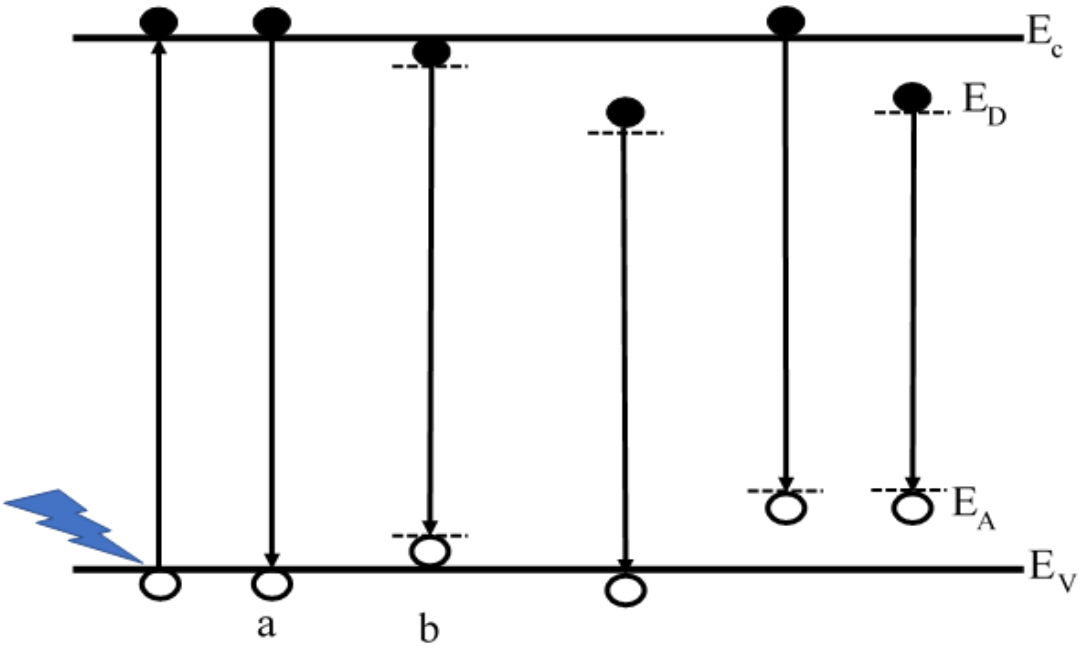

Figure 3.14: Radiative recombination of e-h pair in PL process

Photoluminescence is one of the non-destructive techniques to study the electronic properties of semiconductor film. Generally, PL is a type of luminescence generated by photoexcitation. The incident light from a light source (here laser) may alter the electronic state of a molecule, which in turn relaxes to a final state *via* one or several relaxation mechanisms. In other words, PL is an optical process in which light is emitted from a sample because of the absorption of the incident light, which is often referred to as photoexcitation. In PL, the material is exposed to monochromatic light, and a spectrometer collects re-emitted photons with varying wavelengths. Since PL relies on the electronic transition in the sample, enough photon energy higher than that

of the bandgap ($E>E_g$) is required to excite the electrons from the valence band into the conduction band. PL usually spans the wavelength in the UV, visible, and IR range.

When the incident photon with E>Eg gets absorbed, electron-hole pairs are created with the incident light, which then returns to a lower energy state by the emission of photons by losing some of its energy (relaxation) and then recombine. With the help of analytic data of photoluminescence spectra, kind of impurities, bandgap, and activation energy of the in-gap states (defects) can be extracted. Also, the composition of the compound can also be estimated from the peak intensity of the PL spectra. As PL is a radiative transition technique, radiative recombination occurs at defect sites in the crystal which helps to reveal the details concerning defect composition and concentration.

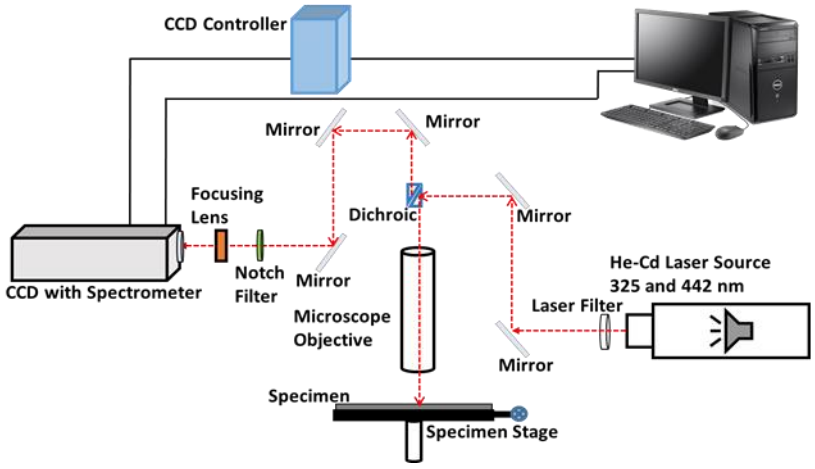

Figure 3.15: Schematics for Raman and PL spectroscopy used in this research

Optical processes in semiconductors can be divided into two types: Radiative and Non-radiative transitions.

1. Radiative Transition: When an electron drops from a higher excited state to lower energy, a radiative transition occurs regardless of intrinsic state or energy state formed by impurities. Hence, the system is imbalanced, and e-h pairs are generated. To explain this

process, some basic transitions need to be considered:

(I) Band to Band transition

Band to band transition in the relationship between the free electrons and holes. These types of transitions usually occur in direct bandgap materials such as II-VI and III-V compounds, where the e-h pairs will generate radiative recombination between the conduction and valence band.

(II) Free exciton transition

For an intrinsic material, an electron and a hole will attract each other to form an exciton. The energy of free exciton can be expressed as

$$E_n = \frac{2\pi^2 m^* e^4}{h^2 \epsilon^2 n^2} \qquad 3.6$$

where m* is the effective mass, h is the Planck's constant, ∈ is the dielectric constant, and is the principal quantum number. The bottom of the conduction band is considered as the zero-energy level. The free excitons only would emit light if they are at the quantum energy states permitted by equation 3.6. It is because of the existence of excitons, the transition energy in bandgap can be expressed as

$$h\nu = Eg - En \qquad 3.7$$

where Eg is the bandgap energy, and En is the excitonic binding energy.

III. Free to bound transition:

This type of transition occurs between energy bands of materials and the impurity levels such as from conduction band to acceptor of from donor to the valence band. For donor type impurity following transitions can occur,

a. Electron reaching ionization donor energy level (for an infrared range of spectrum)

b. Hole reaching neutral acceptor energy level for near band edge (NBE)

IV. Donor-acceptor pair recombination.

A free electron at the donor level can recombine with a hole in the acceptor level to complete this transition. The radiative energy of these transitions is given by

$$E_{DA} = h\nu = E_g - (E_d - E_A) + \frac{q^2}{\epsilon K_s r} \quad 3.8$$

where h is the Planck's constant, ν is the frequency, E_D and E_A are donor and acceptor bound energy respectively, ε is the dielectric constant, and r is the distance between the donor and acceptor. r is inversely proportional to the probability of transition.

2. Nonradiative transitions:

Nonradiative transitions don't involve light. The excess energy from the excited level is then dissipated in some other way, in most cases in the form of phonons. These phonons are associated with the lattice vibration of solids. These transitions ultimately degrade the absorbed energy to heat. Non-radiative transitions display or manifest themselves in suppressed luminescence, the creation of intrinsic defects, enhanced diffusion, reduced carried lifetimes, and so on [25].

For the research in this dissertation, we used PL spectroscopy to examine gamma and proton irradiation's effect on ZTO thin films. Room temperature micro-PL was carried out using a 325nm line (20 mW) of He-Cd laser as an excitation source. For our sample, we could observe a single band for the NBE peak at ~ 3.3eV. The detailed analysis of the observed results is presented in chapter 5 and 6.

3.10 References:

[1] Kim, Y. J., Yang, B. S., Oh, S., Han, S. J., Lee, H. W., Heo, J., ... & Kim, H. J. (2013). Photobias instability of high performance solution processed amorphous zinc tin oxide transistors. *ACS applied materials & interfaces*, *5*(8), 3255-3261.

[2] Seo, S. J., Hwang, Y. H., & Bae, B. S. (2010). Post annealing process for low temperature processed sol–gel zinc tin oxide thin film transistors. *Electrochemical and Solid State Letters*, *13*(10), H357.

[3] Liu, L. C., Chen, J. S., & Jeng, J. S. (2014). Role of oxygen vacancies on the bias illumination stress stability of solution-processed zinc tin oxide thin film transistors. *Applied Physics Letters*, *105*(2), 023509.

[4] Lee, C. G., Dutta, S., & Dodabalapur, A. (2010). Solution-processed ZTO TFTs with recessed gate and low operating voltage. *IEEE electron device letters*, *31*(12), 1410-1412.

[5] Branquinho, R., Salgueiro, D., Santa, A., Kiazadeh, A., Barquinha, P., Pereira, L., ... & Fortunato, E. (2015). Towards environmentally friendly solution-based ZTO/AlOx TFTs. *Semiconductor Science and Technology*, *30*(2), 024007.

[6] Parthiban, S., Elangovan, E., Nayak, P. K., Gonçalves, A., Nunes, D., Pereira, L., ... & Martins, R. (2013). Performances of microcrystalline zinc tin oxide thin-film transistors processed by spray pyrolysis. *Journal of Display Technology*, *9*(10), 825-831.

[7] Bitter, S., Schlupp, P., Bonholzer, M., von Wenckstern, H., & Grundmann, M. (2016). Influence of the cation ratio on optical and electrical properties of amorphous zinc-tin-oxide thin films grown by pulsed laser deposition. *ACS combinatorial science*, *18*(4), 188-194.

[8] Kim, D., Jeong, Y., Song, K., Park, S. K., Cao, G., & Moon, J. (2009). Inkjet-printed zinc tin oxide thin-film transistor. *Langmuir*, *25*(18), 11149-11154.

[9] Young, D. L., Moutinho, H., Yan, Y., & Coutts, T. J. (2002). Growth and characterization of radio frequency magnetron sputter-deposited zinc stannate, Zn 2 SnO 4, thin films. *Journal of applied physics*, *92*(1), 310-319.

[10] Campbell, S. A. (2001). *The science and engineering of microelectronic fabrication*. Oxford university press.

[11] Sanganeria, M. K., Öztürk, M. C., Harris, G., Violette, K. E., Ban, I., Lee, C. A., & Maher, D. M. (1995). Ultrahigh Vacuum Rapid Thermal Chemical Vapor Deposition of Epitaxial Silicon onto (100) Silicon: I. The Influence of Prebake on (Epitaxy/Substrate) Interfacial Oxygen and Carbon Levels. *Journal of the Electrochemical Society*, *142*(11), 3961.

[12] Srinivasan, G. R. (1984). Recent advances in silicon epitaxy and its application to high performance integrated circuits. *Journal of Crystal Growth*, *70*(1-2), 201-217.

[13] Kern, W. (1990). The evolution of silicon wafer cleaning technology. *Journal of the Electrochemical Society*, *137*(6), 1887.

[14] Shul, R., Vawter, G., Willison, C., Bridges, M., Lee, J., Pearton, S., & Abernathy, C. R. (1998). Comparison of plasma etch techniques for III–V nitrides. *Solid-State Electronics*, *42*(12), 2259-2267.

[15] Mack, C. (2008). *Fundamental principles of optical lithography: the science of microfabrication*. John Wiley & Sons.

[16] Koch, C., & Rinke, T. J. (2006). Lithography: Theory and Application of Photoresists, Developers, Solvents and Etchants.

[17] Elshabini, A., Elshabini-Riad, A., Barlow, F. D., & Barlow, F. D. (1998). *Thin film technology handbook*. McGraw Hill Professional.

[18] Sze, S. M., Li, Y., & Ng, K. K. (2021). *Physics of semiconductor devices*. John wiley & sons.

[19] Yapa Bandara, K. (2018). The Reliability of Zinc Oxide Based Thin Film Transistors Under Extreme Conditions.

[20] McClelland, G. M., Erlandsson, R., & Chiang, S. (1987). Atomic force microscopy: General principles and a new implementation. In *Review of Progress in Quantitative Nondestructive Evaluation* (pp. 1307-1314). Springer, Boston, MA.

[21] Morita, S., Giessibl, F. J., Meyer, E., & Wiesendanger, R. (Eds.). (2015). *Noncontact Atomic Force Microscopy: Volume 3*. Springer.

[22] Sherwood, P. M. (2013). Paul van der Heide: X-ray photoelectron spectroscopy: An introduction to principles and practices.

[23] Smith, J. V., & Rivers, M. L. (1995). Synchrotron X-ray microanalysis. In *Microprobe techniques in the Earth sciences* (pp. 163-233). Springer, Boston, MA.

[24] Smith, J. V. (1974). X-ray diffraction techniques. In *Feldspar Minerals* (pp. 179-216). Springer, Berlin, Heidelberg.

[25] Stoneham, A. M. (1981). Non-radiative transitions in semiconductors. *Reports on Progress in Physics*, *44*(12), 1251.

Chapter 4

Enhancement of electrical characteristics of a-ZTO TFTs based on channel layers produced with alternating precursor concentration [1]

(This chapter is the following paper published in ELECTRONICS LETTERS, Vol 54, Issue 22, pp 1298-1300, November 2018)

S. Uprety[1], S. Wang[2], V. Mirkhani[1], K. Yapabandara[1], M. P. Khanal[1], D. Hanggi[1], B. Schoenek[1], S. Dhar[1], M. Hamilton[2], W. Hames[3], M. H. Sk[4], and M. Park[1*]

4.1 Introduction:

Amorphous oxide semiconductors (AOSs) based thin-film transistors (TFTs) are useful in flat panel display applications [2]. Amorphous zinc tin oxide (a-ZTO) is of interest because of its high electron mobility/conductivity and optical transparency. Despite the importance, only a handful of research has been performed on ZTO based TFTs. Jeong *et al.* have fabricated the TFTs with a solution-processed ZTO with different concentrations of Sn, and they have achieved maximum mobility of 1.1 cm^2/V.s [3]. Kim *et al*. has investigated the effect of Zn/Sn composition on the operational stability of ZTO transistors and have found the highest mobility of 3.99 cm^2/Vs [4].

Most of the TFTs fabricated on AOSs with high mobility and on-off current ratios are based on vacuum processes such as pulsed laser deposition and rf magnetron sputtering [5] so fabrication of TFTs with improved electrical characteristics have always been a challenge. The pioneering work by Chen-Sha Li *et al*. [6] resulted in a drastic increase in carrier mobility by optimizing the fabrication conditions for the solution-processed TFTs with low temperature annealed ZnO. They used the precursor solutions with three different concentrations and spun coated on top of each

other. The increase in mobility was attributed mostly to the decrease in the porosity in the films. Also, Hong *et al*. have increased the mobility of the TFTs based on indium-gallium-zinc-oxide (IGZO) with two layers of different concentrations (one lower and other higher) and explained the phenomenon of increasing of mobility based on interface location effect [7].

In this letter, we propose a novel approach to stacking the sol-gel processed channel layers to enhance the electrical characteristics of the TFTs [a]. The novelty of this research resides in the fact that the bottom layer with lower precursor concentration followed by a layer of higher precursor concentration produces a densification effect on the bottom layer, reducing interface states at the SiO_2/ZTO interface, and hence, reducing carrier scattering. This effect clearly explains the observed increase in the field effect mobility in TFTs fabricated with the mixed stacked precursors solutions. By using this approach, we have achieved the mobility of 5.3 cm^2/Vs from the TFTs based on sol-gel processed ZTO layers.

4.2 Experiment:

The sol-gel solution for ZTO thin films was prepared as follows; Zinc acetate dihydrate [$Zn(CH_3COO)_2{\cdot}2H_2O$] and Tin(II) Chloride dihydrate [$SnCl_2{\cdot}2H_2O$] were used as metal precursors and were dissolved in 2-methoxy ethanol. The molar concentration of Zn to Sn was maintained at 7:3. Two different concentrations of the precursor solutions (0.05 M and 0.2 M) were prepared. Dry-oxidized highly-boron-doped Si wafers purchased from University wafers, with 0.001 Ohm.cm resistivity, oxide thickness of 100 nm, and <100> orientation, were used as substrates. The oxide (SiO_2) was used as the gate dielectric layer. The precursor solution was spin-coated and then calcined for 5 minutes at 285°C. The spin-coating process was repeated three additional times with the next desired precursors, to achieve a 4-layered film. Three different types of samples were prepared; The first and second types of ZTO films used 0.05 M and 0.2 M concentration

precursors, respectively (The devices fabricated on these layers will be referred to as 0.05 M and 0.2 M samples, respectively). In the case of the third sample, mixed-stacked ZTO films with alternating precursor solution concentrations (layer stacking sequence: 0.2M/0.05M/0.2M/0.05M/SiO_2/Si) were prepared (The device fabricated on this layer will be referred to as the mixed-stacked sample). After ZTO deposition, the wafer with ZTO films was annealed at 500°C for one hour in the box furnace. Source and drain for TFT were patterned photolithographically. Then, Ti/Ir ohmic contact was deposited by direct-current (DC) magnetron sputtering to form source and drain contacts, forming bottom-gate TFTs.

Device isolation was achieved by forming a mesa structure *via* a BOE etching of the ZTO active layer, resulting in the reduction of the gate leakage current by more than four orders of magnitude. Thermogravimetric analysis (TGA) was performed using Shimadzu-50H. X-ray diffraction (XRD) was performed for these samples using a BURKER D2 phaser X-Ray diffractometer using Cu-Kα radiation The XRD instrument was equipped with a scintillation counter and Lynxeye detector. Transistor current-voltage (I-V) and capacitance-voltage (C-V) characteristics were investigated using Keithley 2400-source meters automated with LabView program.

4.3 Results and Discussion:

Thermogravimetric analysis (TGA) of the prepared solutions was performed to elucidate the formation mechanism of ZTO thin films (not shown here). TGA analysis confirmed the thermal decomposition of the residual organic components stop at 500°C, and hence this temperature was chosen as an annealing temperature.

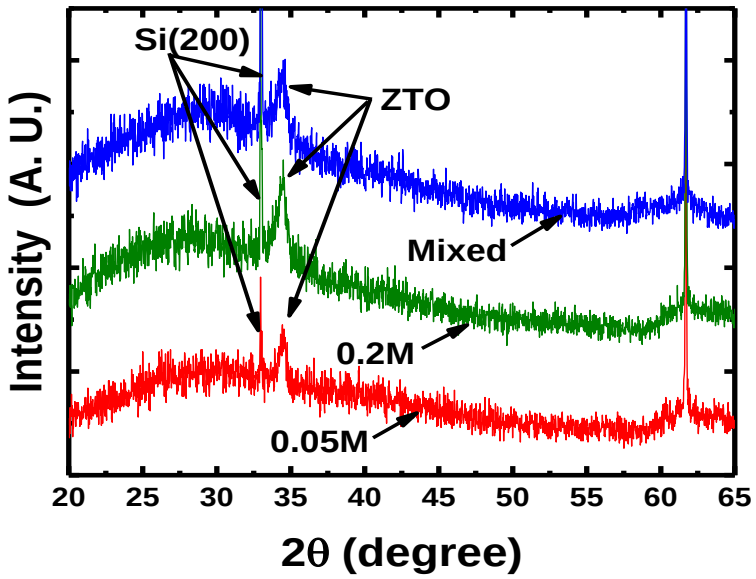

Figure 4.1: X-ray diffraction patterns of the three different films; 0.05M, 0.2M, and mixed stack respectively

Figure 4.1 shows the X-ray diffraction (XRD) pattern for ZTO films and the SiO_2/Si substrate. In all three cases, the relatively broad peak at 2Θ~34° can be seen. According to the JCPDS (number 28-1486), this peak corresponds to the reflection of X-ray from the (311) plane of $ZnSnO_3$, confirming that the films are amorphous ZTO, which is consistent with the literature previously reported[9].

It is possible that the film may also contain the nano/microcrystalline phase since the diffraction peaks were sharper than the ones from the amorphous counterpart. The energy-dispersive spectroscopy (EDX) result (not shown here) confirms that the film is composed of zinc, tin, and oxygen.

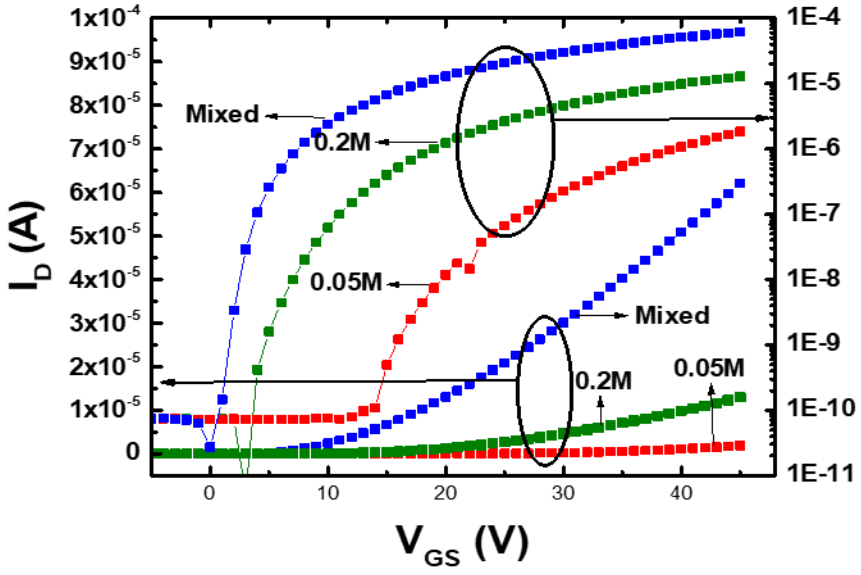

Figure 4.2: Transfer I-V curves for representative TFTs with 0.05 M, 0.2M, and multi-stacked samples.

Figure 2 shows the transfer characteristics of the three types of ZTO TFTs. All TFTs with different precursors have low leakage current (10^{-11} A). The transistor ON current for the mixed-stacked sample was highest while that for the 0.05M sample was the lowest, which implies that the mixed samples offer a better driving capability and thus have a higher ON/OFF ratio.

The turn-on voltage (V_{on}) is defined as the voltage where drain current is 14 V, 4 V, and 1 V for 0.05 M, 0.2 M, and mixed-stacked samples, respectively. The mixed-stacked sample shows the lowest V_{on} and threshold voltage (V_{th}) while the 0.05 M sample has the highest V_{on} and V_{th}. The sub-threshold swing (SS) was extracted at the steepest point of the transfer I-V curves in log scale using the following equation.

$$SS = \left(\frac{d(log(I_d))}{d(V_{GS})}\right)^{-1} \qquad 4.1$$

The *SS* for 0.05 M, 0.2 M, and mixed-stacked samples is 1.49, 1.57, and 0.82 V/decade, respectively. The field-effect mobility was extracted by the following equation.

$$\mu_{FET} = \frac{g_m}{C_i(W/L)V_{DS}} \qquad 4.2$$

where g_m is the transconductance, C_i is the capacitance of the SiO_2, and V_{ds} is the drain voltage that transconductance values were extracted (V_{ds} = 1 V). The *W* is the width, and the *L* is the length of the channel. The plot of field-effect mobility (μ_{FET}) *vs*. gate-source voltage is shown in Figure 3. As can be seen from the plot, the highest mobility was achieved with the mixed-stacked sample. The key electrical characteristics for ZTO thin-film transistors are summarized in Table 1.

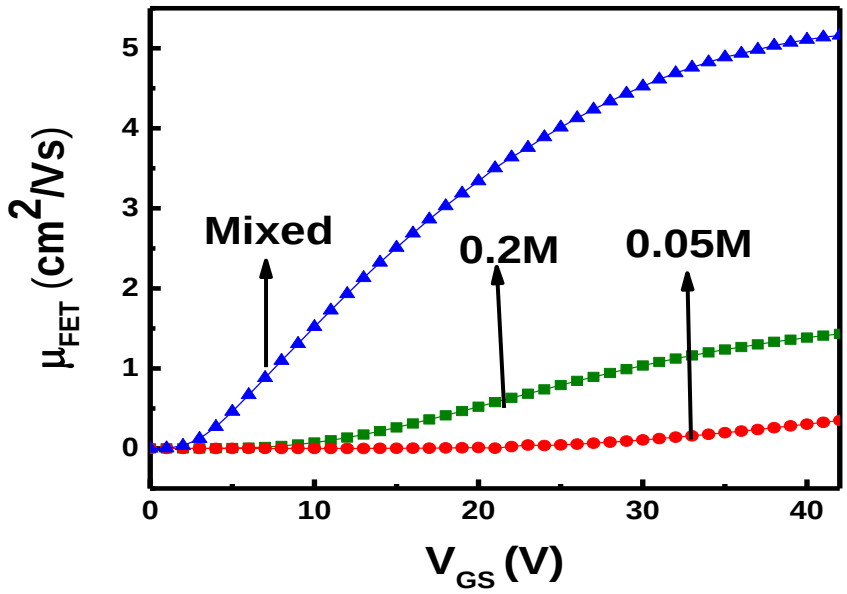

Figure 4.3: Field effect mobility of ZTO TFTs with different precursor solution concentrations

Table 4.1: Summary of the key electrical characteristics for ZTO thin-film transistors

Sample Names	0.05M	0.2M	Mixed-Stacked
Concentration of ZTO solution	0.05M	0.2M	0.05M/0.2M
Number of spin-coated layers	4	4	4a
Thickness of ZTO (nm)	10±3	40±5	25±5
Threshold Voltage V_{th} (V)	30	20	15
Turn-on voltage Von (V)	14	4	1
on/off ratio	10^5	10^6	10^7
μ_{FET} (cm^2/V.s)	0.45	1.45	5.3
SS (V/decade)	1.57	1.49	0.82
D_{it} ($10^{12}/cm^2$)	5.43	5.1	2.82

[a]ZTO (0.2M/0.05M/0.2M/0.05M)/SiO_2/Si

The mixed-stacked sample exhibited the highest mobility (5.3 cm^2/V.s) among the three samples. Also, other parameters such as on/off ratio, *SS*, and interface trap density (D_{it}) were better than the other two [10]. Reduction of threshold voltage was confirmed by calculating the donor concentration from CV measurement using the following equation.

$$N_d = \frac{2}{\frac{d\frac{1}{C^2}}{dV_{gs}}} \times \varepsilon_{ZnO} \times q \qquad 4.3$$

In this calculation, the dielectric constant of ZnO (8.5) was used for simplicity. The donor concentration of the mixed stack film was found to be in the order of 10^{18} cm^{-3} (as compared to 10^{16} cm^{-3} for a 0.2M sample). The negative shift of threshold voltage could be attributed to the

presence of more charge carriers in the mixed-stacked ZTO TFT, which enables the formation of the channel at a lower gate bias. Therefore, it is hypothesized that the reduction in interface trap density and hence the carrier scattering is attributed to the observed increased mobility of mixed stacked samples.

4.4 Summary and Conclusions:

We have successfully fabricated thin-film transistors using a solution-processed precursor solution for amorphous zinc tin oxide (a-ZTO). We have found a method to enhance the electrical characteristics of the transistors by stacking the layers with alternating precursor solution concentrations. In this letter, the enhancement in electrical characteristics of the thin-film transistors (TFTs) based on the multi-stacked amorphous zinc tin oxide (a-ZTO) with alternating precursor concentration is reported. The channel layers were deposited *via* sol-gel on oxidized p-Si. Source/drain ohmic contacts were prepared on the ZTO layer, and the bottom-gate TFTs were constructed. In this investigation, the TFTs with the following 3 channel layers were fabricated and their characteristics were compared; 1) layer produced from 0.05M precursor solution, 2) layer produced from 0.2M precursor solution, and 3) alternating layers with 0.05M and 0.2M precursor solutions. It was found that the mobility of the TFT fabricated with the channel layers with alternating precursor concentration was higher than those with single concentration. Even though the underlying reason for this mobility enhancement is not clear at this moment, it was conjectured that alternating precursor concentration might have reduced the trap density in the transistor channel.

4.5 References:

[1] Uprety, S., Hanggi, D., Yapabandara, K., Mirkhani, V., Khanal, M. P., Schoenek, B., ... & Sk, M. H. (2018). Enhancement of electrical characteristics of a-ZTO TFTs based on channel layers produced with alternating precursor concentration. *Electronics Letters*, *54*(22), 1298-1300.

[2] Ong, B. S., Li, C., Li, Y., Wu, Y., & Loutfy, R. (2007). Stable, solution-processed, high-mobility ZnO thin-film transistors. *Journal of the American Chemical Society*, *129*(10), 2750-2751.

[3] Jeong, S., Jeong, Y., & Moon, J. (2008). Solution-processed zinc tin oxide semiconductor for thin-film transistors. *The Journal of Physical Chemistry C*, *112*(30), 11082-11085.

[4] Kim, Y. H., Han, J. I., & Park, S. K. (2011). Effect of zinc/tin composition ratio on the operational stability of solution-processed zinc–tin–oxide thin-film transistors. *IEEE electron device letters*, *33*(1), 50-52.

[5] Seo, S. J., Choi, C. G., Hwang, Y. H., & Bae, B. S. (2008). High performance solution-processed amorphous zinc tin oxide thin film transistor. *Journal of Physics D: Applied Physics*, *42*(3), 035106.

[6] Li, C. S., Li, Y. N., Wu, Y. L., Ong, B. S., & Loutfy, R. O. (2009). Fabrication conditions for solution-processed high-mobility ZnO thin-film transistors. *Journal of Materials Chemistry*, *19*(11), 1626-1634.

[7] Hong, S., Park, J. W., Kim, H. J., Kim, Y. G., & Kim, H. J. (2016). A review of multi-stacked active-layer structures for solution-processed oxide semiconductor thin-film transistors. *Journal of Information Display*, *17*(3), 93-101.

[8] Uprety, S., Hanggi, D., Yapabandara, K., Mirkhani, V., Khanal, M. P., Schoenek, B., ... & Sk, M. H. (2018). Enhancement of electrical characteristics of a-ZTO TFTs based on channel layers produced with alternating precursor concentration. *Electronics Letters*, *54*(22), 1298-1300.

[9] Chiang, H. Q., Wager, J. F., Hoffman, R. L., Jeong, J., & Keszler, D. A. (2005). High mobility transparent thin-film transistors with amorphous zinc tin oxide channel layer. *Applied Physics Letters*, *86*(1), 013503.

[10] Wang, S. (2017). Radiation Hard Thin Film Transistors and Logic Circuits Based on ZnO and Related Materials.

Chapter 5

Facile microwave approach for the enhancement of electrical characteristics of ZTO TFTs.

5.1 Background:

Electromagnetic (EM) radiation, such as microwaves, can be reflected, transmitted, and/or absorbed by any kind of matter, conductors, water, ferrites, glasses, and so forth. Microwave (MW) consists of electric and magnetic fields that fluctuate sinusoidally in planes perpendicular to each other and propagate at the speed of light. EM radiation exhibits a dual nature, wave-like nature through interference and diffraction, and its particle-like behavior manifested by the photoelectric effect. The electromagnetic spectrum is classified according to regions of ascending frequencies or equivalently energies as radio waves, microwaves, infrared, visible light, ultraviolet (UV), X-rays, and gamma rays. Microwaves fall in the range of 300 MHz to 300 GHz, which correspond to 1m to 1mm wavelengths, respectively. Microwaves predominantly find their use in microwave heating, RADAR, electronic warfare, communications, radiation therapy, etc.

Unlike conventional heating, microwave heating occurs internally, and the heating rates are not limited to the heat transfer from an external heat source. Another essential characteristic of microwave heating is the reversal of the heating direction compared to conventional heating. Conventional heating occurs through heat flow from the external heat sources by processes such as conduction and convection such that the surface of the sample remains at a higher temperature than the core. However, heating occurs from the core as the Microwave traverses and generates heat inside the samples during microwave heating. Microwave features have led researchers to explore MW as an alternative to conventional heating, and considerable growth of microwave-assisted material processing has been observed in the last few decades [1]–[7].

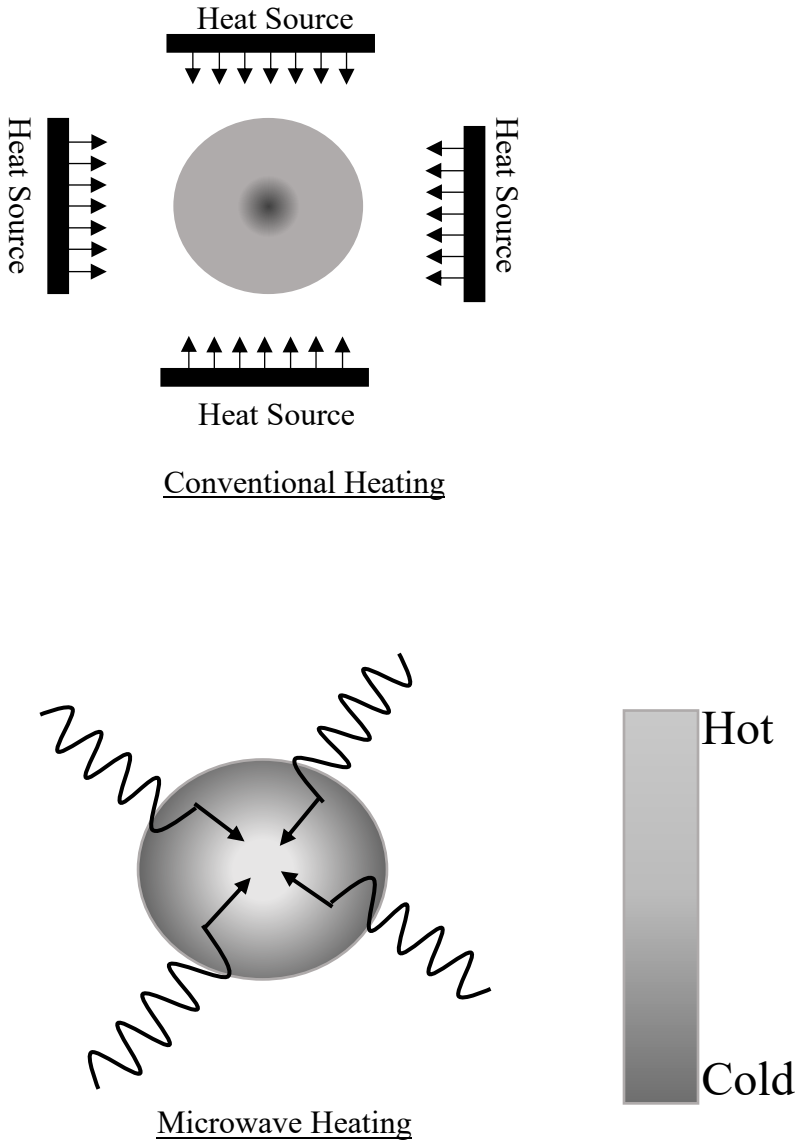

Figure 5.1: Conventional and microwave-induced heating patterns

Microwaves, in its use, differ from conventional processing of materials as it lacks [5].

- Controllable electric field distributions
- Rapid heating

- Penetration radiation
- Self-limiting reactions, and
- Selective heating of materials through differential absorptions

These features of a microwave, either alone or in combination, provide opportunities that are not available from conventional processing or heating and presents an alternative for the processing of a plethora of materials, including powders, a thin film of semiconductors, polymers, ceramics, composites, chemicals, and so on. However, the use of microwaves comes with challenges. Bulk materials with significant ionic or metallic conductivity are hard to be effectively processed due to insufficient penetration of the microwave energy. Insulators like SiO_2 and Al_2O_3 with low electric loss factors are difficult to heat from a room temperature due to little absorption of the microwave energy. These microwave heating limitations can be at least partially overcome by using susceptors with materials like SiC, carbon, and molybdenum silicide ($MoSi_2$) [8]. These are highly lossy materials that can couple with microwaves even at room temperature. They provide a comfortable and non-invasive technique to utilize rapid microwave processing even for highly Microwave transparent ceramics.

Generally, materials can be classified into three main categories based on their interaction with microwaves. (1) Opaque or conductors (electrical) in which microwaves are reflected and are not penetrated. (2) Transparent materials with low dielectric loss where microwaves are neither reflected nor absorbed but transmitted through with a little attenuation. (3) Absorbers or high dielectric loss materials absorb microwave energy (to a certain degree based on the value of dielectric loss factor) and subsequently convert it to heat. (4) Magnetic materials such as ferrites interact with the electromagnetic radiation's magnetic component and become heated [9]. Theoretically, the basis of microwave heating lies in how efficiently a particular material responds

to electromagnetic radiation. The two fundamental properties which measure the response of a material to an electric field are the permittivity or dielectric constant (ε') and dielectric loss (ε"). ε' is manifested as the ability of a material to store electric energy. At the same time, ε" determines the ability to convert the electric energy to heat. Similarly, the ability of a material to store and convert magnetic energy to heat is decided by the magnetic permeability (μ') and magnetic loss (μ"), respectively. Electric energy is stored *via* the polarization of bound charges. In contrast, the electric energy is converted into heat via the relaxation of the polarized molecules, which is often referred to as polarization loss and is also produced by free electrons' conduction.

Table 5.1: Examples of a few representative materials interacting with both electric and magnetic fields of the microwave for 2.45 Hz frequency [10], [11].

Material	ε'_r	ε''_r	μ'_r	μ''_r	$\tan\delta_e$	$\tan\delta_m$
Fe_3O_4	12.51	0.25	1.51	0.3	0.02	0.199
$NiZnFe_4O_4$	1.313	0.123	1.080	0.201	0.094	0.186
$BaFe_{12}O_{19}$	1.465	0.052	1.105	0.071	0.036	0.064
$CuZnFe_4O_4$	1.595	0.089	1.038	0.209	0.056	0.201
$CuFe_2O_4$	1.507	0.091	1.029	0.106	0.06	0.103

When all possible polarization mechanisms (dipolar, interfacial, ionic, and electronic) are considered, the effective dielectric equation can be written as

$$\varepsilon' = \varepsilon'_{dipolar} + \varepsilon'_{ionic} + \varepsilon'_{interfacial} + \varepsilon'_{electronic} \quad 5.1$$

$$\varepsilon'' = \underbrace{\varepsilon''_{dipolar} + \varepsilon''_{ionic} + \varepsilon''_{interfacial} + \varepsilon''_{electronic}}_{\text{Polarization Loss}} + \underbrace{\frac{\sigma}{2\pi f}}_{\text{Conduction Loss}} \quad 5.2$$

where σ is the conductivity of the material, and f is the frequency of the radiation.

Table 5.2: A few examples of transparent material, absorber, and reflector of microwave radiation along with their penetration depth and loss tangent values

Microwave Transparent material			Microwave Reflector		Microwave absorber		
Material	$\tan\delta_e$	d_p(m)	Bulk metal	d_p(μm)	Material	$\tan\delta_e$	d_p (cm)
Fused quartz[a]	0.0003	75.73	Al[a]	1.7	SiC[a]	0.37	1.93
Alumina	0.001	12.65	Ag[a]	1.3	Water	0.15	3
Borosilicate glass	0.0012	15.7	Cu[a]	1.3	Carbon black (20 μm)	0.23	5.75
Silicon[a]	<0.012	>3.96	Zr[a]	6.7	Graphite powder[b](20-80μm)	0.36-0.67	1.34-2.09
Silicon Nitride[b]	<0.001	>12.2	Au[a]	1.5	Charcoal[c]	0.14-0.38	6-11
Boron Nitride[a]	<0.0005	>35			Carbon Fibers[d]	0.45-0.5	0.5

[a] [12]–[15] [b] [16] [c] [17], [18] [d] [19]

Microwave heating basically occurs *via* the polarization loss for the dielectric insulating materials such as zirconia, alumina, quartz, *etc*., while conduction loss primarily contributes to the heating of the highly conducting materials such as metals under the electric field of the microwave. It might as well be noted that along with heating under the electric field, the heating also occurs under the magnetic field *via* several mechanisms such as eddy current loss, hysteresis loss, and domain wall/electron spin resonance loss [13], [19]. The dielectric and magnetic properties are usually reported as their relative values concerning the free space permittivity (ε_o) and permeability (μ_o), respectively and can be defined as

$$\varepsilon' = \frac{\varepsilon\prime}{\varepsilon_o}, \varepsilon''_r \frac{\varepsilon''}{\varepsilon_o}, \mu'_r = \frac{\mu\prime}{\mu_o} \text{ and } \mu''_r = \frac{\mu''}{\mu_o} \quad 5.3$$

Also, the ability of a dielectric material to absorb microwaves and store energy is given by the complex permittivity ε^* given by

$$\varepsilon^* = \varepsilon' - j\,\varepsilon'' \quad 5.4$$

the ratio of the dielectric loss to the dielectric constant is known as the loss tangent ($tan\,\delta$)which is given as,

$$tan\,\delta = \frac{k''}{k'} = \frac{\epsilon''}{\epsilon'} \quad 5.5$$

where k' and k'' are relative dielectric constant and relative dielectric loss, respectively, which are given as $k' = \frac{\varepsilon\prime}{\varepsilon_o}$ and $k'' = \frac{\varepsilon''}{\varepsilon_o}$. Therefore, the higher the values of dielectric constant and large values of dielectric loss or tangent loss, the materials couple with microwave with higher efficiency. Besides, the dielectric properties of a material are also dependent upon the temperature, purity, frequency, chemical state, and manufacturing process.

5.2 Microwave radiation as an alternate source of annealing:

Because of the characteristics mentioned above of microwave radiation, microwaves have been used as an alternative method of annealing for a plethora of materials, including thin-film perovskites such as $NiTiO_3$, and $CdTiO_3$, semiconductors such as Indium Tin Oxide (ITO), ZnO, ZTO, IGZO, and other ceramic materials, *etc*. [20]– [27]. Phani *et al*. studied the synthesis of nanocrystalline $ZnTiO_3$ perovskite thin films produced via the sol-gel process assisted by microwave radiation. For comparison purposes, two sets of annealing processes were involved. MW annealed films showed decreased grain size films, and slight stoichiometric change between the conventional and [28] microwave annealed films were observed. Song *et al.* investigated the low-temperature soluble Indium Zinc Oxide (InZnO) thin-film transistors by microwave annealing. Solution-processed IZO TFTs prepared at 150°C by microwave annealing showed improved device characteristics. The enhancement in the device characteristics was attributed to the improved crystallization at low temperatures made possible by microwave radiation [29].

Yoo *et al.* studied the low temperature. Solution-processed ZTO TFTs fabricated by thermal annealing and microwave radiation. It was found that the combination of conventional hot plate annealing, and microwave radiation would yield high-performance TFTs. XPS study confirmed that the residual hydrolysis in solution-processed ZTO films could be decomposed at low temperature by microwave radiation [28].

The microwave annealed ZTO layer showed the near absence of hydroxyl groups and more oxygen vacancies than the hot plate annealed ZTO channel layer. The enhancement of device characteristics was attributed to reduced hydroxyl groups and increased oxygen vacancies. The effect of microwave annealing on the electrical enhancement of amorphous oxide semiconductor (a-IGZO) TFTs was studied.

The TFTs performance with microwave annealing for 100s was discovered to be in fair competition with its counterpart with furnace annealing at 450°C annealed for an hour [30]. The XPS analysis was conducted. O 1s spectrum for the a-IGZO thin film with microwave annealing was deconvoluted with Gaussian functions into two components which centered at 530.6 and 531.4 eV, respectively. The lower binding energy peak centered at 530.6 eV originates from the lattice oxygen ions with neighboring metal atoms. The higher binding energy peak at 531.4 eV corresponds to O^{2-} ions at an oxygen-deficient region in the matrix of the IGZO film. The XPS results confirmed that the microwave annealing process assisted the oxygen ions binding with the metal atoms and suppressed the formation of the oxygen-deficient region in the a-IGZO when increasing both the microwave power and the annealing duration. Increased intensity in the 530.6 eV and decreased 531.4 eV peaks for Microwave annealed samples explains the improved device performance as microwave annealing facilitated the formation of lattice oxygen and eliminated the defects that originated from oxygen deficiency [30].

Cheong *et al.* investigated the rapid preparation of solution-processed IGZO thin films by microwave annealing and photoirradiation. MW annealing was employed for the added rapid heating of the precursor film. As per their study, applying microwave annealing for the film promoted the crystallization of IGZO film. MW annealing along with Vacuum Ultraviolet (VUV) irradiation was able to remove the hydroxide group from the sample, which consequently enhanced the TFT characteristics. Also, the current ON/OFF ratio was found to be improved by VUV irradiation and was attributed to the elimination of charge traps and improved M-O binding. Fuh *et al.* also studied the effects of microwave annealing on the nitrogenated amorphous IGZO TFTs for low thermal budget applications [31].

In this dissertation research, microwave annealing was performed on ZTO, and the change in the characteristics of the ZTO-based TFT was studied. A household microwave oven accompanied by a susceptor (microwave kiln) is used to annealing the ZTO film.

5.3 Experimental Set up:

ZTO solution is prepared as mentioned in chapter 3 section. ZTO solution is spin-coated on a silicon dioxide wafer and calcined on a hot plate at around 300°C and diced into 1cm × 1cm. The diced samples were then annealed in microwave kiln assembly. TFTs were fabricated by the usual photolithography process with Ti/Ir as Source/Drain contacts. Figure 5.2 shows the sample preparation process in detail.

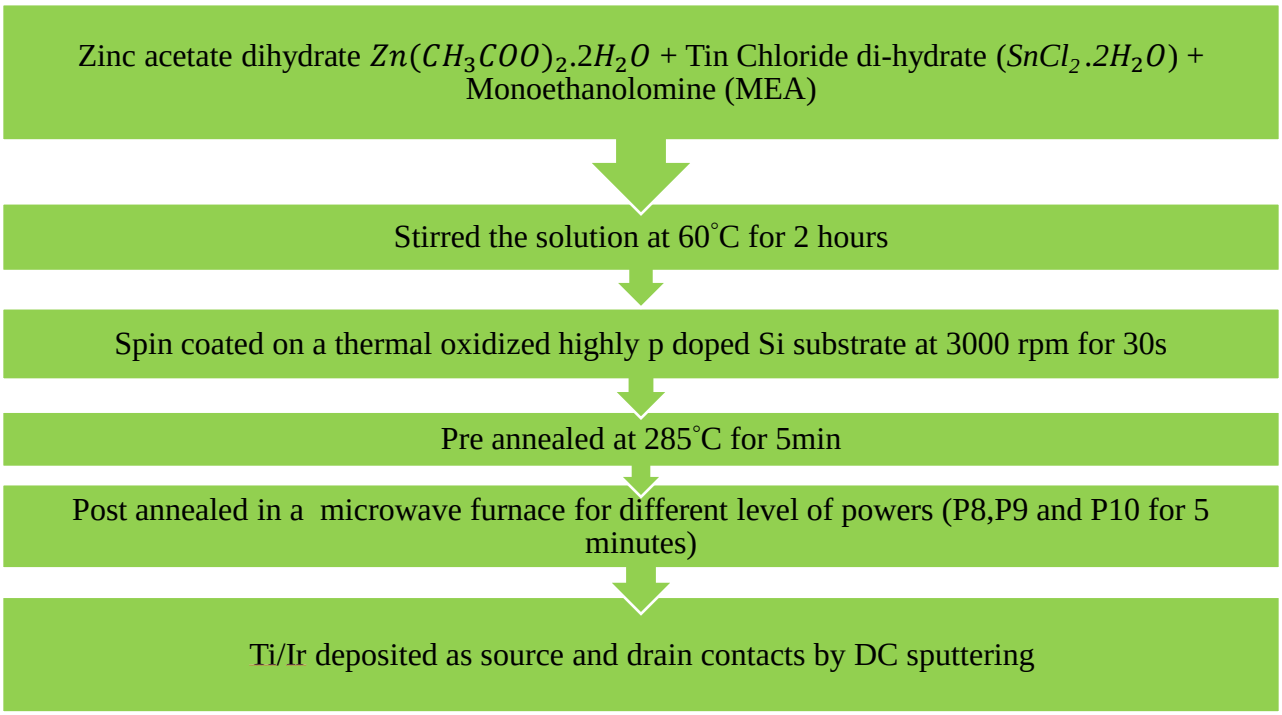

Figure 5.1: Flow chart for the process involved for the fabrication of the TFTs

Table 5.3: The annealing conditions for the ZTO films used in this study

Sample Name	Annealing Conditions
MW P8	Sample calcined on a hot plate for 5 mins at 285ºC, followed by annealing for 5 min. in a microwave oven at the 80% of the total microwave power (1250W)
MW P9	Sample calcined on a hot plate for 5 mins at 285ºC, followed by sample annealed in microwave annealing for 5 min. in a microwave oven at the 90% of the total microwave power (1250W) of microwave for 5 mins after calcination
MW P10	Sample calcined on a hot plate for 5 mins at 285ºC, followed by sample annealed in Microwave annealing for 5 min. in a microwave oven at the 100% of the total microwave power (1250W) of microwave for 5 mins after calcination

Figure 5.2: Microwave oven used for the annealing process

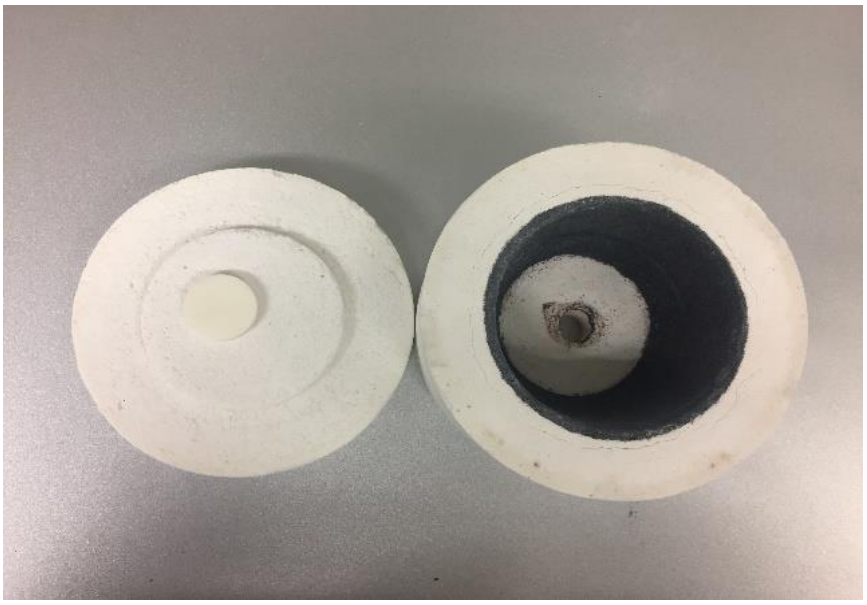

Figure 5.3: Microwave kiln used as a susceptor to assist the annealing process

The microwave kiln used in this experiment is composed of a porous ceramic body with a ring or inside coating of a high-temperature susceptor material (the black colored material).

5.4 Proposed Mechanism of heating:

Methoxy ethanol, among other glycols, has a permanent dipole moment and therefore is a suitable candidate for microwave heating experiments.

Table 5.4: Dielectric properties of glycols

Compound	Loss tangent at 2.45 GHz	Ref	Compound	Loss tangent at 2.45 GHz	Ref
Ethanol	1.26	a	1,7-Heptanediol	0.456	b
Ethylene glycol	1.35	a	2-Methoxyethanol	0.206	b
1,3-Propanediol	1.17	a	2-Ethoxyethanol	0.410	b
1,4-Butanediol	1.30	b	2-Butoxyethanol	0.282	c
1,5-pentanediol	0.783	b	Glycerol	0.301	c

[a] A. C. Kumbharkhane, S. M. Puranik and S. C. Mehrotra, *J. Sol. Chem.*, 1991, **21**, 201. [b]F. Wang, R. Pottel and U. Kaatze, *J. Phys. Chem.*, 1997, **101**, 922. [c]H. D. Purohit and R. J. Sengwa, *J. Mol. Liq.*, 1990, **47**, 53.

Table 5.4 provides the data for loss tangents for glycols used generally as solvents for solution process technique for thin film preparation. The loss tangent of water is 0.1, yet the heating rates are sufficiently high for 2.45 GHz frequency. Hence, it is plausible to say that solvents with a $tan\,\delta$ greater than 0.05 are suitable for microwave heating experiments.

Electromagnetic wave energy absorption ranges typically from 2 to 18 GHz for ZnO-based materials [32] (IGZO with a ($tan\,\delta$) of 0.77 [30] and ZnO with ($tan\,\delta$) 0.539). Hence, it is safe to assume ZTO; a ZnO-based semiconductor, absorbs microwaves effectively.

Also, as the microwaves heat the susceptor, heat is transferred to the wafer via the conventional modes of heat transfer. The insulating material, alumina, prevents heat loss to the microwave cavity and protects the microwave's functional unit. Thus, during the entire heating process, the susceptor heats the wafer or the sample from the surface, whereas the microwave heat

from the center. The reduced heat loss from the surface while the susceptors are present helps in maintaining the homogeneity during the hybrid heating and hence, the material undergoes more uniform and effective heating.

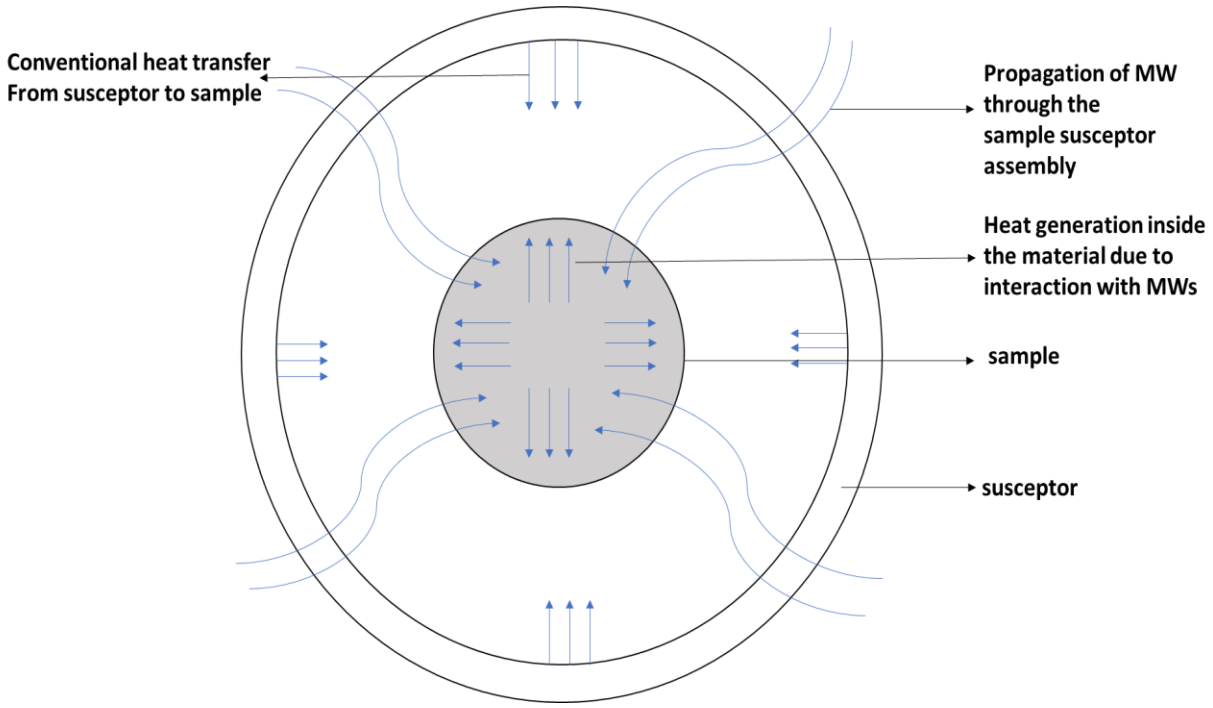

Figure 5.4: The two-way heating mechanism in the presence of external susceptor. Heating from the microwave occurs from the core of the sample, while the susceptor provides additional heating from the surface.

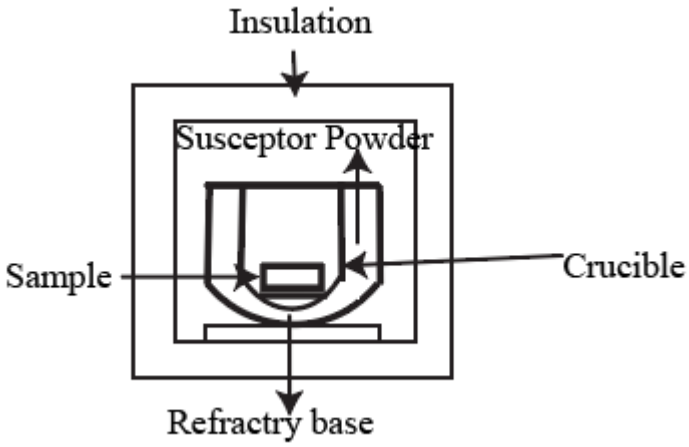

a.

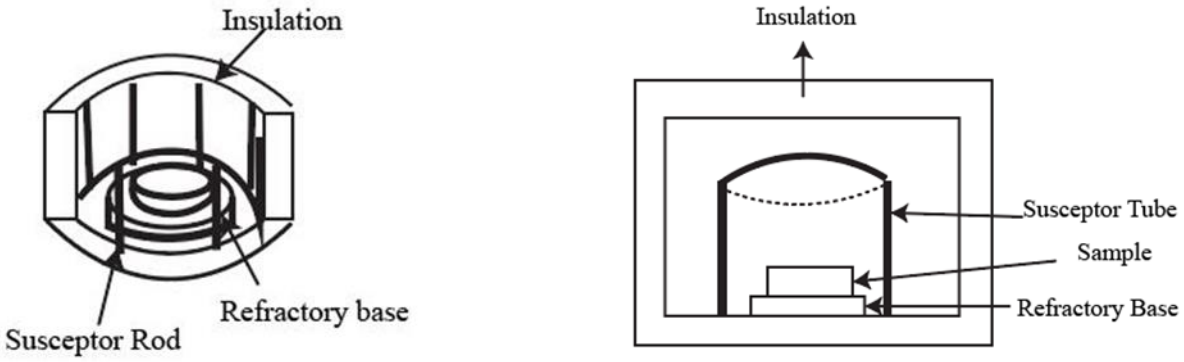

b. c.

Figure 5.5: Schematics of the primary hybrid heating configurations a) powdered (two crucibles set up), b) the picket fence arrangements c) tubular susceptor (like, used in this research)

5.5 Device Structure:

A 1 × 1 cm^2 sample with deposited ZTO was chosen for device fabrication. Circular source and drain (S/D) patterns were obtained by photolithography to achieve a Corbino geometry, with the inner circle (R_1 = 90μm) used as the drain and the outer ring (R_2 = 230μm) used as the source. Titanium was deposited as the ohmic contact, passivated by Iridium (Ir). The devices were then isolated *via* wet-etching to minimize the leakage current. The TFT active layers were kept unpassivated for characterization.

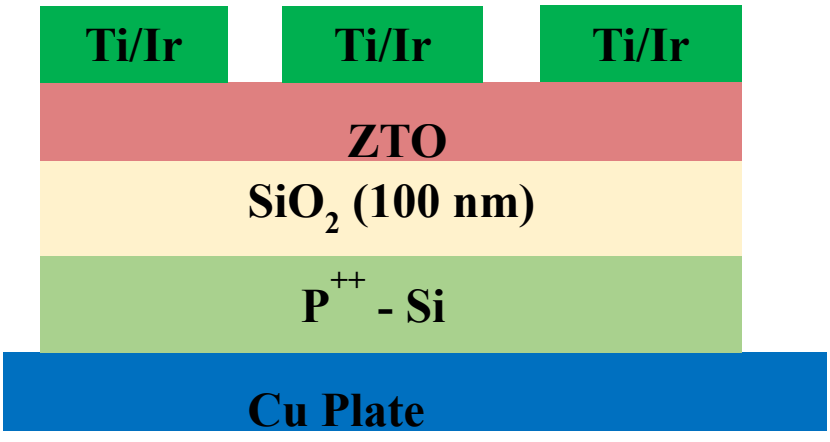

Figure 5.6: Schematic cross-section of the bottom gated ZTO TFTs.

Figure 5.7: Circular devices are used to isolate the device for other devices around it.

5.6 Material Characterization:

Sol-gel-produced films were characterized using X-Ray Diffraction (XRD) and X-Ray Photoelectron Spectroscopy (XPS). XPS was performed by Suresh Thapa, a graduate student in the Department of Physics, Auburn University. Figure 5.9 shows the XRD pattern performed by Ehsan Hassani at Dr. Oh's Lab in Chemical Engineering Department, Auburn University for hot plate annealed and microwave annealed films. Intense peaks were not observed, which led to our assumption that the films remained amorphous even after microwave radiation.

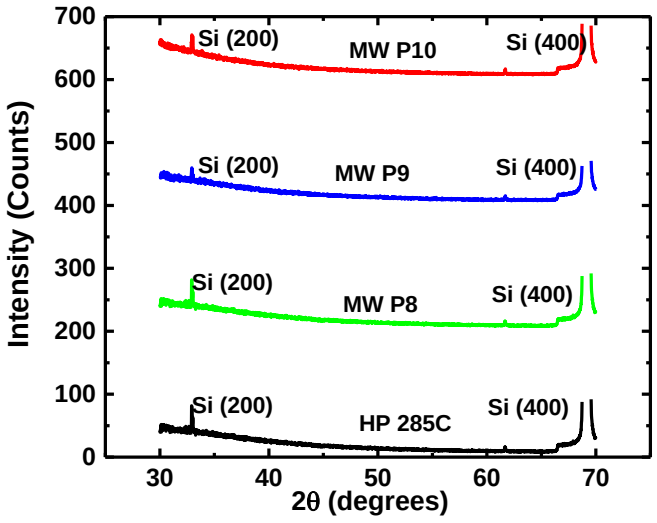

Figure 5.8: XRD plots of hot plate and microwave annealed samples

The properties of oxide semiconductor materials are largely dependent on defect structures of the materials. Figure 5.10 shows the deconvolution of Oxygen 1s peak to quantify the peaks. Table 5.4 and 5.5 show the surface elemental composition of the ZTO peaks and a summary of relative peak areas of the different components of XPS O 1s spectra from the film, respectively, for microwave annealed films at different powers. The peaks centered at~530 and~531 eV originate form lattice and defect oxygen such as those in vacancies, respectively. The peak around 532 eV could be assigned to surface oxygen such as those in hydroxyl groups. Hydrogen is more electronegative than metals, the oxygen atoms in M-OH species are less negatively charged than those in the oxide, which results in a shift towards higher binding energies.

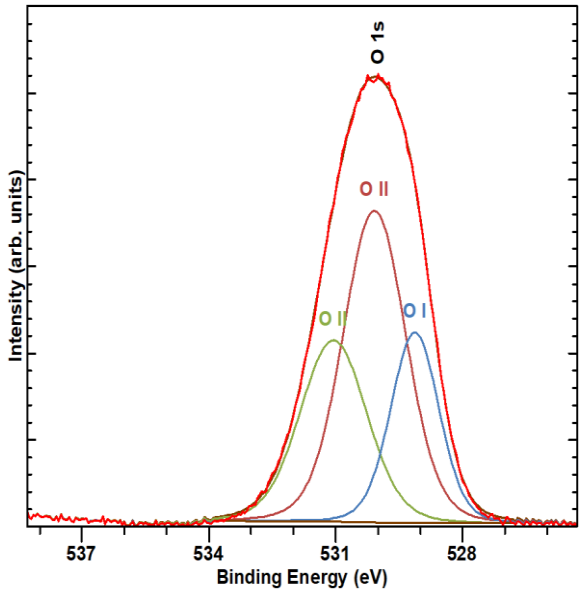

a.

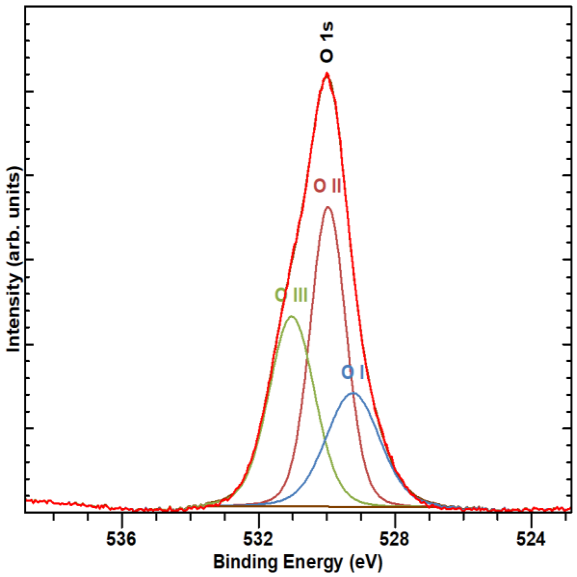

b.

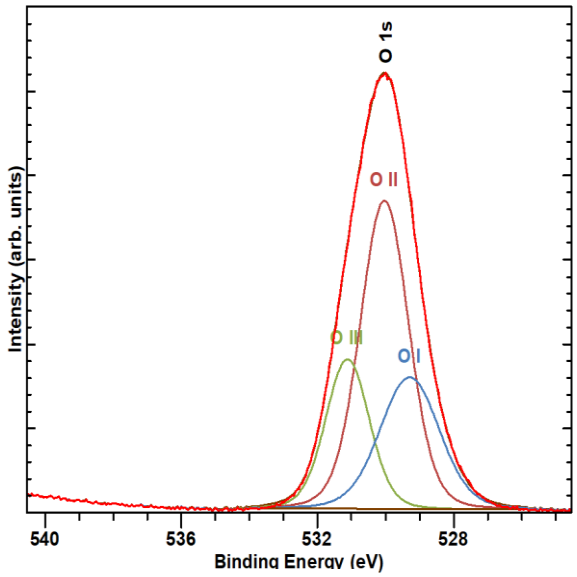

c

Figure 5.9: Deconvolution of 01s oxygen for a. microwave annealed sample at P8 b. microwave annealed sample at P9 c. microwave annealed sample at P10

Table 5.5: Summary of relative peak areas of the different component of XPS O 1s spectra from the films based on figure 5.10

Sample	O_I (%)	O_{II} (%)	O_{III} (%)
MW 8	23.97	42.06	33.96
MW 9	26.78	51.09	22.13
MW 10	22.52	47.92	29.56

According to the XPS data as listed in table 5.5, samples annealed at P9 of the microwave showed lesser amount on OH^- species in the film as compared to the samples annealed at P8 and P10. Hence, microwave irradiated samples for P9 of microwave were able to reduce the amount of hydroxyl groups effectively. It would be safe to assume that the metal hydroxides inside the solution processed ZTO films were converted to oxides via condensation reaction during irradiation.

5.7 Transistor Characteristics of Thin Film Transistors:

After the film characterization, TFTs were fabricated using the usual process of Photolithography and metal deposition and characterized using a Keithley 4200 semiconductor characterization system. Several TFTs were measured from each 1×1 cm^2 sample for transfer characteristics and a typical device was chosen from a sample to represent the general behavior of the set. The device characterizations were performed in the ambient for microwave annealed samples. Figure 5.10 represents the transfer characteristics for the microwave annealed samples in a linear scale and log scale respectively.

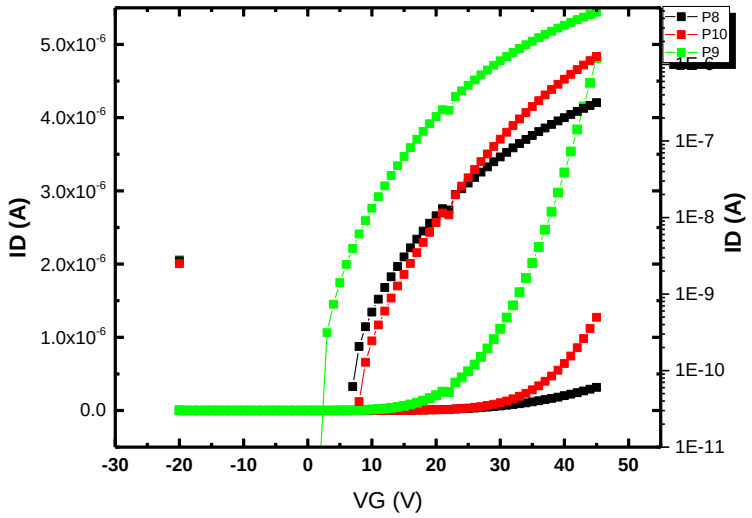

Figure 5.10: I_D vs. V_{GS} scale for microwave annealed samples

A few device characteristics such as field-effect mobility, interface trap density are calculated as provided by equation 4.1 and 4.2 respectively. The channel width length ratio is defined by

$$\frac{W}{L} = 2\pi\left(ln\frac{R_2}{R_1}\right)^{-1} \qquad 5.6$$

Table 5.6: Device properties of the representative of HP and microwave annealed samples

Samples	Mobility ($cm^2/V.s$)	Threshold voltage (V)	Interface trap density (10^{12} $eV^{-1}cm^{-2}$)	ON voltage (V)
P8	0.11	35	7.437	8
P9	1.46	26	1.738	3
P10	0.66	29	5.791	9

5.8 Results from the Transfer Characteristics of TFTs:

With the transfer characteristics of the microwave annealed samples, the threshold voltage and on voltage for the microwave annealed samples at P9 have decreased as compared to the P8 and P10. Subthreshold swing is reduced for the samples annealed at P9 power of the microwave compared to the P8 and P10 samples and hence the interface trap density, which in turn enhances the transistors' electrical performance.

5.9 Results from XRD and XPS:

X-Ray Diffraction (XRD) data were obtained and plotted using ORIGIN PRO. With respect to JCPDS file number 28-4881, the usual ZTO peak lies around 34°. Since no distinct peaks at around 34 degrees were not observed from XRD plots for both the hot plate and microwave annealed samples, it was believed that the films remained amorphous during the two types of annealing.

XPS data obtained for the microwave annealed films were quantified, and the surface elemental composition was obtained. Table 5.4, 5.5, and figure 5.10 show the elemental composition of the films. Oxygen quantity obtained is further deconvoluted into three categories according to their binding energies.

A plethora of analytical techniques have been utilized to characterize oxygen vacancies in transition metal oxides; namely, Thermogravimetric Analysis (TGA), Ultra-Violet Visible Spectroscopy (UV-Vis), X-Ray Diffraction (XRD), Photoluminescence (PL), Electron Spin Resonance (ESR), Electron Energy Loss Spectroscopy (EELS) and X-ray Photoelectron Spectroscopy (XPS) [32]– [35]. In this research, XPS was used for oxygen vacancy analysis. A standard technique is to deconvolute the O 1s peak into 3 Gaussian peaks (labeled as O_I, O_{II}, and

O_{III}) centered at around 530.5eV (O_I), 531.9eV (O_{II}), and 532eV (O_{III}) which are respectively attributed to lattice oxygen, defect oxygen (such as those in oxygen vacancies) and surface oxygen (such as that in hydroxyl groups) respectively [25]. Since hydrogen is more electronegative than metals, the oxygen atoms in M-OH species are less negatively charged than those in the oxide, resulting in a shift toward higher binding energies.

The data obtained showed the increase in the lattice and defect oxygen such as those in vacancies and decrease in the surface oxygen or loosely bound oxygen species such as those in hydroxyl groups. In general, microwave annealing along with the susceptor, which acted as a coupler, helped in the fast dihydroxylation. Since the hydroxyl group acts as traps in oxide semiconductors, it influences the threshold voltage. A decrease of such groups would reduce the threshold voltage for the microwave annealed TFTs. Also, interface trap density for the microwave annealed samples was found to be decreased, suggesting lower interface traps between the semiconductor dielectric interface, hence enhancing the TFTs' electrical performance. The XPS data also showed the general tendency of increasing the relative concentration of oxygen vacancies inside ZTO films. These oxygen vacancies are assumed to act as electron donors, increasing the carrier concentration shown in the figure above.

5.10 Conclusion:

ZTO thin was produced using the solution process. Three specimens were used to fabricate TFTs. XRD and XPS were performed to analyze the film crystallinity and surface elemental composition, respectively. O 1s spectra was Gaussian fitted to analyze the relative areas of the lattice oxygen, defect oxygen such as those in vacancies, and loosely bound oxygen species such as that in hydroxyl groups. In general, microwave-assisted annealing with an external susceptor enhanced the dihydroxylation at a very short period. Hydroxyl groups are polar and behave as

charge traps and influence threshold voltage. The lower threshold voltage for the microwave-assisted annealed at P9 is indicative of the presence of a small amount of hydroxyl groups. Interface trap density in the MW annealed films decreased, suggesting lower interface trap states between the semiconductor dielectric interface for MW annealed samples, hence enhancing the TFTs' electrical performance. The XPS data also show the general tendency of increasing relative concentration of oxygen vacancies inside ZTO films. The oxygen vacancies act as electron donors, increasing the carrier concentration.

5.11 References:

[1] Rosa, R., Veronesi, P., & Leonelli, C. (2013). A review on combustion synthesis intensification by means of microwave energy. *Chemical Engineering and Processing: Process Intensification*, *71*, 2-18.

[2] Bhattacharya, M., & Basak, T. (2013). A theoretical study on the use of microwaves in reducing energy consumption for an endothermic reaction: Role of metal coated bounding surface. *Energy*, *55*, 278-294.

[3] Sadler, S., Moeller, A. R., & Jones, G. B. (2012). Microwave and continuous flow technologies in drug discovery. *Expert opinion on drug discovery*, *7*(12), 1107-1128.

[4] Chandrasekaran, S., Ramanathan, S., & Basak, T. (2012). Microwave material processing—a review. *AIChE Journal*, *58*(2), 330-363.

[5] Singh, S., Gupta, D., Jain, V., & Sharma, A. K. (2015). Microwave processing of materials and applications in manufacturing industries: a review. *Materials and Manufacturing Processes*, *30*(1), 1-29.

[6] Kharissova, O. V., Kharisov, B. I., & Valdés, J. J. R. (2010). The use of microwave irradiation in the processing of glasses and their composites. *Industrial & Engineering Chemistry Research*, *49*(4), 1457-1466.

[7] Whitfield, P. S., & Davidson, I. J. (2000). Microwave Synthesis of Li1. 025Mn1. 975 O 4 and Li1+ x Mn2− x O 4− y F y (x= 0.05, 0.15; y= 0.05, 0.1). *Journal of the electrochemical society*, *147*(12), 4476.

[8] Bhattacharya, M., & Basak, T. (2017). Susceptor-assisted enhanced microwave processing of ceramics-a review. *Critical Reviews in Solid State and Materials Sciences*, *42*(6), 433-469.

[9] Chandrasekaran, S., Ramanathan, S., & Basak, T. (2012). Microwave material processing—a review. *AIChE Journal*, *58*(2), 330-363.

[10] Peng, Z., Hwang, J. Y., Mouris, J., Hutcheon, R., & Huang, X. (2010). Microwave penetration depth in materials with non-zero magnetic susceptibility. *ISIJ international*, *50*(11), 1590-1596.

[11] Peng, Z., Hwang, J. Y., & Andriese, M. (2012). Magnetic loss in microwave heating. *Applied Physics Express*, *5*(2), 027304.

[12] Gupta, M., & Sankaranarayanan, S. (2015). Using energy efficient microwaves to synthesize high performance energy saving magnesium (nano) composites. In *TMS 2015 144th Annual Meeting & Exhibition* (pp. 187-193). Springer, Cham.

[13] Appleton, T. J., Colder, R. I., Kingman, S. W., Lowndes, I. S., & Read, A. G. (2005). Microwave technology for energy-efficient processing of waste. *Applied energy*, *81*(1), 85-113.

[14] Whitfield, P. S., & Davidson, I. J. (2000). Microwave Synthesis of Li1. 025Mn1. 975 O 4 and Li1+ x Mn2− x O 4− y F y (x= 0.05, 0.15; y= 0.05, 0.1). *Journal of the electrochemical society*, *147*(12), 4476.

[15] Von Hippel, A. R. (1954). Dielectrics and waves.

[16] Hotta, M., Hayashi, M., Lanagan, M. T., Agrawal, D. K., & Nagata, K. (2011). Complex permittivity of graphite, carbon black and coal powders in the ranges of X-band frequencies (8.2 to 12.4 GHz) and between 1 and 10 GHz. *ISIJ international*, *51*(11), 1766-1772.

[17] Pickles, C. A. (2009). Microwaves in extractive metallurgy: Part 2–A review of applications. *Minerals Engineering*, *22*(13), 1112-1118.

[18] Wu, K. H., Ting, T. H., Wang, G. P., Yang, C. C., & Tsai, C. W. (2008). Synthesis and microwave electromagnetic characteristics of bamboo charcoal/polyaniline composites in 2–40 GHz. *Synthetic Metals*, *158*(17-18), 688-694.

[19] Hong, W., Xiao, P., Li, Z., & Luo, H. (2014). Microwave radial dielectric properties of carbon fiber bundle: Modeling, validation and application. *Carbon*, *79*, 538-543.

[20] Jo, K. W., & Cho, W. J. (2014). Improvement in gate bias stress instability of amorphous indium-gallium-zinc oxide thin-film transistors using microwave irradiation. *Applied Physics Letters*, *105*(21), 213505.

[21] Okuya, M., Ito, N., & Shiozaki, K. (2007). ITO thin films prepared by a microwave heating. *Thin Solid Films*, *515*(24), 8656-8659.

[22] Valitova, I. (2017). *Electrolyte Gated Metal Oxide Transistors* (Doctoral dissertation, École Polytechnique de Montréal).

[23] Phani, A. R., & Santucci, S. (2006). Microwave irradiation as an alternative source for conventional annealing: a study of pure TiO2, NiTiO3, CdTiO3 thin films by a sol–gel process for electronic applications. *Journal of Physics: Condensed Matter*, *18*(30), 6965.

[24] Kabongo, G. L., Ozoemena, K., & Dhlamini, S. (2018). Microwave irradiation induces oxygen vacancy in metal oxides-based materials and devices: A review. *J Nanosci Curr Res*, *3*(125), 2572-0813.

[25] Cho, W. J., Ahn, M. J., & Jo, K. W. (2017). Performance Enhancement of Solution-Derived Zinc–Tin–Oxide Thin Film Transistors by Low-Temperature Microwave Irradiation. *physica status solidi (a)*, *214*(12), 1700350.

[26] Bhattacharya, M., & Basak, T. (2017). Susceptor-assisted enhanced microwave processing of ceramics-a review. *Critical Reviews in Solid State and Materials Sciences*, *42*(6), 433-469.

[27] Phani, A. R., Passacantando, M., & Santucci, S. (2007). Synthesis of nanocrystalline ZnTiO3 perovskite thin films by sol–gel process assisted by microwave irradiation. *Journal of Physics and Chemistry of Solids*, *68*(3), 317-323.

[28] Valitova, I. (2017). *Electrolyte Gated Metal Oxide Transistors* (Doctoral dissertation, École Polytechnique de Montréal).

[29] Song, K., Koo, C. Y., Jun, T., Lee, D., Jeong, Y., & Moon, J. (2011). Low-temperature soluble InZnO thin film transistors by microwave annealing. *Journal of crystal growth*, *326*(1), 23-27.

[30] Teng, L. F., Liu, P. T., Lo, Y. J., & Lee, Y. J. (2012). Effects of microwave annealing on electrical enhancement of amorphous oxide semiconductor thin film transistor. *Applied Physics Letters*, *101*(13), 132901.

[31] Fuh, C. S., Liu, P. T., Teng, L. F., Huang, S. W., Lee, Y. J., Shieh, H. P. D., & Sze, S. M. (2013). Effects of microwave annealing on nitrogenated amorphous In-Ga-Zn-O thin-film transistor for low thermal budget process application. *IEEE electron device letters*, *34*(9), 1157-1159.

[32] Wang, Z. L., Yin, J. S., & Jiang, Y. D. (2000). EELS analysis of cation valence states and oxygen vacancies in magnetic oxides. *Micron*, *31*(5), 571-580.

[33] Guo, M., Lu, J., Wu, Y., Wang, Y., & UV, L. M. (2011). Visible Raman Studies of Oxygen Vacancies in Rare-Earth-Doped Ceria. *Langmuir*, *27*, 3872-3877.

[34] Nishida, K., Osada, M., Takeuchi, H., Yosiaki, I., Sakai, J., Ito, N., ... & Yamamoto, T. (2008). Raman spectroscopy study of oxygen vacancies in PbTiO3 thin films generated heat-treated in hydrogen atmosphere. *Japanese Journal of Applied Physics*, *47*(9S), 7510.

[35] Wu, Q. (2004). H.; Thissen, A.; Jaegermann, W.; Liu, M. *Photoelectron spectroscopy study of oxygen vacancy on vanadium*

Chapter 6

Gamma Irradiation Study on ZTO TFTs

6.1 Radiation in Space: Basics and Background

The impact of radiation on different materials and semiconductor devices is a wide field of study and modern science research. Radiation is form energy traveling in the form of rays, em waves, and/or particles. In some cases, radiation is visible or felt, while other forms such as x-rays and gamma rays are invisible. Radiation can generally be classified into ionizing radiation (high energy) and non-ionizing radiation (low energy). Ionizing radiation consists of particles or photons that possess enough energy to ionize an atom or molecule with the complete removal of an electron from its orbit, creating a more positively charged atom. Non-ionizing radiation with lesser energy does not have enough energy to dislocate electrons from the material it traverses. Ionizing radiation also produces secondary radiation, propelled into motion by the primary radiation particles and more damaging. The particles associated with ionizing radiation are mainly categorized as depending upon the radiation source: trapped radiation belt particles (Van Allen Belts), cosmic rays, and the solar flare particles.

6.2 Ionizing Radiation Sources

6.2.1 Galactic Cosmic rays (GCR):

Galactic Cosmic Rays (GCR) are the slowly changing, highly energetic background source of energetic particles that constantly bombard Earth. They originate outside the solar system and are likely formed by events such as supernovas [1]. These high-energy particles comprise basically every element ranging from hydrogen, accounting for approximately 89% of the GCR spectrum, to uranium found in the trace elements only [1]. These charged particles travel at significant

fractions of the speed of light and possess tremendous energy. After these particles hit the atmosphere, massive showers of secondary particles are created. Some of these particles even reach the ground. [2]. These particles present a minimal threat to humans and systems on the ground. The Earth's magnetic field works effectively to protect it from these particles, largely deflecting them away from the equatorial regions but providing insufficient protection near the polar regions or above roughly 55 degrees magnetic latitude (magnetic latitude and geographic latitude differ due to the tilt and offset of the Earth's magnetic field from its geographic center).

This constant shower of GCR particles at high altitudes can increase radiation exposure for crew members of an airplane and passengers at high altitudes and latitudes. Fred Singer, a U.S. based scientist, independently proposed a similar mechanism to describe the origin of the trapped electrons and protons trapped in radiation belts. Moreover, these particles can easily traverse or stop satellite systems, sometimes depositing enough energy resulting in errors or damage in spacecraft electronics and systems.

Primary cosmic radiation comprises gas and dust, which is gradually accelerated due to magnetic fields acting as large accelerators outside the solar system. These charged particles mainly consisting of electrons, protons, and neutrons spread over a range of energies, which can cause severe damage to the performance of the electronic components and other semiconductor devices [3][4]. The energy of these galactic cosmic rays can be as high as 10^{11} eV [5]–[7]

6.2.2 Solar Particle Events (SPE):

Solar Particle Events (SPE) occur when energetic electrons, protons, alpha particles, and more massive particles are injected into interplanetary space. These particles are accelerated close to relativistic speeds by the interplanetary shock waves preceded by fast Coronal Mass Ejections

(CME), and which exist in the vicinity of solar flare sites. Solar Flares are significant emissions from the sun containing protons, helium, and heavy ions [8], [9], and can have an energy higher than 0.1 GeV. During a massive SPE, the fluence of protons with energies ranging >30MeV can surpass 10^{10} cm^{-2} in several hours or days. This process can deposit large radiation doses for crew and equipment that are not sufficiently protected. Such significant events are infrequent to occur, and currently, there are no reliable methods to predict their occurrence. These hazards are potent enough to impose significant operational constraints on human-crewed space missions and equipment [10].

6.2.3 Trapped Particles in Radiation belts

The rotation of the Earth's molten core gives rise to electric currents that produce magnetic field lines around the Earth like those associated with a regular bar magnet, which stretches several thousand kilometers out from Earth's surface. A stream of particles produced by the sun, called the solar wind, varies in intensity with the sun's surface activity. It contains ions from almost every element, mainly protons and electrons. The interaction of these particles and the magnetic field forms a shock front around which the particles are deflected. The solar wind constricts and confines the magnetic field toward the sun and stretches it out into a long tail on the night side. Thus, this cavity is termed the magnetosphere, which shelters the Earth from the charged particles' continuous bombardment. The magnetosphere deflects only a part of the charged particles. Rest are trapped in the Earth's magnetic field [8]

6.3 Magnetosphere

An area of space around a planet, controlled by the planet's magnetic field, is called a magnetosphere. The shape of the Earth's magnetosphere possesses a dipole geomagnetic field, and

the solar wind alters these magnetic field lines. The solar wind squeezes its sunward side to 6 to 10 times the radius of the Earth. A supersonic shock wave is created sunward of Earth called the Bow Shock. Most solar wind particles are heated and slowed at the bow shock and detour around the Earth in the Magneto sheath. The solar wind drags out the night-side magnetosphere to possibly 1000 times Earth's radius, its exact length being unknown. This extension of the magnetosphere is known as the Magnetotail. The outer boundary of Earth's confined geomagnetic field is called Magnetopause. The Earth's magnetosphere is a highly dynamic structure that responds dramatically to solar variations [11]. The Van Allen Radiation belts are a part of Earth's dynamic magnetic environment known as the magnetosphere.

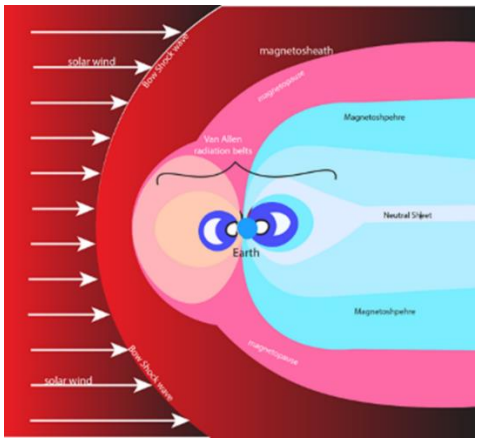

Figure 6.1: The Van Allen radiation belts contained within Earth's magnetosphere

A Van Allen radiation belt is a doughnut-shaped swath of energetic charged particles trapped at high altitudes in the Earth's magnetic field. The Van Allen radiation belt is a part of the Earth's magnetic environment known as the magnetosphere. Most of the inner belt comprises high energetic protons (0.1-40MeV), whereas the outer belt comprises energetic electrons (0.1-7MeV).

The zone was named after James A. Van Allen, the American physicist who discovered them in 1958, using data transmitted by the U.S. Explorer satellite. Van Allen's experiment on

Explorer 1, which launched Jan. 31, 1958, had a simple cosmic ray experiment consisting of a Geiger counter (a device that detects radiation) and a tape recorder. Follow-up experiments on three other missions in 1958 — Explorer 3, Explorer 4, and Pioneer 3 — established that there were two belts of radiation circling the Earth [12]. With technological advancement, artificial satellites have been launched for communications, navigations, atmospheric studies, remote sensing, military surveillance, etc. The conditions of these radiation belts pose a severe threat to these satellites [13]. Hence, a detailed study of the variation and behavior of the Van Allen belts is required. Within a span of twenty years, starting from 1920 to 1970, space missions such as "Combined Release and Radiation Effects Satellite" and NASA's "Solar Anomalous and Magnetospheric Particle Explorer" discovered essential information about the Van Allen radiation belts such as particle acceleration, loss of particles, and the high energy events during the solar activities. Van Allen probe mission was launched in 2012 by NASA, a dual spacecraft mission to explore the spatial structure and the dynamics of the radiation belts [14].

Table 6.1: Table 6.1 Characteristics of ionizing radiation for 1 MeV

	Electron (e)	Proton (p)	Gamma (γ)	Neutron (n)	Alpha (α)
Symbol	${}^{0}_{-1}e \; or \; \beta$	${}^{1}_{1}p \; or \; H^{+}$	${}^{0}_{0}\gamma$	${}^{1}_{0}n$	${}^{4}_{2}\alpha \; or \; He^{2+}$
Ionization	Direct	Direct	Indirect	Indirect	Direct
Charge	-1	+1	Neutral	Neutral	+2
Mass (amu)	0.000549	1.007276	-	1.008665	4.001506
Velocity (m/s)	2.82×10^{8}	1.38×10^{7}	3×10^{8}	1.38×10^{7}	6.944×10^{6}
Speed of light	2.3%	4.6%	100%	4.6%	2.3%
Range in air (cm)	319	1.81	82000*	39250*	0.56

*Based on 99.9% reduction

6.4 Effects of Radiation in Semiconductors

Modern electronic devices, fabricated with processes such as ion-implantation, e-beam, plasma etching, sputtering, ion milling, etc., can introduce radiation damage on them [15]. With the advancement of technology, the size of the electronic devices used in the electrical devices decreases rapidly, with a minimum thickness of dielectric being used in these devices. These devices possess a higher probability of being damaged due to radiation while being used in harsh radiation ambiance. When the practical applications of the microelectronic devices and components are considered, their use in the harsh radiation environment is unavoidable in space and terrestrial environments. Shielding is used to protect the system's electronic components' core components from subduing the effects of radiation [16]. But limitations of added weight and volume to the design of the system make it vulnerable. Radiation hard semiconductors that can perform without failing in these harsh environments are a simple and effective solution to such problems.

6.5 Total Ionizing Dose (TID) effects in Metal Oxide Semiconductors:

Charging of oxides, including gate oxide, field oxide, and isolation oxide, occurs by the process as detailed pictorially in figure 6.2.

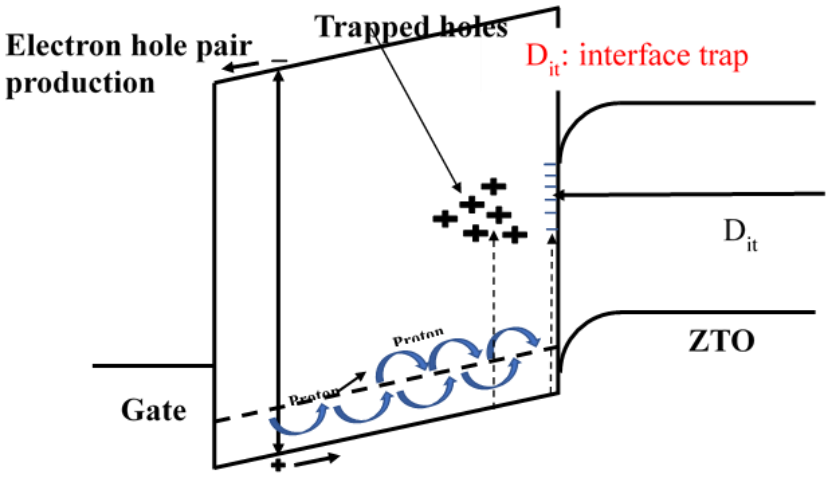

Figure 6.2: Schematic representation of primary radiation-induced e-h pair production with bulk hole trapping and movement of charge centroid to the interface under bias [23].

A simple case is considered where a positive gate voltage is applied to the gate metal, which bends the band in the MOS devices, as shown in the corresponding figure**.** When it traverses through the configuration, the photon of specific energy generates photoelectrons via the photoelectric effect. These photoelectrons, in turn, produce electron-hole pairs EHPs throughout the system. Hence created photoelectrons deposit their energy in the oxide losing around 17-18 eV (is SiO_2) for each EHP [21]–[23].

A fraction of the e-h pairs recombines. The recombination of the electron holes depends significantly on the energy and the type of incident particle. The holes, which escape initial recombination, are relatively immobile and remain near their point of generation. The remaining charges, mostly electrons, are swept away to the gate metal because of its higher mobility when a positive gate bias is applied. This phenomenon occurs in time scales of picoseconds. The slower drifting holes get trapped in the pre-existing traps and the microstructural defects in the oxide. These holes move slowly by the hopping mechanism towards SiO_2/Si (In our case, SiO_2/ZTO) through the localized states in the oxide [24]. As shown in the figure, the trapped holes generate

positive trap states in the dielectric layer to influence the threshold voltage for a device and influence the device's electrical stability.

6.5.1 Single Events Effects (SEE):

SEE are caused by a single, energetic particle and capable of taking any form. It can cause Single Event Upsets (SEUs) and are non-destructive. SEE can alter the operational state of the logic transistor. Two leading causes of SEEs are present in the space environment: cosmic rays and high-energy protons [25]. For cosmic rays, SEEs are generally caused by their heavy ion component. These heavy ions cause a direct ionization SEE. It means that if an ion particle moves through a device deposits enough charge, an event such as a memory bit alters, or transient might occur.

On the other hand, protons, usually trapped in the Earth's radiation belt or from solar flares, have the possibility of causing direct ionization SEEs in susceptible devices. Generally, there are two types of errors associated with SEE: soft error and hard error. Soft errors such as SEUs [26] are generated when the circuit's logic state is changed. The problematic errors lead to permanent functional defects because of the large amount of energy deposited in a small dielectric area, generally referred to as Single Event Gate Rupture (SEGR). This type of permanent damage can also occur from high current conditions arising from the passage of protons and other heavy ions, leading to a single event latch ups (SEL) [27]. Other forms of SEE, such as Sigle Event Transient [28], which leads to device failures, are discussed elsewhere [29], [30]

6.6 Non - Ionizing Damage:

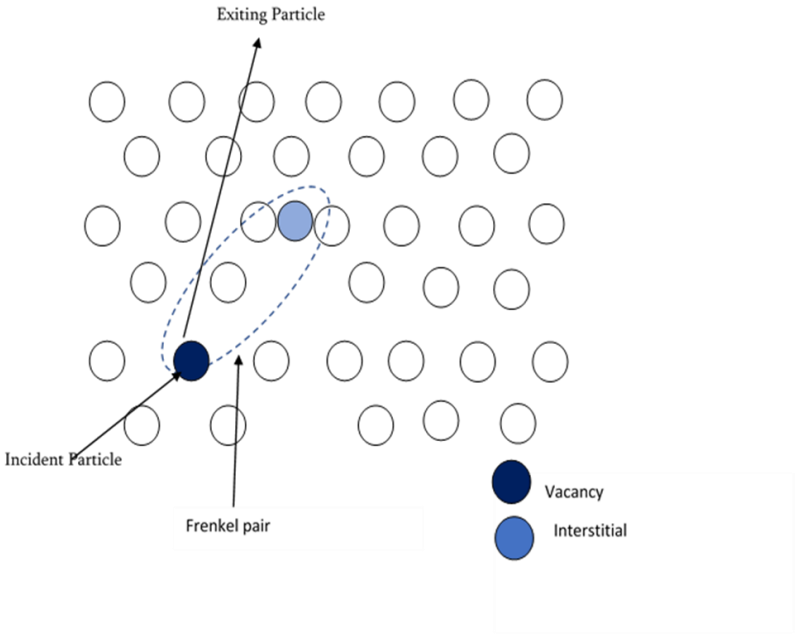

Figure 6.3: Displacement Damage

Non- ionizing damage, also known as atomic displacement damage, occurs ballistically via kinetic energy transfer or radiolytically by converting radiation-induced excitation into atom motion. When a charged particle passes through the matter, the energy dissipates by exciting orbital electrons and elastic collisions with the material nuclei. The transferred energy is enough to move the target atom from its normal lattice position to some other location creating a vacancy. The ejected is called a primary knock-on, which, in turn, may cause a cascade of atomic displacements before coming to rest. The figure below depicts how the displacement damage occurs in a lattice.

As shown in figure 6.3 above, the displaced atom becomes an interstitial, and the position atom previously occupied becomes a vacancy [31]. Together the interstitial and vacancy are referred to as a Frenkel pair. Some displaced atoms can also lead to secondary displacement.

An incident particle can stimulate a cascade of collisions to materialize to a portion of the affected material (e.g., Si) lattice atoms. These collisions are produced by both incident "heavy" particles such as protons, neutrons, and ions and secondary particles. Defects (vacancies, interstitials, Frenkel pairs, dislocations) are created along the secondary particles' tracks and clusters. Non-ionizing energy loss (NIEL) quantifies the displacement damage.

NIEL can be defined as the energy lost to non-ionizing events per unit length with units as MeV/cm or MeV·cm^2/g. The NIEL draws upon that the displacement damage effects are proportional to the non-ionizing particle's energy loss and the nuclear recoils procreated. A displacement damage dose can be computed from D_d = NIEL Φ. The production of vacancies and interstitials involves transferring particle kinetic energy to potential energy stored in the crystal lattice. Both vacancies and interstitials are mobile at sufficiently high temperatures, and annealing expedites their recombination. At the higher temperature, the atoms' vibration in the lattice increases, consequently providing a mechanism by which an interstitial atom can migrate to a vacancy; thereby, fixing both defects. Annealing, in some semiconductors, is believed to correct the induced defects introduced due to displacement damage [32].

6.6.1 Impurity Production:

Impurity Production generally refers to radiation-caused impurities except for any pre-existed impurities in any material. Impurities in a crystal constitute structural imperfections that can alter electrical and mechanical properties. Electrons and protons do not directly cause impurity production but may create impurity production through chemical bond breakage. Alpha particles and protons can cause Helium and Hydrogen buildup, respectively, to cause pressurization problems. The pressurization of the neighboring atoms can cause swelling and blisters in the material.

Neutron and ion irradiation can also help in the formation of radioactive species. When a nucleus captures a neutron, it does not necessarily change the chemical element but changes the isotope present. The novel isotope thus formed may be radioactive and decay, which has the potential to change the element itself [33].

6.6.2 Energy Deposition:

The ionization process is responsible for all the radiations to cause energy (and charge) deposition within the absorbing material. In water and organics, most of the absorbed ionization energy breaks chemical bonds. In metals, the bulk of the absorbed energy from ionization appears as heat. It is the kinetic energy deposition that generally manifests itself as thermal heating of the material. The equivalent temperature rise can change a slew of material properties. For direct heating by radiation, the product of the absorbed dose rate (dD/dt) and the material density (ρ) gives the volumetric heat generation rate, dQ/dt (i.e., the energy deposition rate per unit volume)

$$\frac{dQ}{dt} = \frac{dD}{dt}\,\rho \qquad 6.1$$

Table 6.2: Table 6.2 Radiation Damage to Materials (adapted from [34])

Radiation	Impurity Production	Atom Displacement	Ionization	Energy Release
Alpha	He buildup can cause pressurization problem	may cause atom displacement	Causes sizable ionization	over a very short range
Proton	H buildup can also cause pressurization	Yes	Directly	Yes, over a short range
Photon (γ and X-ray)	N/A	Rare displacements (Via Compton effect)	Indirectly	Gamma heating over considerable distance
Beta	N/A	Some displacement	Directly	Localized heat deposition
Thermal (eV) neutron	Directly by absorption reactions (mostly thermal neutrons), also may lead to more radiations	Indirectly	Indirectly	Indirectly
Fast (MeV) neutron				
Fission fragment	Become impurities themselves	Multiple displacements via scattering reactions; can cause displacement of "knock-on" atoms	These highly charged ions cause considerable ionization, and they emit β and γ	Considerable heat deposition over a concise range

6.7 Interactions of Gamma-irradiation with matter:

Gamma rays, also popularly known as gamma radiation, refer to the em radiation (no charge, no mass) of very high energy. Gamma rays can ionize atoms directly through the Photoelectric effect and the Compton effect, but secondary ionization imparts a more significant impact. Three important interaction mechanisms are responsible for any damage, such as ionization damage due to gamma irradiation.

1. Photoelectric effect
2. Compton Scattering
3. Pair Production

Charged Particles, such as electrons, protons, and alpha particles, on the other hand, interact by Coulomb interaction, causing both ionization and atomic displacements.

The photoelectric effect is the general form of interaction occurring when the gamma rays' energy is in a comparable magnitude of the energy binding the atomic electrons to the nucleus. Gamma rays can eject electrons away from atoms, sharing their energy between the electron and the excited atom. During this process, the vacancy is filled by one of the outer electrons, emitting characteristic soft em radiation in the X-rays, UV, or visible regions of the em spectrum**.**

Compton scattering is the most prevalent and dominant process of gamma ray's interaction with matter. It occurs for the gamma rays' relatively high energy (0.1-1MeV) depending upon the atomic number of the target atom. It involved a process when a gamma-ray photon collided elastically with a free electron. However, if the incident photon energy and momentum are much

larger than the binding energy and momentum of the interacting electron, the electron's state can be approximated as free and at rest. In this case, a gamma-ray can interact with a loosely bound electron by being scattered with an appropriate loss in energy.

When the gamma rays' energy exceeds much higher (>1MeV), the photon interacts with a nucleus producing an electron and a positron. The gamma-ray energy is transferred to the matter, with the nucleus's strong electric field helping as a catalyst. This pair production phenomenon often happens compared to the Compton effect for higher energies but is less likely in radioactive phenomena [35].

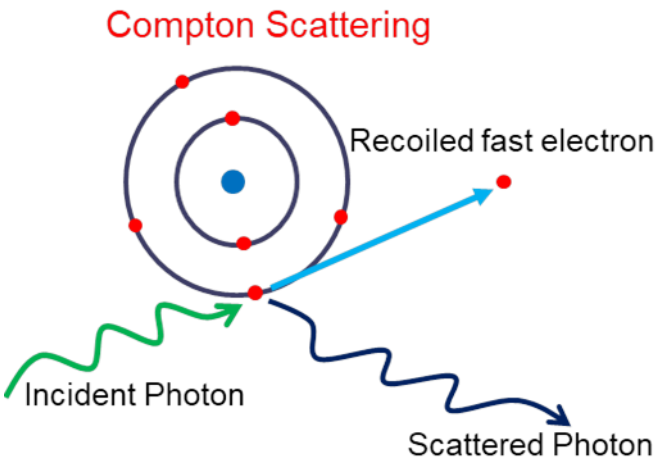

Figure 6.4: Compton Scattering

6.8 Types of Damages in Semiconductors

When exposed to high-energy radiation, semiconductors and semiconductor devices ought to receive energy and are deposited onto. The energy in the semiconductors is stored via two mechanisms, atomic collisions, and electronic ionization. The importance of these mechanisms depends upon the type of radiation and the nature of the device. For environments dominated by

electron, proton, and γ-ray, most deposited energy goes into the ionization process, *i.e.*, pair production and excitation, whereas for fast neutron environments, most of the deposited energy results in the atomic displacement damage from collisions [17].

The damaging ramifications on the electronic devices' performance when they are exposed to radiation are known as radiation-induced damage. The damage's extensiveness depends upon the parameters such as dose, energies, type of radiation, and the material itself. Radiation-induced damage can thus be divided into two main categories:

1. Ionization Damage
2. Displacement Damage:

6.8.1 Ionization Damage:

Ionization loss occurs when an incoming charged radiation loses energy after it strikes a target atom. The lost energy is then transferred to an electron, making it jump to the conduction band from the valence band, henceforth creating a hole in the valence band. This phenomenon created an electron-hole pair in the material under study. The number of e-h pairs depends upon the energy required to create a pair. The charged particles such as α, β, and proton induce direct ionization, whereas neutral radiations such as γ-rays and neutrons cause indirect ionization to the material. The type of bonding in the material also plays a vital role in determining ionization damage. Ionization damage for the materials with metallic and ionic bonds does not suffer permanent damage. In contrast, materials that possess covalent bonds suffer permanent damage since ionization can easily break the bonds into their constituent atoms radicals [18]. The best-known degradation effect of ionization damage is charge trapping by the pre-existing or radiation-induced trap sites. It causes the deterioration of the resolution of a solid-state nuclear detector. It

produces an increase in the charge transfer inefficiency (CTI) of Charge Couple Devices (CCDs) used for imaging or spectroscopy purposes [19].

Ionization damage can occur due to these main mechanisms categorized as,

a. Total Ionizing Dose (TID) effect
b. Single Event Effects (SEE)

6.8.2 Total Ionizing Effect (TID)

Total ionizing dose-effect refers to the cumulative long-term ionizing damage due to charges resulting in a charge buildup at the interfacial regions or boundaries, which causes failures in the electronic devices [20]. TID is a severe problem as it may elevate to several hundreds of kilorads during the lifetime of a space mission. It also serves as a measure of the amount of radiation a device can sustain before it fails to operate. TID effects generally affect threshold voltage, causing a shift in it, increasing leakage current, altering the channel layer, degrading the crystal quality, *etc*. These shifts in parameters cause the failure of the circuits used in the electronic devices.

6.9 Gamma Irradiation Effect on Semiconductors and Devices:

Efficiently and Properly designed Silicon-based devices are usually radiation-tolerant, but most TFTs, including polysilicon and a-Si: H are found to highly degrade under gamma irradiation with dosage as small as 20 kGy [36], [37], [38], [39]. Hence, there emerges a need to study the structural stability, and the device performance of the devices fabricated on other different semiconductors searching for a radiation tolerant substation for silicon [40]–[45]. ZnO based devices have been studied under the irradiation due to various energetic particles such as electrons [46]–[51] [52]–[54], protons [55]–[57], neutrons [58]–[60], ions [61]–[64]. Ramirez *et al.* studied

the radiation tolerance for ^{60}Co gamma irradiation (100 MRad (SiO_2)) and electrical stress on ZnO TFTs with dielectric layer deposited by plasma-enhanced atomic layer deposition (PEALD). A negative Von shift and a smaller Vt shift (ΔV_{ON}~2.5v and ΔV_{th}~-1.5V) was observed irrespective of electrical bias during irradiation. Field effect mobility was unchanged even after the radiation and was concluded that ZnO TFTs were radiation resistant [65]. The effect of gamma irradiation on low temperature Indium Zinc Oxide TFTs were conducted by Indluru *et al*. A negative turn on voltage shift and SS swing degradation were observed after irradiation with a total dose of 1.7 MRad. Increase in mobility from 2.8 to 8.8 $cm^2/V.s$ was also observed.

The changes in the irradiated TFTs' electrical properties were attributed to the combined effects of interface state increment and the e-h pair generation in the dielectric layer [66]. Lee *et al.* investigated the reliability of gamma irradiated ZnO TFTs for a total dose of~60kGy (SiO_2). During the first total dose of~40kGy a positive threshold voltage shift was observed. However, in the second irradiation with a total of 60kGy the threshold voltage shift moved in the other direction. This reversal of threshold voltage was attributed to the influence of the irradiation induced interface and oxide charges, having opposite polarity. It was also mentioned that, during the first regime of the irradiation, oxide charges were dominant over the density of interface traps and caused a positive shift. When the total dose were greater than 40kGy, the irradiation induced interface traps were conjectured to be greater than the oxide charges and caused the threshold voltage shift in other direction [67].

ZnO thin films' structural and optical study was conducted under the low dose rate of Co-60 gamma irradiation (1.25MeV). ZnO thin films of different thicknesses were used. Photoluminescence intensity increased with the increase of the irradiation dose for all the films. XRD data indicated no significant change in the grain size after the gamma irradiation. The optical

band gap was found to be decreased after the irradiation with different doses [68]. The effect of gamma irradiation on the stability of a-IGZO metal-semiconductor-metal UV photodetectors was investigated by Huang *et al*. The I-V measurements showed the ideality factor increased marginally, and the Schottky barrier height decreased slightly when the cumulative dose is increased, demonstrating a-IGZO retaining its electronic characteristics and not significantly affected by irradiation. The increase of the photo response of the Photodetectors (PDs) was attributed to creating more Oxygen vacancies, which produced more carriers and hence the increase in photocurrent [69]. Effects of high dose gamma irradiation on pulsed laser deposited Indium Tin Oxide (ITO) thin film properties were studied by Alyamani *et al.* [70]. Changes in the optical and electrical films were investigated. The intensity in the diffraction peaks and the film's structure was found to be altered with the increased irradiation dose. ITO film's resistivity was found to be reduced and was attributed to the increase in the oxygen vacancies and hence the increase in the electron concentration [70].

Gamma irradiation of solution-processed oxide semiconductors is still a matter of concern. We have irradiated our ZTO samples, and the devices fabricated on ZTO films with ^{60}Co radioactive isotope. We will discuss the electrical and structural properties of the ZTO thin films and fabricated TFTs from here onwards.

6.10 Experimental

ZTO thin film was grown using the sol-gel process by dropping the solution onto the substrate after filtering it through the 1.2um syringe filters. The solution was spun for 30 secs at 3000 rpm and calcined at a temperature of 285°C for 5 minutes four times to remove the organic residuals through evaporation. The solution's molar concentration was maintained at 0.3M, and the ratio of Zn:Sn was 7:3. Dry highly oxidized boron-doped Si wafers purchased from university

wafers, with 0.001 ohm.cm resistivity, the oxide thickness of 100nm, and <100> orientation, were used as substrates.

After calcination, the films were annealed at 500C for one hour in the box furnace. Source and drain were patterned photolithographically with Ti/Ir metal contacts deposited using DC magnetron sputtering system. The devices were isolated, forming a mesa structure by a wet etching method using BOE to help reduce the gate leakage current. Silver paint was coated on the scratched back surface of the Silicon substrate and attached to a copper plate to form a gate metal contact. For the irradiation, a ^{60}Co source stored approximately 20-25-foot-deep well of water (used for shielding purposes) during non-exposure was used. The ^{60}Co source was remotely brought out of the water-filled radiation shielding well to irradiate the samples.

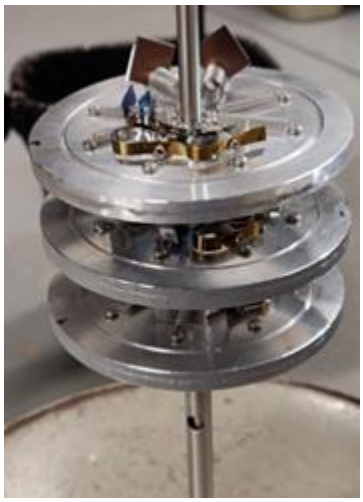

Figure 6.5: Sample Mount Schematics for the irradiation experiment

The American Society for Testing Materials (ASTM) standard and guidelines were used to define the proper dosimetry system and confirmed the field uniformity and intensity of the gamma-rays coming from the ^{60}Co panoramic irradiator. MAXX 4000 Standard Imaging Dosimeter was used to measure the dose-rate. The dosimeter was calibrated by comparison to a NIST source using a scintillation detector. The samples were held with springs in a house-made

structure, as shown in figure 6.5. Each week a sample was taken and characterized with a total of four samples during four weeks of irradiation. Each week a sample received a total dose of 14.26MRad, 28.52MRad, 42.78MRad, and 57.04MRad, respectively, with a dose rate of 23.59 rad/sec.

6.11 Results and Discussion:

A formerly established annealing temperature of 500°C is used for annealing the samples. Figure 6.6 below shows the XRD diffraction pattern of the pristine and irradiated samples. XRD analysis was performed using a Proto-AXRD theta-theta diffractometer with an X-ray K_α line from the Cu target with a 40 kV at 30mA. Ehsan Hassani performed XRD at Dr Oh's lab in the Department of Chemical Engineering, Auburn University.

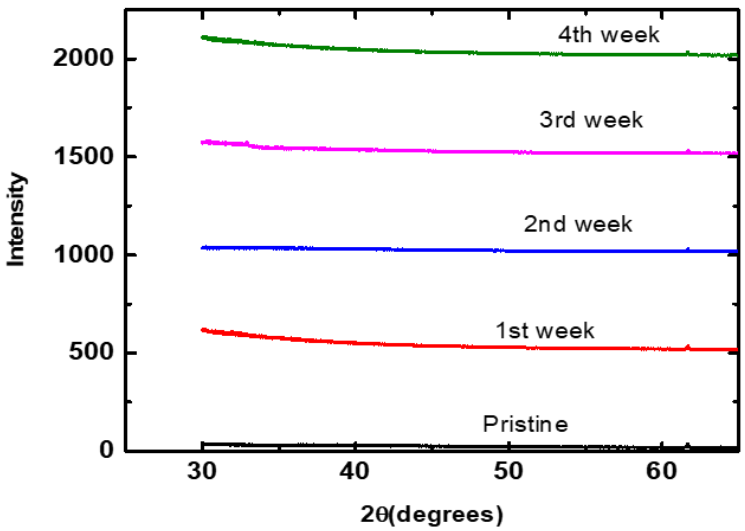

Figure 6.6: XRD peaks of the samples before and after irradiation

ZTO films usually show a peak around 2Θ~ 34º, as reported in JCPDS (number 28-1486). No significant peaks were observed, confirming the films remained amorphous during the four weeks of irradiation.

Park Systems AFM was used to measure the surface roughness of the films before and after the irradiation. Figure 6.7 below shows the AFM images (5μm × 5 μm) for pristine and irradiated samples performed by Suman Das to measure the samples' surface roughness.

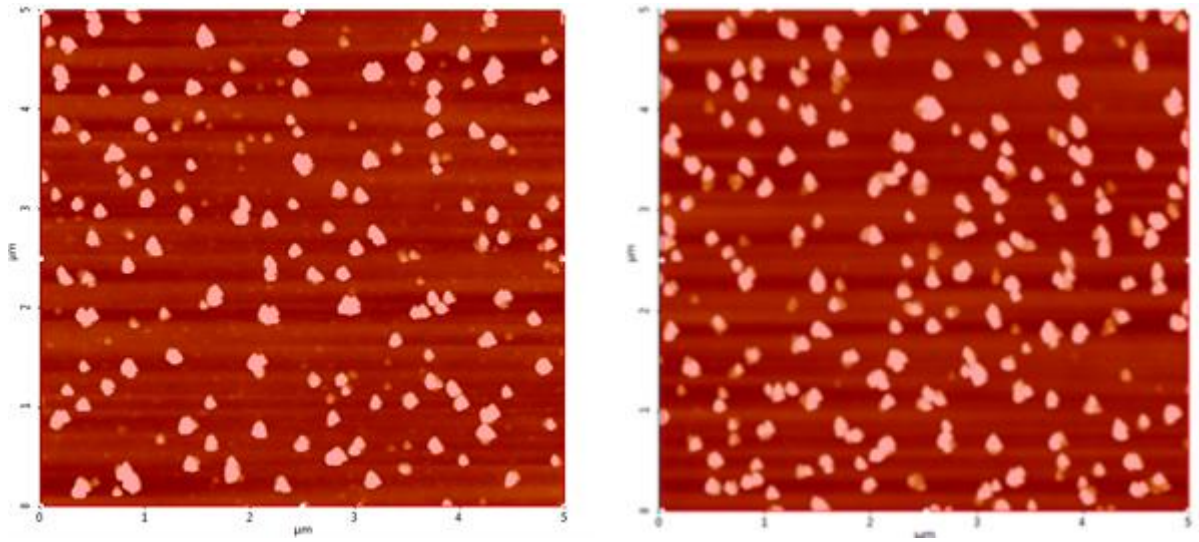

a. b.

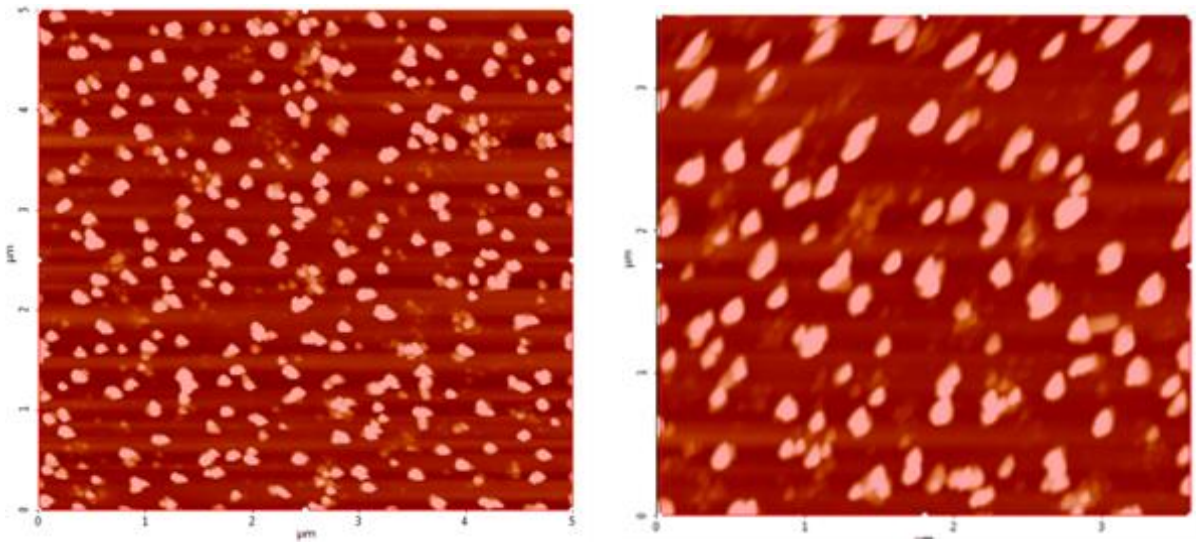

c.

d.

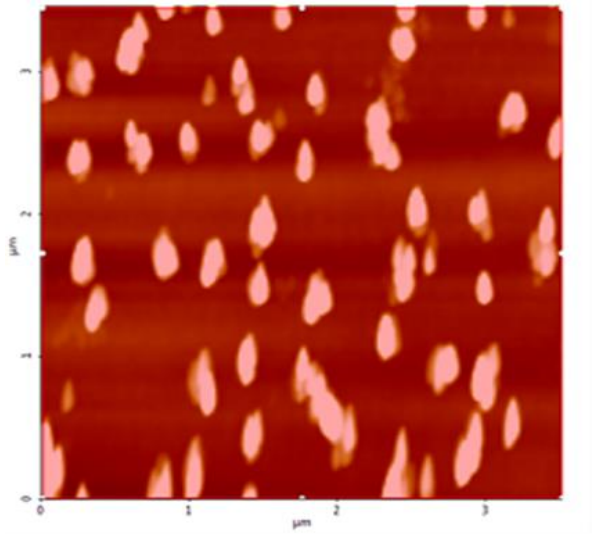

e.

Figure 6.7: 5µm ×5µm AFM images of a. pristine b. 1st week irradiated sample c. two weeks irradiated sample d. three weeks irradiated sample e. four-week irradiated sample

Table 6.3: Surface Roughness measurements of Pristine and Irradiated samples

Sample	Surface Roughness (Rq)
Pristine	5.945 nm
1st week	8.598 nm
2nd week	8.909 nm
3rd week	9.981 nm
4th week	8.879 nm

The surface roughness of the irradiated samples is increased, which might have been caused by the introduction of point defects and increased local disorder of the material. It also could be one of the reasons for the decrease of the field-effect mobilities in the TFTs irradiated with gamma radiation. The increase in the surface scattering of the charges due to the increase in surface roughness could be attributed to reducing the mobility of the irradiated devices.

XPS of the samples were performed using PHI 5400 XPS S (Al Kα X-ray source) system through an ultra-high vacuum (UHV) transfer line. An electron neutralizer gun was applied to compensate charging of the insulating samples. The surface stoichiometry of all grown samples was characterized by analyzing core level XPS spectra measured with a base pressure of ~1×10-9 torr. Analysis of the XPS data was performed using Casa XPS. To properly align all core level peaks, the metallic O 1s peak was aligned to 530.0 eV.

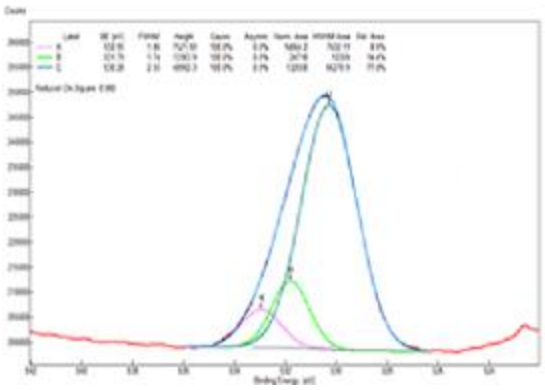

a.

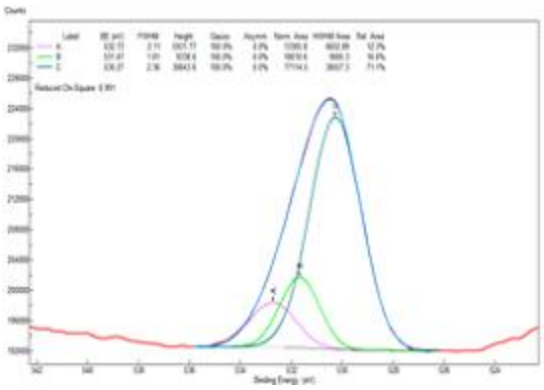

b.

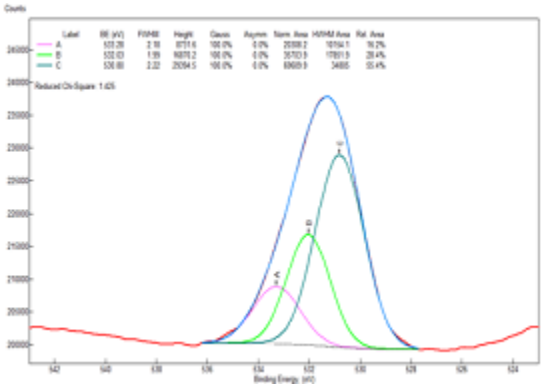

c.

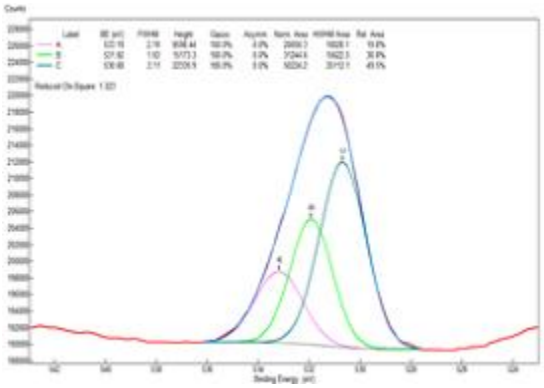

d.

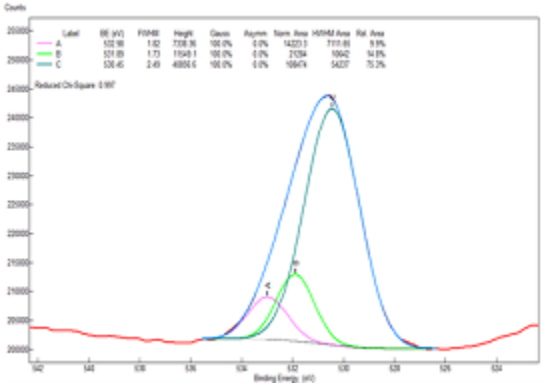

e.

Figure 6.8: O 1s deconvolution of Pristine and Irradiated samples. a. Pristine b. First-week c. Second-week d. Third-week e. Fourth week as performed by Dr. Bozack.

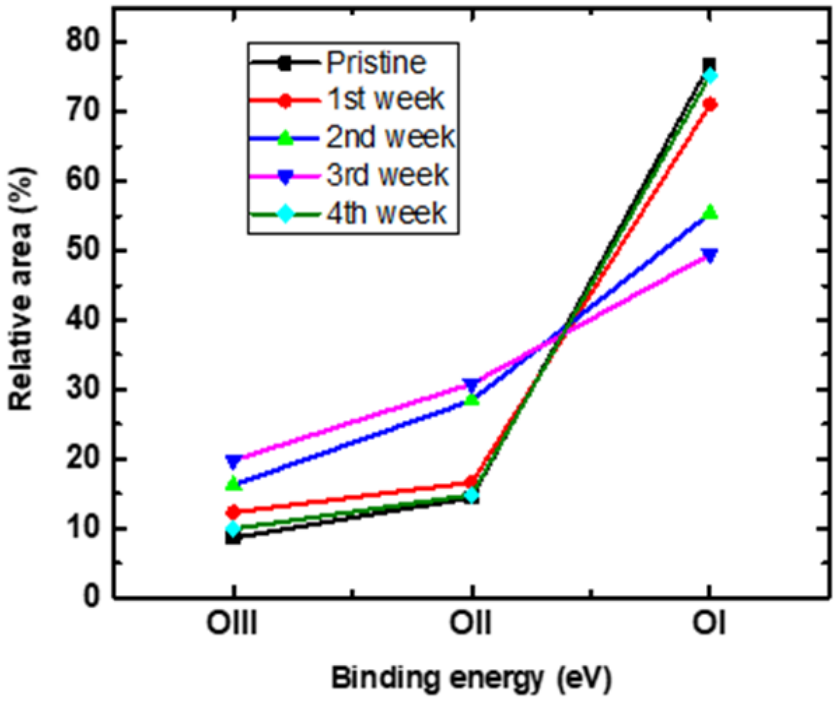

Figure 6.9: Summary of XPS Analysis of Pristine and Irradiates samples. O 1s oxygen peak is deconvoluted into its three components as OI, OII, and OIII

Device measurements and film analysis were carried out before and after the irradiation to compare the irradiation effects in the ambient. The current-voltage (I-V) and capacitance-voltage (C-V) measurements were taken with a Keithley 2400 Source meter and Keithley 590 CV analyzer. Gate voltage was modulated from -20V to 45V at the step of 1V. Figure 6.12 and 6.13 shows the transfer characteristics of the pristine and irradiated films in a linear and log scale respectively.

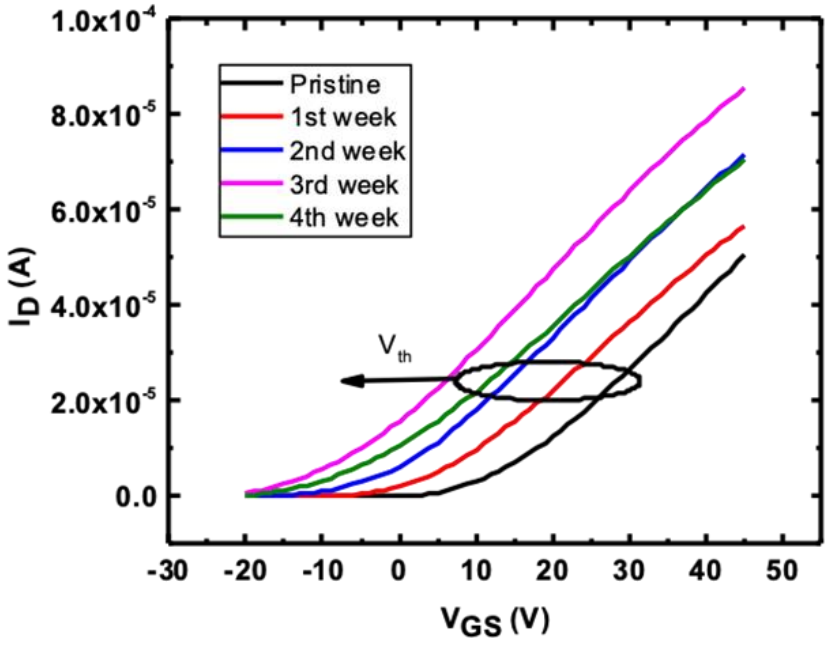

Figure 6.10: Transfer characteristics for V_{th} of Pristine and Irradiated devices in linear scale

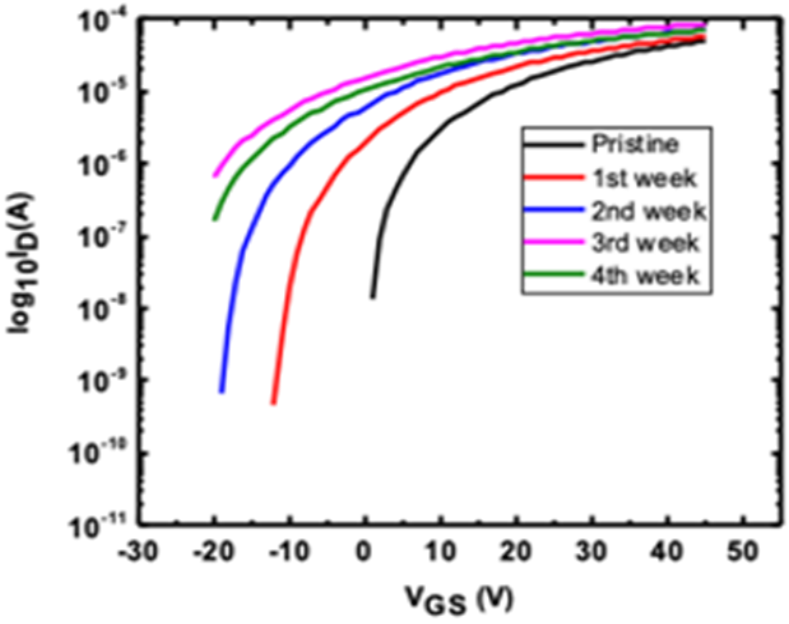

Figure 6.1311: Transfer characteristics for V_{th} of Pristine and Irradiated devices in logscale

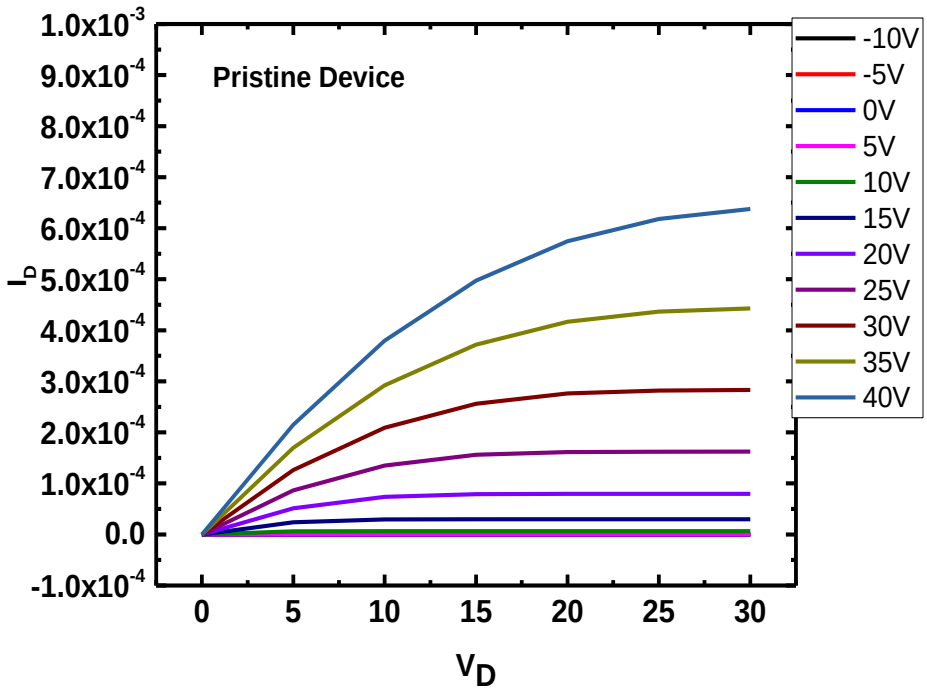
Pristine Device
-10V
-5V
0V
5V
10V
15V
20V
25V
30V
35V
40V
1.0x10-3
9.0x10-4
8.0x10-4
7.0x10-4
6.0x10-4
5.0x10-4
4.0x10-4
3.0x10-4
2.0x10-4
1.0x10-4
0.0
-1.0x10-4
ID
0
5
10
15
20
25
30
VD

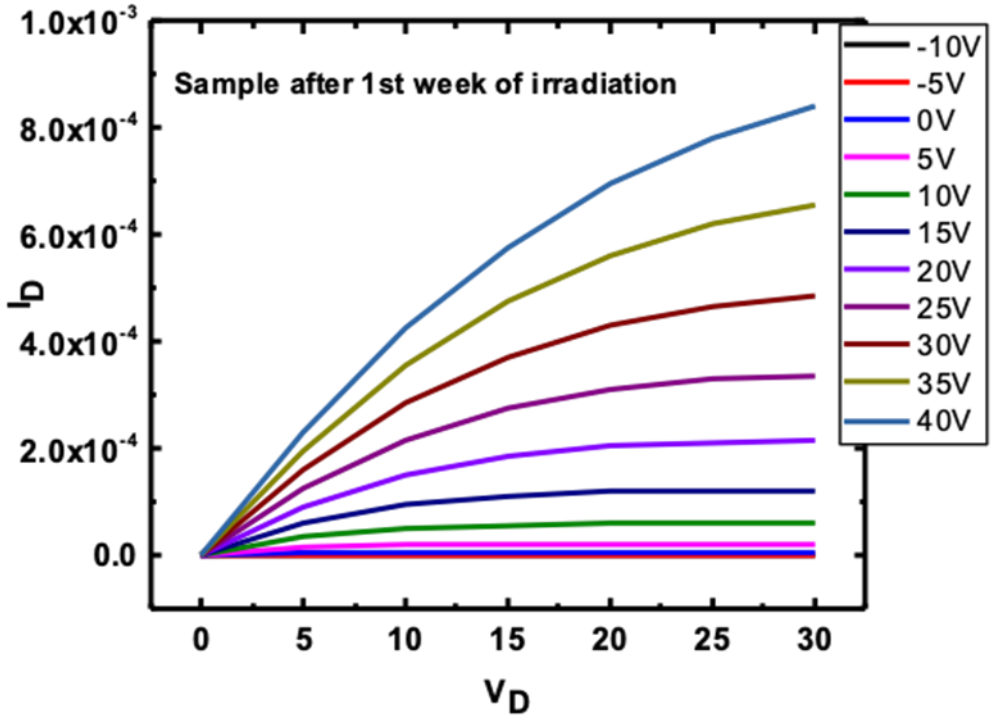
Sample after 1st week of irradiation
-10V
-5V
0V
5V
10V
15V
20V
25V
30V
35V
40V
1.0x10-3
8.0x10-4
6.0x10-4
4.0x10-4
2.0x10-4
0.0
ID
0
5
10
15
20
25
30
VD

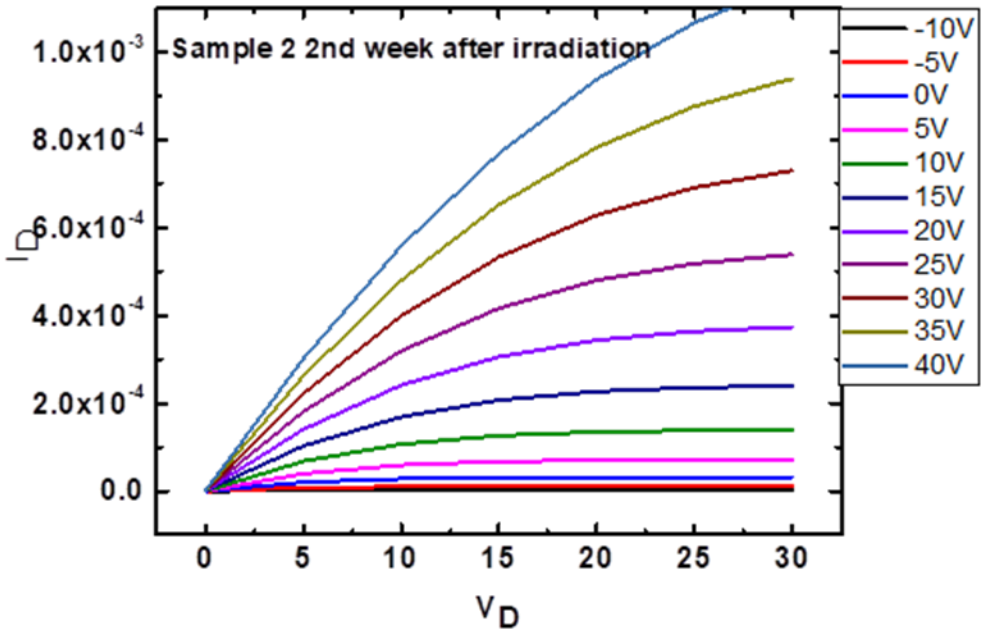
Sample 2 2nd week after irradiation
1.0x10-3
8.0x10-4
6.0x10-4
4.0x10-4
2.0x10-4
0.0
ID
0
5
10
15
20
25
30
VD
-10V
-5V
0V
5V
10V
15V
20V
25V
30V
35V
40V

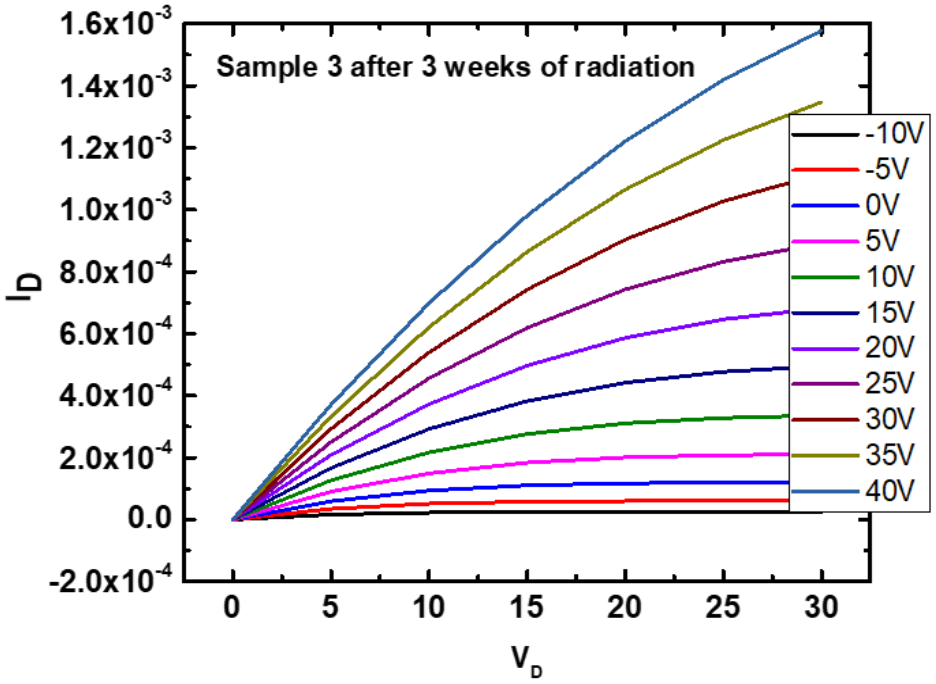
Sample 3 after 3 weeks of radiation
1.6x10-3
1.4x10-3
1.2x10-3
1.0x10-3
8.0x10-4
6.0x10-4
4.0x10-4
2.0x10-4
0.0
-2.0x10-4
ID
0
5
10
15
20
25
30
VD
-10V
-5V
0V
5V
10V
15V
20V
25V
30V
35V
40V

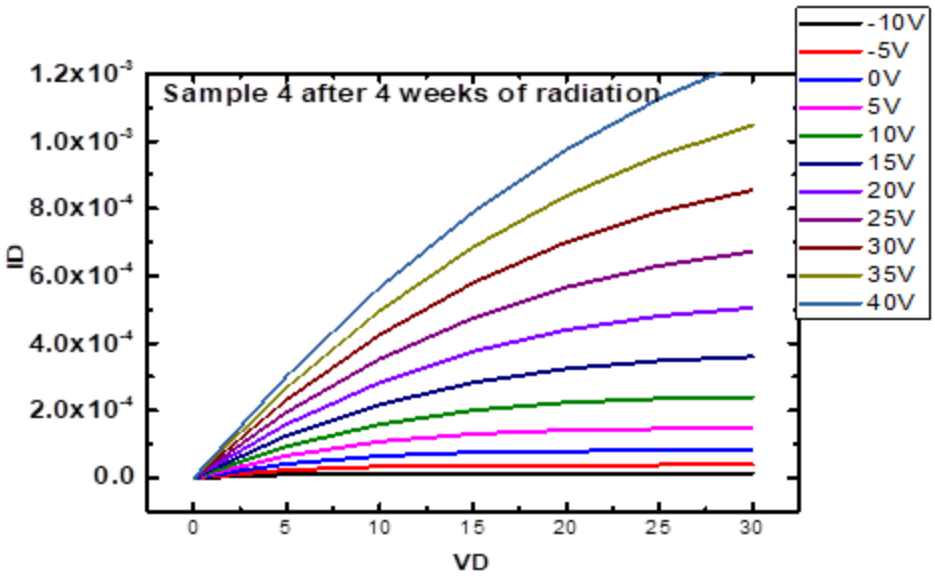

Figure 6.12: Representative Output characteristics of a. Pristine sample b. one week after irradiation c. two weeks after irradiation d. three weeks after irradiation e. four weeks

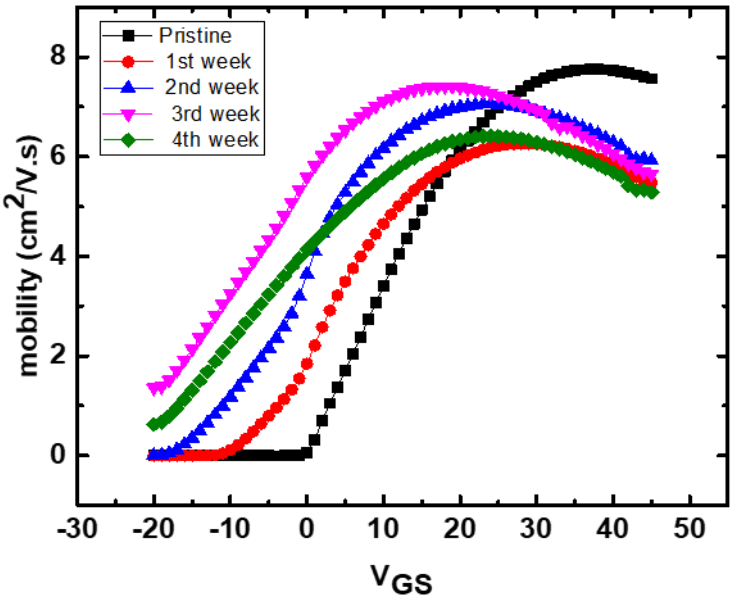

Figure 6.1513: Mobility vs. Gate to Source voltage for Pristine and Irradiated samples

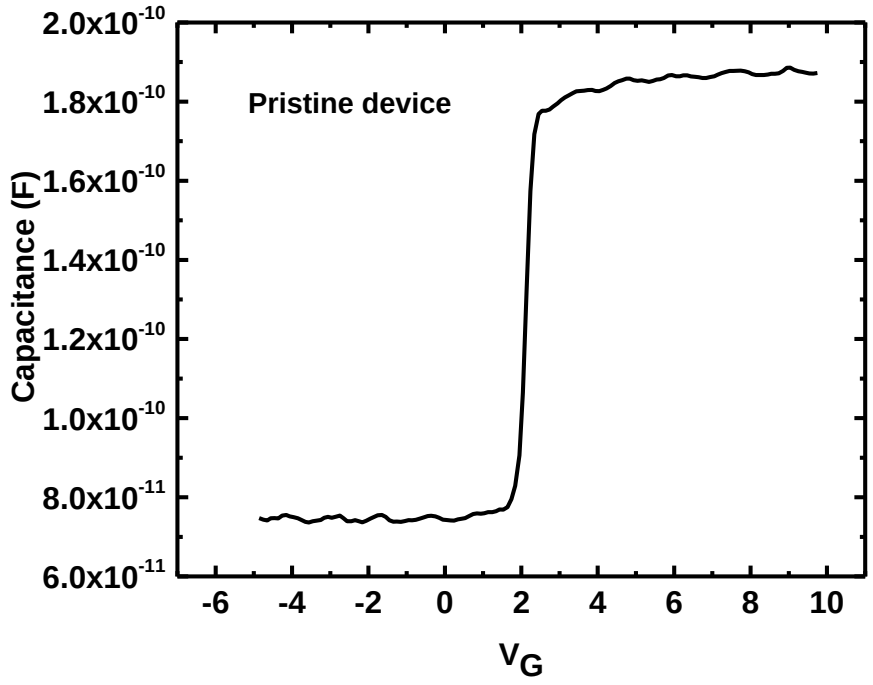
Pristine device
Capacitance (F)
2.0x10-10
1.8x10-10
1.6x10-10
1.4x10-10
1.2x10-10
1.0x10-10
8.0x10-11
6.0x10-11
-6
-4
-2
0
2
4
6
8
10
VG

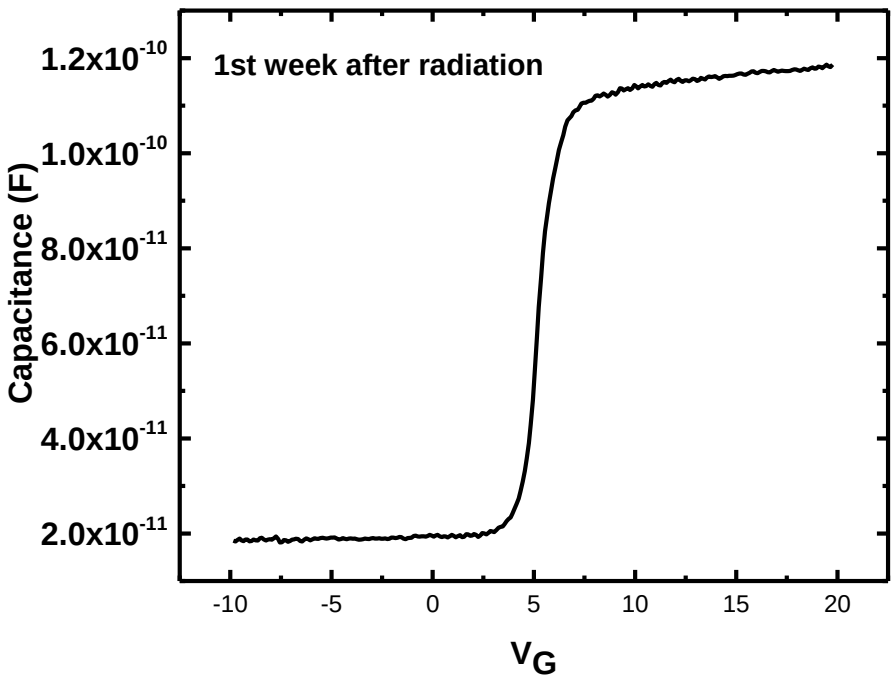
1st week after radiation
Capacitance (F)
1.2x10-10
1.0x10-10
8.0x10-11
6.0x10-11
4.0x10-11
2.0x10-11
-10
-5
0
5
10
15
20
VG

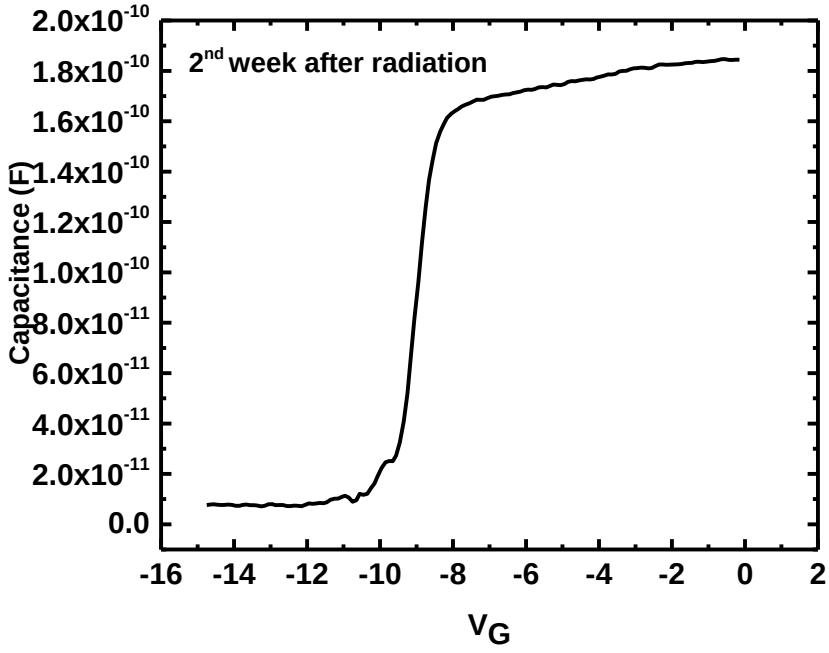
2nd week after radiation
Capacitance (F)
2.0x10-10
1.8x10-10
1.6x10-10
1.4x10-10
1.2x10-10
1.0x10-10
8.0x10-11
6.0x10-11
4.0x10-11
2.0x10-11
0.0
-16
-14
-12
-10
-8
-6
-4
-2
0
2
VG

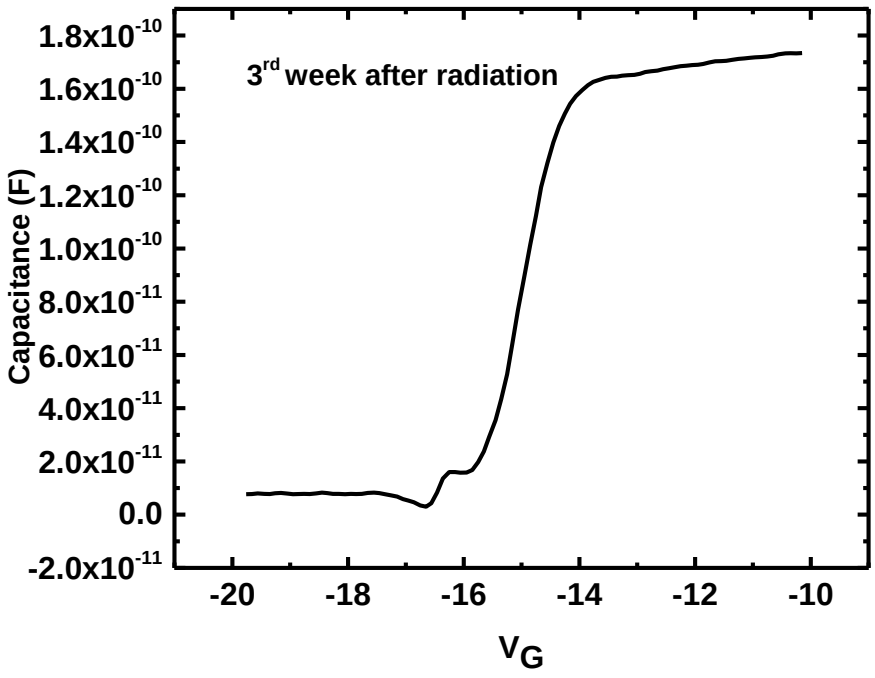
3rd week after radiation
Capacitance (F)
1.8x10-10
1.6x10-10
1.4x10-10
1.2x10-10
1.0x10-10
8.0x10-11
6.0x10-11
4.0x10-11
2.0x10-11
0.0
-2.0x10-11
-20
-18
-16
-14
-12
-10
VG

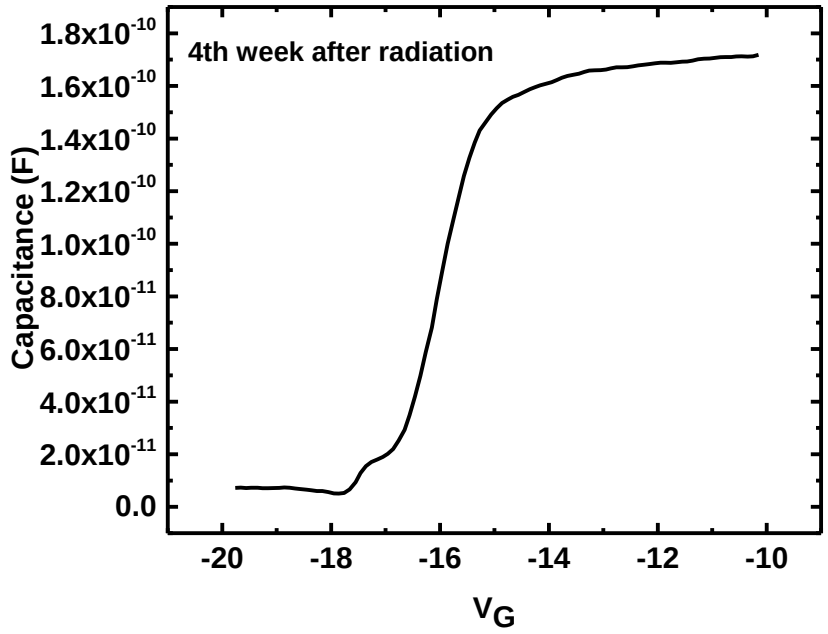

Figure 6.14: C-V measurements for the Pristine and Irradiated samples

Table 6.4: TFTs characteristics as obtained from I-V and C-V plots for Pristine and Irradiated sample

	Pristine	**1st week**	**2nd week**	**3rd week**	**4th week**
Threshold Voltage (V_{th}) V	10	0	-7	-17	-12
Filed Effect Mobility (μ_{FE}) ($cm^2/V.s$)	7.56	5.47	5.92	5.64	5.28
Donor Concentration (N_D) ($10^{18}/cm^{-3}$)	0.63	5.44	3.95	1.05	2.06

If cases of SiO_2 on silicon [74] and Silicon Carbide (SiC) n-channel MOSFETs [75] is considered, threshold voltages initially shifted upon irradiation as positively oxide-trap charges

are produced in a more significant amount than the interface traps, which are acceptors (negatively charged) for the upper half of the band-gap. The overall net effect of positive charges impacts the TFTs' electrical characteristics by shifting its threshold voltage towards negative values. With further irradiation, the interface traps' density increases substantially and eventually more significantly than the irradiation-induced oxide trap charge. As a result, the threshold voltage shifts back towards positive values. Thus, the change in the threshold voltage direction seems because of both irradiation-induced positively charged oxide charges and negatively charged interface traps. When the samples had been subjected to further irradiation for four weeks, the density of interface traps could have been increased compared to the positive oxide charges, which led to the threshold voltage shift to the positive side.

The shifting of threshold voltage also could be attributed to the increase and decrease of carrier concentration as calculated from the C-V curve. After the irradiation, the increase in oxygen vacancies might be attributed to the increase in the carrier concentration in the films. However, as seen in figure 6.8, OH^- (hydroxyl), oxygen in the samples is increased compared to the pristine films. OH^- oxygen acts as traps in oxide semiconductors and tends to decrease the carrier concentration.

6.12 Conclusion

TFTs were fabricated *via* the sol-gel spin coating process and were measured before and after irradiation. An increase in the surface roughness of the irradiated samples was observed. Measurements indicated a negative shift in the threshold voltage for the devices irradiated for three weeks and changed the direction for the samples irradiated for four weeks. The increase and decrease in threshold voltage were attributed to the acceptor-like traps (positive oxide charges) and depopulation of donor-like traps (negative interface states), respectively. A decrease in

mobility could also be attributed to the increase in interface states and the increase in surface roughness, creation of defects, displacement damages, local disorder of the material.

6.13 References

[1] Galactic cosmic rays. (n.d.). Retrieved March 10, 2021, from https://www.swpc.noaa.gov/phenomena/galactic-cosmic-rays

[2] Singer, S. F. (1958). " Radiation Belt" and Trapped Cosmic-Ray Albedo. *Physical Review Letters*, *1*(5), 171.

[3] Cress, C. D., Hubbard, S. M., Landi, B. J., Raffaelle, R. P., & Wilt, D. M. (2007). Quantum dot solar cell tolerance to alpha-particle irradiation. *Applied Physics Letters*, *91*(18), 183108.

[4] Narsingi, K. Y., Manasreh, M. O., & Weaver, B. D. (2007, April). Proton irradiation effect on cdse-zns core-shell nanocrystals embedded in ultra violet curable resin. In *2007 IEEE Region 5 Technical Conference* (pp. 436-440). IEEE.

[5] Draganic, I. G., & Adloff, J. P. (1993). *Radiation and radioactivity on earth and beyond*. CRC press.

[6] Afshinnekoo, E., Scott, R. T., MacKay, M. J., Pariset, E., Cekanaviciute, E., Barker, R., ... & Beheshti, A. (2020). Fundamental Biological Features of Spaceflight: Advancing the Field to Enable Deep-Space Exploration. *Cell*, *183*(5), 1162-1184.

[7] Stassinopoulos, E. G., & LaBel, K. A. (2004). The Near-Earth Space Radiation Environment for Electronics. *Space Magazine*, (6).

[8] Beville, T. (2014). NASA-Space Radiation Analysis Group (SRAG) Web Site. *Terrie Bevill*.

[9] Bourdarie, S., & Xapsos, M. (2008). The near-earth space radiation environment. *IEEE transactions on nuclear science*, *55*(4), 1810-1832.

[10] Hu, S. (2017). Solar particle events and radiation exposure in space. *NASA Space Radiation Program Element. NASA Space Radiation Program Element, Human Research Program*, 1-15.

[11] Zell, H. (2015, March 02). Earth's magnetosphere. Retrieved March 10, 2021, from http://www.nasa.gov/mission_pages/sunearth/multimedia/magnetosphere.html

[12] Howell, E. (2018, May 11). Van Allen radiation Belts: Facts & findings. Retrieved March 10, 2021, from https://www.space.com/33948-van-allen-radiation-belts.html

[13] Baker, D. N., & Lanzerotti, L. J. (2016). Resource letter SW1: Space weather. *American Journal of Physics*, *84*(3), 166-180.

[14] Baker, D. N. (2014). New twists in earth's radiation belts. *American Scientist*, *102*(5), 374-382.

[15] Johnston, A. H. (1998). Radiation effects in advanced microelectronics technologies. *IEEE transactions on Nuclear Science*, *45*(3), 1339-1354.

[16] Zeynali, O., Masti, D., & Gandomkar, S. (2012). Shielding protection of electronic circuits against radiation effects of space high energy particles. *Adv. Appl. Sci. Res*, *3*(1), 446-451.

[17] Gregory, B. L., & Gwyn, C. W. (1974). Radiation effects on semiconductor devices. *Proceedings of the IEEE*, *62*(9), 1264-1273.

[18] Raymond, J. P., & Petersen, E. L. (1987). Comparison of neutron, proton and gamma ray effects in semiconductor devices. *IEEE Transactions on Nuclear Science*, *34*(6), 1621-1628.

[19] Wilson, L. (2013). International technology roadmap for semiconductors (ITRS). *Semiconductor Industry Association*, *1*.

[20] Oldham, T. R., & McLean, F. B. (2003). Total ionizing dose effects in MOS oxides and devices. *IEEE transactions on nuclear science*, *50*(3), 483-499.

[21] Benedetto, J. M., & Boesch, H. E. (1986). The relationship between 60Co and 10-keV X-ray damage in MOS devices. *IEEE Transactions on Nuclear Science*, *33*(6), 1317-1323.

[22] Curtis Jr, O. L., Srour, J. R., & Chiu, K. Y. (1974). Hole and electron transport in SiO2 films. *Journal of Applied Physics*, *45*(10), 4506-4513.

[23] Dressendorfer, P. V. (1989). MOS DEVICES AND CIRCUITS. *Ionizing radiation effects in MOS devices and circuits*, 256.

[24] Hughes, R. C. (1973). Charge-Carrier Transport Phenomena in Amorphous Si O 2: Direct Measurement of the Drift Mobility and Lifetime. *Physical Review Letters*, *30*(26), 1333.

[25] Buchner, S., McMorrow, D., Melinger, J., & Camdbell, A. B. (1996). Laboratory tests for single-event effects. *IEEE Transactions on Nuclear Science*, *43*(2), 678-686.

[26] Reed, R. A., Carts, M. A., Marshall, P. W., Marshall, C. J., Musseau, O., McNulty, P. J., ... & Corbiere, T. (1997). Heavy ion and proton-induced single event multiple upset. *IEEE Transactions on Nuclear Science*, *44*(6), 2224-2229.

[27] Dodd, P. E., Schwank, J. R., Shaneyfelt, M. R., Felix, J. A., Paillet, P., Ferlet-Cavrois, V., ... & Saito, H. (2007). Impact of heavy ion energy and nuclear interactions on single-event upset and latchup in integrated circuits. *IEEE Transactions on Nuclear Science*, *54*(6), 2303-2311.

[28] Weatherfold, T. R., Tran, L., Stapor, W. J., Petersen, E. L., Langworthy, J. B., McMorrow, D., ... & McNulty, P. J. (1991). Proton and heavy ion upsets in GaAs MESFET devices. *IEEE transactions on nuclear science*, *38*(6), 1460-1466.

[29] Dodd, P. E., Sexton, F. W., Hash, G. L., Shaneyfelt, M. R., Draper, B. L., Farino, A. J., & Flores, R. S. (1996). Impact of technology trends on SEU in CMOS SRAMs. *IEEE Transactions on Nuclear Science*, *43*(6), 2797-2804.

[30] Schwank, J. R. (2002, July). Total dose effects in MOS devices. In *IEEE NSREC short course* (Vol. 111, No. 123).

[31] Pearton, S. J., Ren, F., Patrick, E., Law, M. E., & Polyakov, A. Y. (2015). Ionizing radiation damage effects on GaN devices. *ECS Journal of solid state science and technology*, *5*(2), Q35.

[32] Bai, X. M., Voter, A. F., Hoagland, R. G., Nastasi, M., & Uberuaga, B. P. (2010). Efficient annealing of radiation damage near grain boundaries via interstitial emission. *Science*, *327*(5973), 1631-1634.

[33] Whyte, G. N. (1955). Measurements of Spectral and Angular Distributions of Secondary Gamma-Rays in Matter. *Canadian Journal of Physics*, *33*(2), 96-109.

[34] Jin, L., & Clayton, D. D. (1995). Gamma rays, cosmic rays, and extinct radioactivity in molecular clouds. *The Astrophysical Journal*.

[35] Gamma rays in matter. (n.d.). Retrieved March 10, 2021, from https://www.radioactivity.eu.com/site/pages/Gamma_Matter.htm

[36] Jelenković, E. V., Kovačević, M. S., Stupar, D. Z., Bajić, J. S., Slankamenac, M. P., Kovačević, M., & To, S. (2013). N-channel polysilicon thin film transistors as gamma-ray detectors. *Measurement Science and Technology*, *24*(10), 105103.

[37] Lee, E. H., Indluru, A., Allee, D. R., Clark, L. T., Holbert, K. E., & Alford, T. L. (2011). Effects of gamma irradiation and electrical stress on a-Si: H thin-film transistors for flexible electronics and displays. *Journal of Display Technology*, *7*(6), 325-329.

[38] Imagawa, O., Yasuda, K., & Yoshida, A. (1989). Gamma-ray irradiation effect in amorphous hydrogenated silicon. *Journal of applied physics*, *66*(10), 4719-4722.

[39] Davidović, V., Kouvatsos, D. N., Stojadinović, N., & Voutsas, A. T. (2007). Influence of polysilicon film thickness on radiation response of advanced excimer laser annealed polycrystalline silicon thin film transistors. *Microelectronics Reliability*, *47*(9-11), 1841-1845.

[40] Sayyed, M. I., Elmahroug, Y., Elbashir, B. O., & Issa, S. A. (2017). Gamma-ray shielding properties of zinc oxide soda lime silica glasses. *Journal of Materials Science: Materials in Electronics*, *28*(5), 4064-4074.

[41] Khanal, M. P., Ozden, B., Kim, K., Uprety, S., Mirkhani, V., Yapabandara, K., ... & Park, M. (2017). Electrical and optical characteristics of gamma-ray irradiated AlGaN/GaN high electron mobility transistors. *Journal of Vacuum Science & Technology B, Nanotechnology and Microelectronics: Materials, Processing, Measurement, and Phenomena*, *35*(3), 03D107.

[42] Deshpande, V. K., & Raut, A. P. (2017). Effect of gamma irradiation on the density, glass transition temperature and electrical conductivity of lithium borosilicate glasses with alumina addition. *Journal of Non-Crystalline Solids*, *457*, 104-110.

[43] Novak, S., Singh, V., Monmeyran, C., Ingram, A., Han, Z., Lin, H., ... & Richardson, K. (2017). Positron annihilation lifetime spectroscopy (PALS) studies of gamma irradiated As2Se3 films used in MIR integrated photonics. *Journal of Non-Crystalline Solids*, *455*, 29-34.

[44] Ozden, B., Khanal, M. P., Park, J., Uprety, S., Mirkhani, V., Yapabandara, K., ... & Park, M. (2017). Raman and X-ray photoelectron spectroscopy investigation of the effect of gamma-ray irradiation on MoS2. *Micro & Nano Letters*, *12*(4), 271-274.

[45] Abubakar, S., Kaya, S., Karacali, H., & Yilmaz, E. (2017). The gamma irradiation responses of yttrium oxide capacitors and first assessment usage in radiation sensors. *Sensors and Actuators A: Physical*, *258*, 44-48.

[46] Gorelkinskii, Y. V., & Watkins, G. D. (2004). Defects produced in ZnO by 2.5-MeV electron irradiation at 4.2 K: Study by optical detection of electron paramagnetic resonance. *Physical Review B*, *69*(11), 115212.

[47] Smith, J. M., & Vehse, W. E. (1970). ESR of electron irradiated ZnO confirmation of the F+ center. *Physics Letters A*, *31*(3), 147-148.

[48] Vlasenko, L. S., & Watkins, G. D. (2005). Optical detection of electron paramagnetic resonance for intrinsic defects produced in ZnO by 2.5-MeV electron irradiation in situ at 4.2 K. *Physical Review B*, *72*(3), 035203.

[49] Look, D. C., Reynolds, D. C., Hemsky, J. W., Jones, R. L., & Sizelove, J. R. (1999). Production and annealing of electron irradiation damage in ZnO. *Applied Physics Letters*, *75*(6), 811-813.

[50] Coskun, C., Look, D. C., Farlow, G. C., & Sizelove, J. R. (2004). Radiation hardness of ZnO at low temperatures. *Semiconductor Science and Technology*, *19*(6), 752.

[51] Knutsen, K. E., Galeckas, A., Zubiaga, A., Tuomisto, F., Farlow, G. C., Svensson, B. G., & Kuznetsov, A. Y. (2012). Zinc vacancy and oxygen interstitial in ZnO revealed by sequential annealing and electron irradiation. *Physical Review B, 86*(12), 121203.

[52] Nesheva, D., Šćepanović, M., Grujić-Brojčin, M., Dzhurkov, V., Kaschieva, S., Bineva, I., ... & Popović, Z. V. (2016, October). Photoluminescence from 20 MeV electron beam irradiated homogeneous SiOx and composite Si-SiOx films. In *Journal of Physics: Conference Series* (Vol. 764, No. 1, p. 012018). IOP Publishing.

[53] Jeong, S. H., Bae, B. S., Yu, K. M., Ryu, M. K., Cho, K. I., & Yun, E. J. (2012). Properties of IGZO thin films irradiated by electron beams with various energies. *Journal of the Korean Physical Society*, *61*(6), 867-872.

[54] Dayananda, G. K., Rai, C. S., Jayarama, A., & Kim, H. J. (2018). Simulation model for electron irradiated IGZO thin film transistors. *Journal of Semiconductors*, *39*(2), 022002.

[55] Hong, W. K., Jo, G., Sohn, J. I., Park, W., Choe, M., Wang, G., ... & Lee, T. (2010). Tuning of the electronic characteristics of ZnO nanowire field effect transistors by proton irradiation. *Acs Nano*, *4*(2), 811-818.

[56] Khanna, R., Ip, K., Allums, K. K., Baik, K., Abernathy, C. R., Pearton, S. J., ... & Wilkins, R. (2004). Effects of high dose proton irradiation on the electrical performance of ZnO schottky diodes. *physica status solidi (a)*, *201*(12), R79-R82.

[57] Park, B., Ho, D., Kwon, G., Kim, D., Seo, S. Y., Kim, C., & Kim, M. G. (2018). Solution-Processed Rad-Hard Amorphous Metal-Oxide Thin-Film Transistors. *Advanced Functional Materials*, *28*(47), 1802717.

[58] Taylor, A. L., Filipovich, G., & Lindeberg, G. K. (1970). Electron paramagnetic resonance associated with Zn vacancies in neutron-irradiated ZnO. *Solid State Communications*, *8*(17), 1359-1361.

[59] Flitsiyan, E. S., Swartz, C. M., Peale, R. E., Lupan, O., Chernyak, L., Chow, L., ... & Dashevsky, Z. (2008). Neutron transmutation doping and radiation hardness for solution-grown bulk and nano-structured ZnO. *MRS Online Proceedings Library (OPL)*, *1108*.

[60] Flitsiyan, E. S., Swartz, C. M., Peale, R. E., Lupan, O., Chernyak, L., Chow, L., ... & Dashevsky, Z. (2008). Neutron transmutation doping and radiation hardness for solution-grown bulk and nano-structured ZnO. *MRS Online Proceedings Library (OPL)*, *1108*.

[61] Kucheyev, S. O., Williams, J. S., Titov, A. I., Li, G., & Jagadish, C. (2001). Effect of the density of collision cascades on implantation damage in GaN. *Applied Physics Letters*, *78*(18), 2694-2696.

[62] Azarov, A. Y., Kucheyev, S. O., Titov, A. I., & Karaseov, P. A. (2007). Effect of the density of collision cascades on ion implantation damage in ZnO. *Journal of Applied Physics*, *102*(8), 083547.

[63] Wendler, E., Bilani, O., Gärtner, K., Wesch, W., Hayes, M., Auret, F. D., ... & Alves, E. (2009). Radiation damage in ZnO ion implanted at 15 K. *Nuclear Instruments and Methods in Physics Research Section B: Beam Interactions with Materials and Atoms*, *267*(16), 2708-2711.

[64] Liao, L., Lu, H. B., Li, J. C., Liu, C., Fu, D. J., & Liu, Y. L. (2007). The sensitivity of gas sensor based on single ZnO nanowire modulated by helium ion radiation. *Applied Physics Letters*, *91*(17), 173110.

[65] Ramirez, J. I., Li, Y. V., Basantani, H., Leedy, K., Bayraktaroglu, B., Jessen, G. H., & Jackson, T. N. (2015). Radiation-hard ZnO thin film transistors. *IEEE Transactions on Nuclear Science*, *62*(3), 1399-1404.

[66] Indluru, A., Holbert, K. E., & Alford, T. L. (2013). Gamma radiation effects on indium-zinc oxide thin-film transistors. *Thin Solid Films*, *539*, 342-344.

[67] Lee, K. K., Wang, D., Shinobu, O., & Ohshima, T. (2018). Reliability of gamma-irradiated n-channel ZnO thin-film transistors: electronic and interface properties. *Radiation Effects and Defects in Solids*, *173*(3-4), 250-260.

[68] Ismail, A., Alahmad, M., Alsabagh, M., & Abdallah, B. (2020). Effect of low dose-rate industrial Co-60 gamma irradiation on ZnO thin films: Structural and optical study. *Microelectronics Reliability*, *104*, 113556.

[69] Huang, C. Y. (2020). The effect of Gamma irradiation on the stability of amorphous InGaZnO metal-semiconductor-metal UV photodetectors. *Journal of Non-Crystalline Solids*, *546*, 120292.

[70] Alyamani, A., & Mustapha, N. (2016). Effects of high dose gamma irradiation on ITO thin film properties. *Thin Solid Films*, *611*, 27-32.

[71] Wang, X. D., He, S. Y., Yang, D. Z., & Gu, P. F. (2011). Space Radiation Damage in ZnO Induced by Subthreshold Electrons: Defect Identity and Optical Degradation. *Radiation research*, *176*(2), 264-268.

[72] Fu, Z., Yang, B., Li, L., Dong, W., Jia, C., & Wu, W. (2003). An intense ultraviolet photoluminescence in sol–gel ZnO–SiO2 nanocomposites. *Journal of Physics: Condensed Matter*, *15*(17), 2867.

[73] Thapa, D., Huso, J., Morrison, J. L., Corolewski, C. D., McCluskey, M. D., & Bergman, L. (2016). Achieving highly-enhanced UV photoluminescence and its origin in ZnO nanocrystalline films. *Optical Materials*, *58*, 382-389.

[74] Oldham, T. R., & McLean, F. B. (2003). Total ionizing dose effects in MOS oxides and devices. *IEEE transactions on nuclear science*, *50*(3), 483-499.

[75] Lee, K. K., Ishida, Y., Ohshima, T., Kojima, K., Tanaka, Y., Takahashi, T., ... & Kamiya, T. (2003). N-channel MOSFETs fabricated on homoepitaxy-grown 3C-SiC films. *IEEE Electron Device Letters*, *24*(7), 466-468.

Chapter 7

Conclusions and Future work

7.1 Conclusions

In chapter 4, multistacking of different molar concentrations of ZTO solution was performed and ZTO thin films and TFTs were fabricated and analyzed. It was, based on the surface characterization techniques such as XRD and AFM, concluded that the films are amorphous or close to nanocrystalline and the least surface roughness was obtained for the films with multistacked layer. It was also deduced from the electrical characterizations of the fabricated TFTs that multistacked layer performed well in comparison to the TFTs fabricated with 0.05M and 0.2M solution. It was conjectured that a film with the lowest molar concentration might have worked as a nucleation layer to reduce the interface traps between the dielectric layer and the channel.

In chapter 5, microwave irradiation for different powers of a microwave was employed as a heating substitute for the hot plate annealed samples for the enhancement of the electrical characteristics of the fabricated TFTs. For all the powers of the microwave as demonstrated from the XPS, concentration of the oxygen vacancies was increased and reduction of hydroxyl components in the films were highly decreased. As oxygen vacancies acts as shallow donor the donor concentration in the film might have increased and eventually led to the reduced threshold voltage. The increase in mobility for the microwave irradiated films could be attributed to the dihydroxylation *i.e.,* the reduction of OH^- species in the film.

In chapter 6, effects of cumulative gamma irradiation on ZTO thin films and TFTs were investigated. The increase and decrease in threshold voltage were attributed to the acceptor-like traps (positive oxide charges) and depopulation of donor-like traps (negative interface states),

respectively. A decrease in mobility could also be attributed to the increase in interface states and other imperfections caused by irradiation.

7.2 Future work

Chapter 5 discusses microwave radiation as an alternative source of annealing for solution processed ZTO. A lab grade microwave with a better control over the temperature and ambient atmosphere can be used for the research work to be pursued in the future. As an alternative avenue of annealing technique, laser irradiation on solution processed films and its effects on fabricated devices remains to be investigated.

In chapter 6, gamma irradiation for a relatively low dosage was studied. Stability of TFTs under higher gamma irradiation dosage is still a matter of study. Proton Irradiation on AOSs still need a room for additional study. Stopping and Ranges of Ions in matter (SRIM) simulation could be employed to study the distribution of irradiation for different thicknesses of ZTO.